

AROD-T-2.17-E

AD718798



REPORT 70-7

**AN EXPERIMENTAL INVESTIGATION  
OF A TURBULENT JET IN A CROSS FLOW**

David K. Mosher

DECEMBER 1970



Reproduced by  
NATIONAL TECHNICAL  
INFORMATION SERVICE  
Springfield, Va 22151

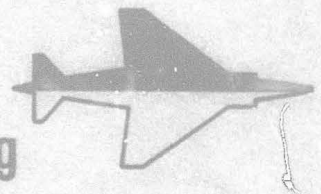
GITAER 70-7

This work was supported by the U. S. Army Research  
Office — Durham under Contract No. DAHCO4 68 C 0004.

This document has been approved for public release  
and sale; its distribution is unlimited.



**School of Aerospace Engineering**  
**GEORGIA INSTITUTE OF TECHNOLOGY**  
Atlanta, Georgia 30332



REPORT 70-7

AN EXPERIMENTAL INVESTIGATION  
OF A TURBULENT JET IN A CROSS FLOW

David K. Mosher

This work was done in partial  
fulfillment of the requirements for  
the Degree of Doctor of Philosophy.

December 1970

Prepared for  
U. S. Army Research Office, Durham  
under  
Project THEMIS  
Contract No. DAHCO4 68 C 0004

This document has been approved for public release  
and sale; its distribution is unlimited.

School of Aerospace Engineering  
Georgia Institute of Technology  
Atlanta, Georgia 30332

## ACKNOWLEDGMENTS

I would like to especially thank Dr. Howard M. McMahon for his suggestion of the thesis topic and guidance throughout the entire research program. To Dr. James C. Wu and Professor James E. Hubbartt I am also indebted for both the reading of the manuscript and fruitful discussions during the conduct of the investigation.

Appreciation is extended to J. G. Palfrey for his assistance in all phases of the research. For help in various stages of the design and construction of equipment I would like to thank G. T. Bird, H. R. Hudson, D. L. Ransom and C. H. Wiser.

Fellow students have also provided technical support and meaningful discussion. For assistance in this area gratitude is expressed to D. C. Seymour, M. N. Milhous, Jr., M. A. Wright and D. Hester.

I wish to gratefully acknowledge the financial support provided by project Themis (U. S. Army Research Office, Durham) and a National Defense Education Act Title IV Fellowship.

Finally, I want to express gratitude to my wife, [REDACTED] and sons, [REDACTED] for their inspiration and understanding.

# TABLE OF CONTENTS

	Page
ACKNOWLEDGMENTS . . . . .	ii
LIST OF TABLES . . . . .	v
LIST OF ILLUSTRATIONS . . . . .	vi
NOMENCLATURE . . . . .	ix
SUMMARY . . . . .	xi
Chapter	
I. INTRODUCTION . . . . .	1
Literature Review	
Review Objective and Scope	
II. EQUIPMENT AND INSTRUMENTATION . . . . .	8
Flat Plate and Nozzles	
Air Supply	
Solid Blockage Model	
Probes and Supply Mechanisms	
Pressure Switching Equipment	
Pressure Measuring Equipment	
Flow Visualization	
III. PROCEDURE . . . . .	16
Test Technique	
Accuracy	
IV. RESULTS AND DISCUSSION . . . . .	27
Summary of Collected Data	
Interpretation	
V. CONCLUSIONS . . . . .	53
APPENDIX	
A. NOZZLE DESIGN . . . . .	56

	Page
CITED LITERATURE. . . . .	63
TABLES. . . . .	67
ILLUSTRATIONS . . . . .	91

## LIST OF TABLES

Number		Page
1.	Surface Pressure Test Conditions and Result Index. . . . .	68
2.	Pressure Probe Test Conditions and Result Index. . . . .	70
3.	Flow Visualization Test Conditions and Result Index. . . . .	73
4.	Results of Extensive Flow Field Survey for $w/\lambda = 1.0, \lambda = 8$ . . . . .	75

## LIST OF ILLUSTRATIONS

Number		Page
A-1	Nozzle Contours. . . . .	58
A-2	Non-Circular Nozzle, Original Design . . . . .	60
A-3	Oil Visualization at $\lambda = 8$ , Original Design. . . . .	61
A-4	Cross-Sectional Template Shapes, Modified Design . . . . .	62
1	Lift Loss Due to Jet and Cross-Flow Interference . . . . .	92
2	Coordinate System and Definition of Flow Region Terms. . .	93
3	Top View of Flat Plate . . . . .	94
4	Nozzle Blocks: Exit Configurations and Flange Details. . .	95
5	Side View of Nozzle Block in Jet Supply Pipe . . . . .	97
6	Plate Installed in the Wind Tunnel; Configuration For Acquiring Surface Pressures. . . . .	98
7	Blower Performance Curve . . . . .	99
8	Pressure Probe . . . . .	100
9	Pressure Probe and Traversing Mechanism Installation . . .	101
10	Total Pressure Rake. . . . .	102
11	Total Pressure Probe and Stand . . . . .	103
12	Fluid Wafer System . . . . .	104
13	Electronic Manometer System. . . . .	105
14	Smoke Tunnel . . . . .	106
15	Orifices and Plates Used in Smoke Studies. . . . .	107
16	Jet Exit Total Pressure Versus $P_a$ for $\lambda = 12$ , $V_\infty = 50$ ft/sec . . . . .	108
17	Pressure Probe Calibration Curves. . . . .	109

Number		Page
18	10 mmHg Transducer Versus Dead Weight Tester . . . . .	111
19	1000 mmHg Transducer Versus Dead Weight Tester . . . . .	112
20	Surface Pressure Reading Fluctuations, Typical . . . . .	113
21	Jet Plume Reading Fluctuation, Typical . . . . .	114
22	Comparison With Other Investigations . . . . .	115
23	Probe Holder Interference. . . . .	117
24	Composite of $C_p$ Contours . . . . .	118
25	$C_p$ Contours Around Solid Blockage Model. . . . .	119
26	Surface Pressures Behind the Jet, $\beta = 180^\circ$ . . . . .	120
27	Mean Surface Pressures . . . . .	122
28	Center of Pressure . . . . .	124
29	Oil Studies. . . . .	125
30	Tuft Study, $w/l = 1.0$ , $\lambda = 8$ . . . . .	131
31	Jet Paths. . . . .	132
32	Total Pressure Decay Along Jet Path. . . . .	133
33	Smoke Studies, Jet Injection . . . . .	134
34	Smoke Studies, Cross-Flow Injection. . . . .	136
35	Total Pressure Contours in Plume Cross Section at $z/a = 5$ , $\lambda = 8$ . . . . .	138
36	Lateral Flow Field Surveys at $z/a = 6$ . . . . .	139
37	Surface $C_p$ Contours for Solid Blockage Models. . . . .	141
38	Effect of Extrapolation from $z/a > 6$ , $w/l = 3.4$ , $x/a = 0$ , $y/a = 4$ . . . . .	142
39	Free Jet Velocity Decay and Entrainment Data . . . . .	143
40	Surface Pressures for Matching Jet Paths . . . . .	144
41	Interference Lift Loss as a Fraction of Thrust . . . . .	145



Number		Page
42	Attenuation of Lift Loss . . . . .	146
43	Extract from Extensive Flow Field Survey, $w/l = 1.0$ , $\lambda = 8$ . . . . .	147
44	Lateral Flow Field Surveys, $z/a \geq 6$ . . . . .	150
45	Upstream Flow Field Surveys, Solid Blockage. . . . .	154
46	Upstream Flow Field Surveys, Jet On. . . . .	155
47	Surface $C_p$ Contours. . . . .	157

## NOMENCLATURE

$a$	radius of the circular jet
$A_j$	area of circular jet, $\pi a^2$
$C_p$	pressure coefficient, $(P - P_\infty)/q_\infty$
$C_s$	suction force coefficient $\frac{\int_0^\pi \int_{r_1}^{r_2} C_p r dr d\theta}{\pi r_2^2/2}$
$d$	diameter of the circular jet
$\Delta L$	interference lift, $q_\infty C_s S$
$M_j$	jet exit Mach number
$P$	local static pressure
$P_a$	atmospheric pressure
$P_o$	local total pressure
$P_{oe}$	total pressure at jet exit
$P_{o\infty}$	total pressure of the undisturbed cross flow
$q$	local dynamic pressure, $\frac{1}{2} \rho V^2$
$q_x, q_y, q_z$	components of $q$ in Cartesian coordinate system
$q_j$	jet exit dynamic pressure
$q_\infty$	undisturbed cross-flow dynamic pressure
$r, \theta$	polar coordinates in the plane of the plate, Figure 2
$r_1$	radial location of pressure tap nearest to jet exit
$r_2$	upper limit of integration, radial
$R$	radial distance to furthest static pressure tap, $R = 15.75a$

$s$	distance along jet path, Figure 2
$S$	wing reference area
$w/l$	width to length ratio of jet exit geometry
$T$	thrust of the jet, $T = \rho_j v_j^2 m a^2$
$v$	local velocity
$v_j$	velocity at jet exit
$v_m$	maximum velocity in jet plume cross section at any $s$ station
$v_\infty$	undisturbed cross-flow velocity
$v_j/v_\infty$	velocity ratio
$\bar{x}$	center of pressure
$x, y, z$	Cartesian coordinates, Figure 2
$\alpha$	pitch angle of local velocity vector
$\lambda$	effective velocity ratio, $\{\rho_j v_j^2 / \rho_\infty v_\infty^2\}^{1/2}$
$\rho$	local density
$\rho_j$	density at jet exit
$\rho_\infty$	density of undisturbed cross-flow
$\gamma$	yaw angle of local velocity vector

## SUMMARY

The interference phenomenon occurring when a subsonic turbulent jet exhausts normally from a large flat plate into a low speed crossflow has been experimentally investigated in the Georgia Tech nine foot wind tunnel. Static pressures have been measured on the surface around the jet. In the region off the surface, including the jet plume, wake and surrounding areas, the average total and static pressures and the average velocity magnitudes and directions have been determined. Three jet exit configurations were studied, one circular and two slot-shaped with width to length ratios of 0.3 and 3.4. All have the same exit area. The effective jet to cross-flow velocity ratio was varied, for each of exit configurations, over the range  $4.0 \leq \lambda \leq 12.0$ . Analysis of the data indicates that the pressure distributions induced on the surface are a combined result of the jet's blocking and entraining effects on the cross flow with entrainment becoming the more dominant of the two as the effective velocity ratio is increased. This relative dominance brings about an attenuation of total interference lift loss (when computed as a fraction of gross thrust,  $\Delta L/T$ ) primarily by causing a rise in the low pressures in the wake region as  $\lambda$  increases. When the effective velocity ratio is held fixed, the total interference lift loss increases with increasing width to length ratio of the jet exit.

## CHAPTER I

### INTRODUCTION

Aircraft employing lifting jets or fans for vertical or short take off and landing (V/STOL) capability are of current interest. An important problem inherent in these designs arises when this type of aircraft is operating in a flight velocity range which is slow enough to make it dependent on much of the vertically directed thrust for its lift. In this range the interaction of the jet or fan efflux with the cross flow generated by forward flight induces forces on the airplane surface which can significantly reduce the total lift and alter pitching moment characteristics. The need to minimize or reduce these adverse effects necessitates investigations into the details of this flow interaction problem.

#### Literature Review

##### Aircraft Configuration Tests

References 1 through 11 are representative of the testing that has been conducted in an effort to understand the effects of the jet and cross-flow interference problem on specific aircraft configurations. They typically give results regarding gross interference phenomena (see Figure 1) but give little information which can contribute to a basic understanding of the interaction.

More detailed investigations are cited below and have been

categorized into plume and surface pressure investigations.

### Plume Investigations

References 12 through 20 are reports of experimental investigations into some of the various aspects of the jet's behavior as it encounters a cross flow. Early research into penetration characteristics is reported in references 12, 13 and 14. These investigations were not intended for use in V/STOL technology but were instead concerned with the penetration of heated jets for combustion (fuel injection) studies. A tunnel which was narrow relative to orifice size was used which inhibited jet spreading, as was pointed out by Gordier<sup>15</sup> when he attempted to verify this data in a water tunnel. However the relevance of these works to the current study lies in the emergence of the velocity ratio  $V_j/V_\infty$  as a primary parameter influencing penetration in the cross flow.

Jordinson<sup>16</sup> made pressure measurements in the jet plume which gave not only penetration data but also total pressure contours. Similar measurements were made by Gordier<sup>15</sup> in a water tunnel. Both authors note that the jet distorts from a circle to a kidney shape within several diameters from the exit. In addition, their total pressure surveys indicate the presence of a wake region behind the jet where local total pressure is less than that of the free stream.

Gordier released dye on the surface upstream of the jet and noted that there was deceleration of the cross flow as it approached the jet, indicating a blockage effect on the cross flow. Flow was seen to be diverted around the upstream portion of the jet and entrained

along the lateral edges and in the region behind the jet. These basic characteristics of blockage and entrainment were cited earlier by Jordinson<sup>16</sup> when he compared the interference phenomena to that about a cylinder with suction.

References 17 through 19 report on a series of investigations made in order to obtain an understanding of the phenomena of waste disposal situations such as occur when effluents are discharged from chimney stacks into the atmosphere and from sewage lines into lakes and rivers. However the data can be considered applicable to the study of the V/STOL problem inasmuch as the velocity ratio was varied between 2.0 and 10.0 and the experimental apparatus is scaled such that wall effects should be negligible. These authors found that as the jet (with a uniform exit velocity profile) emerges into the cross flow a turbulent shear region begins to spread until it engulfs the central region of essentially uniform velocity known as the potential core. It is noted that the behavior here is similar to that of a free jet (i.e., no cross flow) except that the potential core for the latter is approximately 5 diameters and that for the former is  $2\frac{1}{2}$  diameters. Also, the deflected jet undergoes a cross-sectional shape deformation and by the end of the potential core region a distinct kidney shape is apparent. The investigators attribute this deformation to the fact that the lateral mixing regions are more easily deflected than the core. The subsequent result is a strong circulatory flow in the form of a pair of contra-rotating vortices which sweep flow into the wake region, immediately behind the jet, where a typical fluid particle follows an upward spiral path.

Entrainment was found to be proportional to  $\left[ (v_j/v_\infty)/(s/2a) \right]^{2/3}$  and greater than that of a free jet. Spreading is shown to vary directly with  $s$  and indirectly with  $v_j/v_\infty$ .

The plume reports discussed up to this point (references 12 through 19) are focused on the behavior of the circular jet. Hardy<sup>20</sup> investigated a jet exhausting from a slot which was oriented with the longer dimension perpendicular to the cross flow. The results show that it is deflected more than the circular jet (of the same cross sectional area) and he infers that this increased bending of the slot jet is due to its increased entrainment of cross-flow fluid containing horizontally-directed momentum.

Hardy does acknowledge that the static pressure differential across the jet is partly responsible for bending, but only weakly relative to entrainment. His latter conclusion is demonstrated analytically and agrees with Jordinson's<sup>16</sup> statement (regarding the circular jet) that entrainment is the primary mechanism determining the path of the jet with pressure bending being important only in the first few diameters from the exit.

#### Surface Pressures

Vogler<sup>21</sup> and Bradbury and Wood<sup>22</sup> have measured the pressure distributions on the surface of flat plates around circular jets over a range of  $1.0 \leq v_j/v_\infty \leq 5.0$  and  $2.0 \leq \lambda \leq 11.3$  respectively. The term  $\lambda$  is herein defined as  $\left( \rho_j v_j^2 / \rho_\infty v_\infty^2 \right)^{1/2}$  and will subsequently be referred to as the effective velocity ratio. Bradbury and Wood demonstrated that  $\lambda$  is the proper correlating parameter to be used when



dealing with dissimilar densities. They conclude, upon integration of pressures, that the resultant suction force on the flat plate is of the proper magnitude to be considered as the prime causal factor of lift losses measured in aircraft configuration studies. They were able to control the boundary layer momentum thickness and concluded that its variation within the practical range of interest had insignificant effects on the surface pressures. Also it was demonstrated that a two fold increase in Reynolds number had a very small effect on the pressure.

Surface pressures on the flat surface around a circular jet may also be found in reference 23 where the jet is exhausted into quiescent air and low speed cross flows.

References 24 and 25 present surface pressures measured about a jet exhausting from a wing, the latter including data for non-circular jets. Reference 26 includes a comparison of surface pressures about a circular jet issuing from a wing with those about a circular jet issuing from a flat plate. The authors state that the results on the wing cannot be explained by an extension of the flat plate results, and imply that finite wing effects introduce another parameter into the flow interaction phenomenon.

References 27 through 31 are cited here as representative surveys of the state of the art.

References 32 through 37 represent salient theoretical analyses of the jet in a cross flow. The existence of a wide variety of mathematical models (all yielding creditable agreement with experiment)

further demonstrates the need for more understanding of the details of this interference phenomenon.

### Research Objective and Scope

Previous research has established that the jet induces pressures on the surface through which it exhausts by some combination of blocking and entraining effects which it has on the cross flow. However the specific manner in which these factors affect the pressure distribution is still unknown. (The definitions of the terms blockage and entrainment may vary from author to author, whether explicitly stated or left implied by contextual usage. This author's definitions will be given in Chapter IV).

The purpose of this investigation is to gain insight into the basic mechanism of this flow problem; specifically to understand how the jet induces the pressure distribution on the surface through which it exhausts. The interaction phenomena is very complex and the approach taken here has been to simplify the problem as much as possible, yet retaining important features. To this end the jet has been exhausted through a large flat plate and the experimental program consists of a series of coordinated tests where surface pressure distributions and data away from the surface (both in and around the plume) are concomitantly collected while the effective velocity ratio and jet exit configurations are systematically varied. The basic approach is to vary the conditions away from the circular case and, by observing the resulting behavior, obtain more understanding of the fundamental mechanisms. Not enough is known to be able to design an experimental

model that allows direct control of entrainment and blockage as though they were test variables. However, it was felt that a systematic variation of the thickness ratio of the jet exit  $w/l$  and effective velocity ratio  $\lambda$  would cause implicit changes in blockage and entrainment, with the explicit variations being determined by data analysis.

The range of effective velocity ratio over which the investigation is conducted is  $4.0 \leq \lambda \leq 12.0$ . Although not all investigators agree, the current literature indicates that this is generally the range where the interference effects are of practical aerodynamic concern.

The literature also demonstrates a need for more experimental data, other than surface pressures, in order to expand the regions of the flow where mathematical predictions can be compared with experiment. To fill this need, an extensive flow field survey has been conducted, away from the plate and generally out of the jet plume proper, for the circular jet at  $\lambda = 8$ .

## CHAPTER II

### EQUIPMENT AND INSTRUMENTATION

The experimental apparatus involves a jet exhausting upward through the center of a large flat plate installed 13 inches above the test section floor in the Georgia Tech nine foot wind tunnel. The wind tunnel is a closed return, atmospheric type with a continuously variable velocity in the test section from approximately 5 to 160 miles per hour. The turbulence factor is 1.04.

#### Flat Plate and Nozzles

Figure 3 shows a top-view of the plate. Its dimensions are 48 inches x 66 inches in the chordwise and spanwise direction respectively and it is made of 0.375 inch thick aluminum. An annular disk with a 32 inch outside diameter, a 7 inch inside diameter, and of the same material is inlaid in the center so as to be flush with the top of the plate, the maximum discontinuity between the two surfaces being  $\pm 0.010$  inches. This discontinuity was considered acceptable in light of its relationship to a boundary layer thickness of approximately 1.0 inch. This disk has one row of static pressure taps, as shown, and can be rotated remotely so that surface pressures can be measured at any angular position around the jet. On the lower surface at the juncture of the plate and the disk is a tongue and groove arrangement which allows the disk to rotate while keeping it restrained in the vertical direction. The same arrangement is repeated where the inner edge

junctures with the nozzle flange.

The center 7.0 inch diameter is occupied by the jet nozzle and flange, which together constitute the "nozzle block". Below the nozzle block is the jet supply pipe. Figure 3 shows the circular nozzle block in place. Figure 4 gives a close-up view of all three exit configurations used in the experiment. The two non-circular configurations use the same nozzle block. (The nozzle contour design procedure is given in Appendix A). When installed so that the longer dimension parallels the free stream flow the exit configuration will be referred to as "streamwise" or  $w/l = 0.3$ ; when perpendicular, "blunt" or  $w/l = 3.4$ . In the installed position, the nozzle blocks are attached to the supply pipe by screws (Figure 5) and do not rotate with the disk. This necessitates the many static pressure taps which can be seen on the nozzle flanges in Figure 4. The taps on both the nozzle flanges and the annular disk are 0.040 inches in diameter.

Figure 6 is view looking upstream from the aft end of the test section showing the plate installed. The plate is supported by 8 legs made of 1/2 inch threaded steel rod. Each leg fits through a hole in the wind tunnel floor, and with the aid of adjustment nuts the plate can be either leveled or set to some desired angle of attack. The plate is installed so as to almost span the test section, with its center at a height of approximately 13 inches above the floor of the wind tunnel. The portion of the jet supply pipe below the plate and above the tunnel floor is housed in a 30 percent thick fairing which also contains the pressure leads.

### Air Supply

The cross wind is provided by the uniform stream of the wind tunnel. The jet air is supplied by a 100 H.P. centrifugal blower. The flow is first exhausted from the blower into a 6 inch diameter line, then passes through an orifice plate and a butterfly valve for controlling exit conditions, and finally passes through three screens and enters the supply pipe. A dump valve was installed at the blower exit in order to avoid compressor surge, and subsequent flow oscillations, when specified test conditions required a low mass flow at the nozzle exit. Figure 7 gives the blower performance curve provided by the manufacturer.

### Solid Blockage Model

It was considered desirable to make certain pressure measurements with the jet replaced by a solid blockage model. For this a thick-walled rubber hose was used with a 1.25 inch inside diameter, 2 inch outside diameter and 24 inches long. One end was press fitted to a one inch depth in the nozzle exit. The other had a fine wire attached and by clamping this wire to the trailing edge of the plate various curved paths could be obtained.

For the solid blockage oil flow studies, appropriately shaped right cylinders, five feet in length, were press fitted into the nozzles. The circular model was a 2 inch diameter aluminum tube and the non-circular one was constructed of wood.

### Probes and Support Mechanisms

Pressure measurements above the plate surface were made with a 1/4 inch diameter, five-port pressure probe, type DA-250, manufactured by United Sensor and Control Corporation (Figure 8). There is a cluster of five orifices (numbered  $P_1$  through  $P_5$ ) 1/2 inch from the end and the pressure measurements taken from them can be used to determine the pitch ( $0^\circ \leq \alpha \leq 360^\circ$ ), yaw ( $-40^\circ \leq \gamma \leq 40^\circ$ ), and the total and static pressure of the flow in which the probe is immersed. The details of this procedure will be given in the next chapter.

The pressure probe is supported by the traversing mechanism shown in Figure 9 so that its longitudinal axis is parallel to the plate and perpendicular to the free stream. The probe holder moves vertically, by remote control, along a lead screw inside the vertical support strut. A counter outside the test section measures the revolutions of the lead screw from which vertical position is determined. Positioning of the probe in the x-direction is conducted manually by pushing the vertical strut along the support slide until the desired position is achieved. Small studs fix this position during a test run. The small rail along the plate provides additional stability for the vertical strut. The probe is secured in a particular  $y$  position by the tightening of an adjustment nut on the probe holder; changes in this direction cannot be made remotely. The probe can also be rotated about its own longitudinal axis. A flexible cable leads from the block to a remote control station outside the test section for this purpose. The centerline of the vertical strut is located 18 inches from the  $y = 0$  plane and the probe

can be extended from this location to as far as 5.0 inches on the other side of the  $y = 0$  plane. Traversing in the longitudinal direction covers the range  $-12" \leq x \leq 36"$  while the vertical range is approximately  $6" \leq z \leq 48"$  and the rotational is  $0^\circ \leq \alpha \leq 360^\circ$ .

This probe support mechanism was also used to hold the total pressure rake shown in Figure 10. The rake has 12 individual total head probes, 0.058 inches in diameter and with 1/2 inch spacing.

Figure 11 shows a total head probe supported by a converted micromanometer stand. This was used for surveys of the exit conditions of the nozzles (free jet condition). A static pressure probe (not shown) was also used with this stand.

#### Pressure Switching Equipment

Approximately 10 feet of 0.063 inch Tygon tubing connects each static pressure tap on the plate with a port on a switching device (48J4 Scanivalve), which, by manual selection, is used to connect (internally) any one of the input pressures with a pressure transducer. The precision surfaces inside this switching device are lubricated by an oil wick and, during test operations, a suction pressure of approximately 10 inches of mercury is kept in the Scanivalve case in order to prevent oil leakage into the pressure lines.

The leads from the pressure probe enter a wafer model switching device (W1/2P-6T Scanivalve) which can select, for output to a transducer, any one of six differential input pressures. As opposed to the 48J4 Scanivalve, this latter model requires the application of a back pressure during test runs in order to keep adjacent precision surfaces,



within the wafer, sealed. The back pressure must be greater than any of the pressures being measured.

Two transducers were used to cover the range of pressures encountered in the pressure probe study. A second wafer model Scanivalve was accordingly connected to the first to provide the capacity to switch a selected differential reading to either of these transducers. Also the differential pressures will undergo sign changes during a test and, since the transducers operate best with a fixed sign on a differential input, a third wafer was connected in series to provide any such necessary polarity changes between test output and input to the transducer. A fourth wafer is added in order to make it convenient to rapidly check the zero setting of the transducer. The entire system is shown in Figure 12. Each wafer is operated by an individual solenoid drive, actuated by the push button on the control box.

#### Pressure Measuring Equipment

Pressures from the plate surface and the probe are measured with the Barocel Electronic Manometer System manufactured by Datametrix, Inc. It consists of two major components as shown in Figure 13, with the Model 1014 power supply and signal conditioner on the left and a pair of Model 511, variable capacitance, differential pressure transducers on the right. They respectively cover a range of 0 to 10 and 0 to 1000 millimeters of mercury. A reading from either of these may be made on the voltmeter in the 1014 unit, selection being determined by a manual sensor switch having gain positions from 1 to  $10^3$ . The voltmeter reads from zero to five volts, full scale.

Jet plenum pressure was measured by a mercury micromanometer and atmospheric pressure by an aneroid barometer. Temperature in the jet supply line was monitored with a simple bimetallic thermometer after the temperature drop to the plenum had been established.

### Flow Visualization

For the flow visualization studies conducted on the plate surface an oil mixture was used consisting of 1 part of linseed oil, 4 parts carbon black, 4 parts oleic acid, and 16 parts of number one diesel oil. It was found that this mixture gave the best results in that the amount of carbon residue left after a test run was sufficient to give an indication of the direction of flow near the plate surface (i.e., streamline traces). Also this mixture deposited more residue in regions of slower air flow, thus providing visual information about relative velocity magnitudes. In order to prevent this mixture from entering the static pressure ports a thin sheet of self adhesive white plastic was used to cover the surface.

Smoke visualization studies were conducted in a Model 960A.1 smoke tunnel, manufactured by Collins Radio Company, with a 2" x 24" glass encased test section (Figure 14). Smoke could be released anywhere in the flow field through a small, hollow tubed, hand held wand or injected into the jet supply line. Five different orifice shapes shown in Figure 15 were used, each manufactured with its own plate and settling chamber as one unit. The circular orifice, shown on the lower left, is 1/4 inch in diameter and the rest of the orifices are of the same cross-sectional area. The values of  $w/t$  are 0.08, 0.3, 1.0, 3.4,

and 11.8 respectively from left to right, top to bottom. Installation is accomplished by merely inserting the extension from the settling chamber into the plastic tubing which brings the jet air into the test section and taping the plate to the test section back wall. The plate is 6 inches long and completely spans the test section with its 2 inch width.

## CHAPTER III

### PROCEDURE

#### Test Technique

##### Installation

A few simple tests were conducted to determine the optimum position of the plate in the test section. It was considered desirable to keep the plate as close to the tunnel floor as possible in order to minimize any ceiling interference effects on the jet flow. However it was then necessary to examine the possible effects of interference from the support structure beneath the plate. Hence the design of the legs and support pipe for the aluminum plate, as described in the previous chapter, was dictated by the results of a test with a plywood plate of the same dimensions. Various support legs were tried until tufts on the upper surface demonstrated that smooth flow was present. The fairing, which can be seen beneath the plate in Figure 6, was concurrently tested and found to have no adverse upper surface interference effects. Pressure measurements from several chordwise and spanwise rows of static pressure taps in the upper surface were used to find the angle of inclination for the plate which produced a nearly uniform pressure distribution. This occurred at an angle of approximately  $-1.0^\circ$  relative to the tunnel floor (minus sign implies leading edge down). The same procedure using tufts and surface pressures (with jet off) was used when the aluminum plate was installed in the

position described in Chapter II. The average resulting surface pressure was one percent below  $q_\infty$  ( $C_p = -0.01 \pm 0.003$ ). The boundary layer was checked on the aluminum plate (at  $x/a = -5.0$ ,  $y/a = 0.0$ ) and found to be approximately one inch thick with a typical  $1/7$  power profile.

### Jet

The shape of the exit velocity profiles was investigated by using a total and a static pressure probe. For both the circular and non-circular jets the pressure profiles were found to be uniform within one percent with the total pressure probe and within two percent with the static probe. The probe and stand of Figure 11 were used for this test under free jet conditions. Sample measurements were made with and without the presence of another identical support stand located in an image position on the opposite side of the jet exit. The results verified that there was no interference effect on the free jet due to the support stand.

Mass flow as calculated from the integration of these profiles agreed within one percent with the mass flow as determined by the orifice meter method (Ref. 38). Hence, with acceptable accuracy, jet dynamic pressure at the exit  $q_j$  (needed for any particular  $\lambda$  value) could easily be determined by opening the butterfly valve until the appropriate exit total pressure  $P_{0e}$  was achieved. The governing equations used along with the procedure followed for setting the jet dynamic pressure are cited below.

First the wind tunnel dynamic pressure and the effective velocity ratio are selected. This in turn fixes the desired jet exit dynamic

pressure, i.e.,

$$q_j = \lambda^2 q_\infty .$$

Next consider the isentropic pressure ratio expression at the jet exit

$$\frac{P_{O_e}}{P} = \left( 1 + \frac{M_j^2}{5} \right)^{\frac{7}{2}}$$

where the value of 1.4 for the ratio of specific heats (for air) has been used and where the Mach number of the jet flow is given by

$$M_j = \left( \frac{10}{7} \frac{q_j}{P} \right)^{\frac{1}{2}}$$

Then assuming that the jet exhausts at atmospheric pressure  $P_a$  (with the wind tunnel breather,  $P_\infty \cong P_a$ ) one obtains

$$P_{O_e} = P_a \left( 1 + \frac{q_j}{3.5 P_a} \right)^{\frac{7}{2}} ,$$

or

$$P_{O_e} = P_a \left( 1 + \frac{\lambda^2 q_\infty}{3.5 P_a} \right)^{\frac{7}{2}} .$$

From this last equation curves of  $P_{o_e} - P_a$  versus  $P_a$  for various  $\lambda$  and  $q_\infty$  values were constructed (for typical example see Figure 16). Under cross-flow conditions the pressure in the plenum was used to monitor  $P_{o_e}$ . The difference between the pressure measured by the plenum tap and that at the jet exit proper was determined experimentally under free jet conditions. Temperature in the plenum stabilized at approximately 160° Fahrenheit. After this no further adjustment of the butterfly valve was necessary to keep a constant  $P_{o_e}$ .

### Surface Pressures

All data from the plate upper surface was taken in differential form, referenced to the static pressure in the undisturbed cross-flow  $P_\infty$ . That is, raw data has the form  $P - P_\infty$ . Except for a few special cases the wind tunnel was run at  $q_\infty = 1.07$  mm Hg (which, under standard sea level conditions, corresponds to  $V_\infty = 50$  ft/sec). The annular disk was rotated to successive radial settings, in 15° increments, in the range  $0^\circ \leq \beta \leq 180^\circ$ , and pressures were read on the twelve pressure taps located along a ray (Figure 3) at each of these angular settings. Additional readings were made with  $\beta = 195^\circ$  and  $\beta = 270^\circ$  as spot checks on the symmetry of the pressure distribution. On the non-circular nozzle flange, pressures were measured every 15° from the fixed positions shown in Figure 4. The circular nozzle flange, in the range  $0^\circ \leq \beta \leq 150^\circ$ , has a ray of taps only in 30° increments. The readings for intermediate, odd multiples of 15° are obtained, during a given test run, by momentarily closing the butterfly valve, loosening the nozzle hold down screws, and re-securing the nozzle after a 15° clock-

wise rotation. On both nozzle flanges enough pressure taps are included for symmetry spot checks at  $\beta = 195^\circ$  and  $\beta = 270^\circ$ .

### Pressure Probe.

The support slide installed in the ceiling of the test section (Figure 9) may be left in place while plate pressures are being measured. Tests were made with it in and out and there was no effect on these surface measurements. However the vertical support strut and the rest of the probe support mechanism were installed only when the pressure probe was being used. There was a small amount of interference effect noted when the orifice end of the probe was close to the vertical support strut. This will be discussed in the section on accuracy.

The probe is used in conjunction with calibration curves (Figure 17) which were generated in the nine foot wind tunnel at  $q_\infty = 1.07$  mm Hg. The procedure for employing the probe was as follows. It may be recalled that it was positioned in the flow field so that its longitudinal axis is perpendicular to the free-stream flow of the wind tunnel and parallel to the plate surface. The first step, after positioning the probe at the desired physical location, is to rotate it about its own longitudinal axis so that the differential reading  $P_2 - P_3$  equals zero (Figure 8). The number of turns of the flexible shaft to accomplish this is used to determine the pitch angle of the flow as measured relative to the free stream flow. Then the measurements  $P_1 - P_2$ ,  $P_4 - P_5$  and  $P_1 - P_a$  may be taken. The probe calibration curve (Figure 17a) of  $(P_4 - P_5)/(P_1 - P_2)$  can be used to determine  $\psi$ , the yaw angle of the flow. Subsequently this  $\psi$  is used with the calibration curve shown in Figure 17b to give the value  $q/(P_1 - P_2)$ ; and



knowing  $P_1 - P_2$  the local dynamic pressure can thus be calculated.

The calibration curves are good only for incompressible flow. They were found to be very sensitive to compressibility effects so no attempt was made to ascertain  $\gamma$  and  $q$  in high speed regions, such as in the jet near the exit. However, with the wind tunnel at  $V_\infty = 50$  ft/sec and with much of the flow outside the plume being near this value, there was an extensive area where these calibration curves were valid for use in determining local yaw and dynamic pressure.

Along the jet centerline only total pressures were measured with this probe. The calibration curve for the total pressure coefficient (Figure 17c) was found to be insensitive to compressibility effects encountered within the range of the investigation.

#### Rake

The total pressure rake was used to gather data that gave information about relative plume distortion as  $w/l$  was varied. The rake was positioned so that the line of total pressure probes was parallel to the  $x$  axis. Then, with the center probe set at  $z/a = 5$  the entire rake was rotated so as to be perpendicular to the jet path(s) at  $\lambda = 8$ . Readings were then taken at various  $y$  stations, from  $y = 0$  out to the edge of the plume.

#### Flow Visualization Techniques

Oil. The plastic sheeting described earlier was put on the plate, with the oil mixture subsequently applied in a thin, smooth layer with a standard paint brush. The wind tunnel and jet were then brought up to their respective speeds together. The average run time

needed for the oil traces to develop was approximately 10 minutes.

Smoke. In the smoke tunnel the jet velocity was slowed until the flow became laminar in order to aid visualization. This made velocity measurement impractical because of the low dynamic pressures involved and the following procedure was used to roughly set the jet speed. A plot of jet paths at  $\lambda = 4$  and  $\lambda = 8$ , scaled properly for a 1/4" diameter circular turbulent jet, was drawn on clear plastic which was taped to the glass on the test section of the tunnel. It was positioned such that the origin coincided with the actual jet exit. To attain a desired  $\lambda$ , the cross flow and jet speeds were then adjusted so that the center of the smoke trace followed one of the plotted paths. These control settings could be then held fixed during a nozzle change so that the same  $\lambda$  could be held for a non-circular case. Also, after fixing control settings for a desired  $\lambda$ , the smoke supply could be diverted from the jet air to the wand for injection into the cross flow.

#### Accuracy

The Barocel transducers have, as stated by the manufacturer, an accuracy of from 0.1 to 0.25 percent of reading. A dead weight tester (Consolidated Electrodynamics Corporation, type 6-201-0001) was used to check the transducers in the 10 mm Hg. and 1000 mm Hg. range. The results are shown in Figures 18 and 19. The dead weight tester is a primary laboratory standard and stated to be accurate within 0.025 percent of reading. (Additional research in this calibration area has led to the suggested use of the variable capacitance transducer as a standard). Frequent checks on the transducers were made during actual

test conditions, using wind tunnel  $q_\infty$  as the standard, which in turn was monitored by the wind tunnel operator on a Betz water manometer (reading uncertainly of  $\pm 0.03$  mm  $H_2O$ ). The jet plenum pressure is read on a mercury micromanometer, with a repeatability of  $\pm 0.005$  inches.

Measurement errors may originate from several sources. One is the finite diameter of the static pressure taps in the surface of the plate. Based on the finding of reference 40 this introduces an error of approximately  $\pm 0.5$  percent of  $q_\infty$  in the present investigation. Turbulence also has an effect on the accuracy of a mean static pressure measurement<sup>41</sup> but it is felt that in this study it is less than the reading error incurred in the measurement of the fluctuating static pressures. The mean voltage output was determined by visual integration of the needle fluctuations over an average interval of 10 seconds. (Response time was investigated concurrently with leak and continuity checks and found to be less than one second). The maximum range of oscillation for each reading was recorded and Figure 20 shows the typical resulting uncertainty band for different radials. This reading fluctuation band is approximately  $\pm 1.0$  percent  $q_\infty$  in the forward and far lateral regions and can average as high as 5.0 percent in the wake and very near the jet. The repeatability of the surface pressures from one installation to the next was within the fluctuation band, as was the symmetry (based on check readings along  $\beta = 195^\circ$  and  $\beta = 270^\circ$ ). Above the plate and away from the plume the reading fluctuation is the same as above.

Regarding fluctuations in the plume, Figure 21 shows a typical working drawing from which jet centerline paths were ascertained. Total pressure is plotted against  $z/a$  for various  $x/a$  stations. With reading fluctuation bands as shown, it is estimated that the maximum uncertainty in plotting jet paths is less than  $\pm 0.5a$ . Data taken with the pressure probe was repeatable, from one installation to the next, within the reading fluctuation bands.

Figure 22a presents a comparison of plate pressures (shown in contours of constant  $C_p$ ) with those of reference 22. Figure 22b compares jet paths as determined by the present investigation with those of references 16 and 17. It is felt that the agreement can be considered satisfactory when one considers the judgement factors involved in determining mean values.

The total head measurement  $P_1 - P_a$  from the pressure probe was checked against the same measurement made by a small total head probe (Figure 11), both taken near the (free) jet exit. This gives one confidence that the 1/4" diameter pressure probe is causing negligible interference effects on the total pressure readings. Regarding the  $P_1 - P_2$  and  $P_4 - P_5$  readings no test was made to ascertain the extent of probe interference in regions in and close to the jet where gradients are very steep. However data from these pressure ports is taken in the field away from the jet where deviations from  $q_\infty$  are not great and steep gradients are not present. In the author's opinion any interference in this latter region would be much less than the previously discussed fluctuation band.

Figure 23 shows the effect of the vertical support strut and probe holder on the pressure probe readings. For the  $y/a = 10$  measurement there is a 2.9 percent effect on  $q$  and  $1.0^\circ$  effect on  $\psi$ . Correspondingly the effects at  $y/a = 5$  are 2.2 percent and  $0.5^\circ$ .

Ceiling interference was considered negligible. This estimation was based on the findings of reference 16 where a 1.0 inch diameter jet and 0.5 inch jet were found to have the same paths (non-dimensionalizing by jet diameter) when issuing, at the same  $\lambda$ , from the floor of a 1' x 5' wind tunnel.

The blockage effect of the jet on the free stream velocity of the wind tunnel was calculated and found to be negligible using the procedure given in reference 42:

$$\frac{V_{\text{corrected}}}{V_{\infty}} = 1 + \epsilon$$

where,

$$\epsilon = \frac{1}{4} \left\{ \frac{\text{Frontal Area}}{\text{Test Section Area}} \right\}.$$

Using the conservative estimate that the jet presents a solid front to the free stream flow of 3.4" x 48" results in  $\epsilon = 0.004$ .

The accuracy of the rake measurements cannot readily be determined. A check in the free stream of the wind tunnel at  $q_{\infty} = 1.07$  mm Hg. showed the individual probes to be insensitive to pitch changes of  $\pm 12^\circ$ , but it cannot be stated what angularity the

probes experience in the jet plume, especially near the edges. However the objective of these particular tests was to compare relative plume distortion with varying  $w/l$ , and the agreement obtained with the more exact measurements of Jordinson<sup>16</sup> for the circular jet lend creditability to the comparative results for the non-circular cases.

## CHAPTER IV

### RESULTS AND DISCUSSION

The first section of this chapter presents the data collected as  $w/l$  and  $\lambda$  were systematically varied. The second section is concerned with the interpretation of this data and is especially oriented toward relating surface pressure changes to changes in the blocking and entraining properties of the jet.

#### Summary of Collected Data

Table 1 summarizes the test conditions for which surface pressures were measured. Table 2 shows the test conditions for measurements taken off the plate with the pressure probe, along with the range of coordinates covered by the various surveys. Table 3 summarizes the test conditions for the flow visualization studies. Each of these tables also contains an index of figures and tables where results can be found.

#### Surface Data

Surface Pressures. Figure 24 is a composite array of the major results of the plate surface pressure measurement program, the data being displayed in contour lines of constant  $C_p$ . Following a row from left to right represents increasing  $\lambda$  for a particular jet exit configuration (i.e., fixed  $w/l$ ) and following a column downward represents increasing  $w/l$  of the jet exit while at a fixed  $\lambda$ . (Large scale plots of these  $C_p$  contours may be found in the last figure of the

illustration section).

Figure 25 shows the surface pressure distributions around the solid blockage model (2.0 inch rubber hose described in Chapter II) for two cases: (1) the hose is bent to approximate the centerline path of a circular jet at  $\lambda = 4$  and (2) the hose is bent to approximate the path at  $\lambda = 8$ .

All  $C_p$  contours were cross-plotted from radial pressure distribution curves. In some cases it was necessary to investigate surface pressures along the radial  $\beta = 180^\circ$ , only, for  $\lambda$  values other than those cited in Figure 24. These results are shown in Figure 26 and will be discussed in more detail in the interpretation section.

Integrated Effects. Figure 27 presents the suction coefficient  $C_s$  which is defined as the average pressure coefficient, i.e.,

$$C_s = \frac{\int_0^\pi \int_{r_1}^{r_2} C_p r dr d\beta}{\frac{\pi r_2^2}{2}}$$

where  $r_1$  is the location of the static pressure port nearest the jet exit and  $r_2$  is the radial upper limit of integration. The suction coefficient can be used to compute the interference lift loss using the expression  $\Delta L = q_\infty S C_s$ . Integration was accomplished using the trapezoidal method with finite differences of  $\Delta r/a = 1$  and  $\Delta\beta = 0.262$  radians ( $15^\circ$ ). As can be seen from Figure 4 the value of  $r_1$  will differ depending on the jet exit configuration under consideration and will vary with  $\beta$ . In no case does the static pressure port actually measure



the pressure exactly at the edge of the jet so there is a inherent error in the  $C_s$  calculation procedure due to the omission of the region between  $r_1$  and the actual edge of the jet. However several estimates for  $C_p$  at the edge (via extrapolation of  $C_p$  versus  $r$  curves), followed by integration over the small region inside  $r_1$ , showed a change of less than one percent of  $C_s$ .

Figure 28 shows the variation in the center of pressure  $\bar{x}$  with  $\lambda$  and  $w/l$ . This center of pressure is defined as the point on the  $x$  axis through which the suction force appears to act. Hence

$$\bar{x} = \frac{\int_0^\pi \int_{r_1}^R C_p x r dr d\beta}{\int_0^\pi \int_{r_1}^R C_p r dr d\beta}$$

where  $R = 15.75"$ , the location of the outermost pressure port on the annular disk (see Figure 3). If one thinks of the plate surface as being inverted and thus the lower surface of a wing, then positive  $\bar{x}$  may be interpreted as causing a nose-up pitching moment.

Visualization. Figure 29 shows the photographs taken at the end of each oil film test. The darker regions, such as the diamond shaped areas immediately upstream of the jet, illustrate that the flow has a very small velocity or possibly is stagnated. The lighter regions, correspondingly, represent more rapid flow. The region of

reversed flow behind the jet observed during the oil flow run has been marked in one illustrative case,  $w/l = 1.0$ ,  $\lambda = 12$  (Figure 29g).

The circular ring showing around the nozzles in most of the photographs is merely the edge of the nozzle flange (Figure 3).

The region of reversed flow is confirmed by the tuft studies conducted on the plate. Figure 30 illustrates exemplary results. It is noted on the figure that there is a region of upflow behind the jet.

#### Plume Data

Jet Paths. The jet paths shown in Figure 31 are the loci of points of maximum total pressure in the jet plumes in the plane  $y/a = 0$ . The subsequent use of the term path will imply this definition. For any given  $w/l$  value penetration increases with increasing  $\lambda$  and, for fixed  $\lambda$ , penetration decreases with  $w/l$  increasing.

Decay of Total Pressure Along Jet Paths. A comparison of the rates at which total pressure decays along jet paths can be seen in Figure 32 for  $\lambda = 8$  and  $\lambda = 12$ . Results were not conclusive at  $\lambda = 4$  because the three curves fell within the reading fluctuation band. It can be seen that there is a relative positioning of the curves as a function of  $w/l$ , the streamwise jet having the slowest decay.

Distortion and Roll-up. Smoke studies are shown in Figures 33 and 34. Photography in these studies was very difficult especially for the case of Figure 34 where an accompanying sketch has been included to aid in interpreting the photographs. As mentioned in Chapter III, the conditions in the smoke tunnel are different than those in the nine foot tunnel and the Reynolds number range has been

greatly reduced in order to get laminar flow. Figure 33 shows smoke being ejected through jets with  $w/l$  values of 3.4, 1.0, and 0.3 respectively. Figure 34 illustrates the results when smoke is released through the wand (Figure 14) in the deflecting fluid just upstream of the plate leading edge. In this laminar flow case all three jets have roll-up and Figures 34(a) and 34(b) demonstrate that much of the entrained deflecting-stream fluid is entrapped by these contra-rotating vortices. (No satisfactory photograph was obtained for the circular jet in the case of upstream smoke injection. However it was observed that the flow pattern was similar to  $w/l = 3.4$ ). The streamwise jet rolls up in two places; once just aft of the leading edge shoulder and again at the trailing edge. The more slender jet of  $w/l = 0.08$  was also tested with the result showing the same double roll-up pattern.

For a more quantitative look at jet distortion the total head rake was used in the nine foot wind tunnel to collect data a few diameters away from the exit plane. Figure 35 shows representative results in the form of total pressure contours at a distance  $z/a = 5$  above the plate and perpendicular to the jet path. The contours for  $w/l = 0.3$  tend to confirm the double roll-up of the streamwise jet seen in the smoke tests in that they show distortion in the same regions where roll-up was observed in the smoke tests.

#### Flow Field Data

The term "flow field" is defined as any region above the plate and away from the plume. The term "lateral flow field" includes this definition plus the additional requirement that it be above the region

labeled "lateral" in Figure 2. Vertical traverses were made with the pressure probe in this lateral flow field region and the magnitude and direction of local velocities have been obtained. A display of the data at  $z/a = 6$  for various  $x, y$  locations is shown in Figure 36. Two graphs are used in each case, one giving the yaw of the velocity vector and the other relative magnitude in the form of dynamic pressure. The flow pitch angle can also be determined from the latter by noting the angle of the  $q$  vector.

Other data in the flow field above the plate has been collected primarily to provide more regions where the results of mathematical models can be compared with experiment. To this end an extensive flow field survey has been made for the case  $w/l = 1.0, \lambda = 8$ . The results (velocity components and total pressures) are listed in Table 4. A few remarks regarding this data will be given at the end of the interpretation section. In the lateral flow field region data has been collected for  $z/a > 6$ . This data will also be presented and discussed at the end of the interpretation section.

### Interpretation

In Chapter I it was cited that previous research had shown that the jet influences the surrounding surface pressures through some combination of its blocking and entraining properties but the manner in which these properties affected the surface pressure was still unknown. The purpose of this section is to bring attention to certain changes occurring in the data as  $w/l$  and  $\lambda$  are varied and to offer arguments relating these changes to relative changes in blockage and

entrainment.

The terms blockage and entrainment are defined below so as to delineate their specific meaning as used by this author. A blockage effect or "blockage" is meant to imply a flow field characteristic of that for flow around a solid body. Three right cylinders made of a solid material and of the same cross-sectional dimensions as the three nozzle exits, placed normal to the cross flow, have significantly different blockage effects on the flow field due to the solid body displacement. An illustration of these effects can be seen by comparing the three cases of solid blockage in the oil flow studies: as  $w/l$  increases there is a larger low speed region immediately upstream of the body, more diversion of the flow away from the body in the lateral regions and a wider wake region of separated flow. This is herein referred to as increasing blockage. The surface pressures are correspondingly affected by the blockage increase. With increasing blockage the high pressures immediately upstream increase in magnitude and extend over a larger area. There is a lateral extension of some of the low pressure to the side of the body. Also, the low pressures in the wake region cover a wider and longer (downstream) area. The surface pressures for the extreme cases of  $w/l = 0.3$  and  $w/l = 3.4$  ( $\lambda = 0$ ) are shown in Figure 37 and illustrate this trend. (This data was taken using a 24 inch long, wooden cylinder. It was of the same cross sectional shape as the exit of the non-circular nozzle and the tests were run with it press-fitted 0.5 inches into the nozzle exit.)

Entrainment is commonly associated with the increase of mass flow in the jet plume. In a free jet case this is related to a

spreading turbulent interface. However in the deflected jet case there are also the contra-rotating vortices whose pressure field sweep cross-flow fluid in toward the jet. Some of this fluid is mixed into the jet plume proper, but some is merely swept into the wake flow behind the jet. "Entrainment" as used here will imply the total effect of both vortex flow and turbulent mixing. It may be thought of as a sink effect which accounts for all forces tending to force cross-flow fluid in toward the jet and the wake.

#### Surface Pressure Changes

Forward and Lateral Regions. The discussion will first be directed toward the lateral and forward surface pressure trends occurring as one looks along a row of the  $C_p$  array in Figure 24, (i.e., the trends that result from  $\lambda$  being increased as  $w/l$  is held constant). It can be seen that under these conditions low pressures spread farther away from the jet in both the lateral and forward regions. At the same time the high pressure region immediately in front of the jet steadily diminishes in size. The objective is to ascertain what roles blockage and entrainment changes play in causing these trends. It may seem intuitive to argue directly that increased entrainment is the causal factor for the observed pressure changes inasmuch as previous investigators (Chapter I) have shown that the jet entrains more as  $\lambda$  increases. However the possibility of blockage changes occurring with  $\lambda$  increasing cannot be ruled out a priori. Even though  $w/l$  is being held fixed, the jet path is changing. Specifically, the path tends more toward the vertical as  $\lambda$  increases (Figure 31), and this movement could be responsible for some

blockage change. However the data presented in Figure 23 indicates that this change is relatively small. Here one can see that as the circular rubber hose is moved from a position approximating the path of the circular jet at  $\lambda = 4$  to an approximation at  $\lambda = 8$ , that there is an almost imperceptible change in the surface pressures directly upstream and only a slight change laterally. (The wake pressures will be discussed later.) Also, comparing contours of the same  $C_p$  magnitude from Figure 24 to Figure 23 it can be seen that the solid blockage model affects a much less extensive region around it than does the actual fluid jet. It is unknown to what degree the circular, bent hose represents the true blockage characteristics of the jet but qualitatively it seems valid to argue that surface pressure changes due to path changes only are small.

The results thus far seem to indicate that as  $\lambda$  is increased, with  $w/t$  fixed, the primary cause of the observed forward and lateral surface pressure changes is increased entrainment. There may be a very small contribution due to blockage change in the near lateral region.

Turning to the lateral field data this argument is reinforced. The yaw plots in Figure 36 can be used to ascertain the relative dominance of entrainment or blockage at the particular location where the data was collected. Specifically,  $\gamma$  outward indicates blockage dominance and  $\gamma$  inward represents entrainment dominance.

In Figure 36a the results furthest from the jet ( $y/a = 10$ ) are portrayed and the increase of  $\gamma$  inward with increasing  $\lambda$  demonstrates the dominance of entrainment effects under those conditions. In Figure 36b (where  $y/a = 4$ ) there can be seen a general shift (as compared to

Figure 36a) of the curves toward the  $\gamma$  outward direction hence showing that blockage effects are more important in the region near the jet. Generally however, the trend appears to be that, with increasing  $\lambda$ , entrainment eventually dominates.

It is not considered valid to draw much more from these graphs (Figure 36) than the general trends noted. Equipment limitations prevented flow field surveys below  $z/a \approx 6$  and there are undoubtedly changes occurring for  $z/a < 6$ . However extrapolation of data taken at  $z/a \geq 6$  values shows no basic changes to the general trends noted above. To demonstrate this, Figure 38 shows the effect of extrapolating to  $z/a = 3$  from the data taken at  $z/a \geq 6$  (upper graph). The upper graph in Figure 38 is extracted from Figure 44 in the "flow field data" sub-section below where data taken at  $z/a > 6$  is discussed. The case of  $w/l = 3.4$ ,  $y/a = 4$ ,  $x/a = 0$  was chosen because it exhibits one of the strongest variations of yaw as a function of  $z/a$  and is one of the few cases where extrapolation to  $z/a = 3$  results in a cross-over of  $\gamma$  values. The effect is shown by the solid symbol curve in the lower graph. The bow outward as  $\lambda$  is increased from 4.0 to 8.0 is no longer present. However, entrainment effects can be seen to become dominant with increasing  $\lambda$  and from other such extrapolations the general observation that relative blockage effects are stronger as one moves (laterally) closer to the jet can still be made.

The focus of the discussion now returns to the surface pressures of Figure 24 in order to interpret the  $C_p$  behavior under the conditions of increasing  $w/l$  with  $\lambda$  held constant. The most prominent trend occurring in the forward and lateral surface pressures as one looks down



a column in Figure 24 is the growth of the region of high pressures immediately in front of the jet. This is indicative of a blockage increase which could arise from two sources: (1) the change of jet path location under these conditions (Figure 31); (2) the increase of the bluntness of the jet shape. The first source is an unlikely candidate as a major cause. The reason is that the variance in the position of the jet path under these conditions of  $\lambda$  fixed,  $w/l$  increasing is less than the change in path occurring when  $\lambda$  is varied with  $w/l$  fixed which has been shown (Figure 25) to have a very small effect on the upstream surface pressure. Hence the second source is the most probable primary causal factor.

To what extent entrainment is varied under the condition of  $w/l$  increasing with  $\lambda$  fixed, is not readily apparent from the surface pressures. This will be discussed later in the sub-section on plume behavior.

To summarize the interpretation thus far regarding the forward and lateral regions: the changes in the surface pressure distribution, with  $w/l$  fixed and  $\lambda$  increasing, are primarily due to the increased entrainment strength of the jet, with some small changes resulting from blockage effects being evidenced close to the jet; pressure changes occurring as  $w/l$  increases and  $\lambda$  is held fixed are primarily due to blockage increases associated with increasing bluntness.

Wake. Jordinson<sup>16</sup> found that the total pressure is less than  $P_0$  in a wake region behind the jet. The fact that his data shows the total pressure loss decreasing with increasing  $\lambda$  lends creditability to his suggestion that the phenomenon is analogous to that occurring for a

cylinder with suction.

Returning to Figure 24 of this report, the wake surface pressure changes with  $\lambda$  increasing,  $w/l$  fixed, tend to confirm Jordinson's suggested analogy. It can be observed that along a row of the  $C_p$  array there is a decrease in the distance to which the low pressure contours extend downstream in the wake region. (An exception to this trend occurs at  $w/l = 3.4$ ,  $4 \leq \lambda \leq 8$  which will be discussed shortly). This behavior is indicative of a relative increase in entrainment effects.

It could also be argued that this trend is indicative of some blockage change as  $\lambda$  increases. However, Figure 25 shows that the blockage change associated with the change in path of the solid rubber hose is opposite from that shown along a row in Figure 24. That is, the wake  $C_p$ 's for the hose extend further downstream as its path is changed to represent increasing  $\lambda$ . It is important to note here that term blockage change is not meant to be synonymous with blockage increase. The distinction in the use of these terms lies in the concurrent behavior of the surface pressures in the forward region as the hose is positioned to represent increasing  $\lambda$ . Here, there is no distinct increase in the area that the high pressures cover, which was a characteristic included in the definition of "blockage increase" stated earlier. Therefore this wake pressure behavior behind the hose does not, by itself, fulfill the complete blockage increase definition.

However the present specific argument requires no more than to show that changes in the wake pressures associated with the path change of the hose are opposite to those occurring with the comparative changes in the path of the fluid jet. This leaves an increase in the dominance

of entrainment effects as the most likely source for causing the pressure trends observed in the wake as  $\lambda$  increases. This interpretation is in turn compatible with that given for the behavior, under the same conditions, in the forward and lateral regions.

The changes in wake surface pressure under conditions of increasing  $w/l$  and constant  $\lambda$  can be related to an increase in blockage domination. These wake pressure changes, in conjunction with those in the forward region, exhibit the trends as given earlier in the definition of blockage increase. It could be reasoned that entrainment decreases would give similar effects. However it will be argued later, in the sub-section on plume behavior, that entrainment actually increases slightly when  $w/l$  is increased.

The interpretation of the behavior of surface pressures in the wake region is hence consistent with the stated hypothesis regarding the forward and lateral surface pressure: changes occurring with  $\lambda$  increasing and  $w/l$  fixed are brought about by a relative increase in the dominance of entrainment effects; changes in the pressure distribution brought about when  $w/l$  is increased and  $\lambda$  held constant are due to a dominant increase in blockage effects.

Returning now to the earlier excluded case of  $w/l = 3.4$ ,  $4 \leq \lambda \leq 8$ , Figure 24 shows that, as  $\lambda$  increases from 4.0 to 8.0 for the blunt jet, the low pressure contours extend further downstream. This is opposite to the trends occurring elsewhere in Figure 24 (for  $w/l$  fixed,  $\lambda$  increasing). However, it is consistent with the trends resulting as the path of the rubber hose (Fig. 25) is adjusted so as to represent path changes occurring with increasing  $\lambda$ . This suggests that, if a

relatively low  $\lambda$  value and high  $w/l$  value are occurring in the right combination, blockage changes can supercede entrainment increases (as far as their influence on wake surface pressures are concerned) as  $\lambda$  is increased.

For more detail Figure 26(a) shows the results of an investigation of surface pressures made directly behind the blunt jet ( $\beta = 180^\circ$  only) at several  $\lambda$  values other than those shown in Figure 24. Notice that the solid blockage behavior appears to dominate as witnessed by the low pressures continuing to extend further downstream until  $\lambda \approx 8$ . At that point entrainment effects begin to overcome the blockage effects and the low pressures begin to decrease their distance of downstream extension as  $\lambda$  is increased above 8.0.

Figure 26(b) shows that the circular jet exhibits the same behavior, only the point at which entrainment effects appear to become dominant occurs in the vicinity of  $\lambda = 4.0$ .

A generalized description of wake pressure behavior is, in this author's opinion, as follows: Beginning at a relatively low  $\lambda$  value some combination of blockage and entrainment effects determine the pressure distribution. As  $\lambda$  is slowly increased entrainment increases but initially not enough to supercede the blockage change in the wake associated with changing plume path. However as  $\lambda$  increases even further, entrainment does eventually become strong enough to arrest the downstream growth of the low pressures. The level of  $\lambda$  required for this arrest increases with increasing  $w/l$ . As  $\lambda$  is increased above the arresting level the behavior is roughly analogous to sucking on a cylinder. That is, as  $\lambda$  is increased, there is a gradual increase in the

magnitude of the pressures in the wake region as well as a reduction of the distance to which these low pressure contours extend downstream.

Plume Behavior. It was suggested earlier that it might be possible to attribute the surface pressure behavior, exhibited as  $w/l$  increases with  $\lambda$  fixed, to a decrease in entrainment rather than the stated interpretation of an increase in blockage effects. It will be argued in this section that, with  $\lambda$  constant, entrainment actually increases as  $w/l$  increases. This interpretation is witnessed by the relative variation (from one  $w/l$  value to the next) of the total pressure decay along the jet path and by the relative behavior of the distortion and roll up properties of the jet plumes.

Before discussing the plume total pressures for the deflected jet, attention is called to Figure 39 (taken from reference 43). There the research was concerned with free jets and the investigators have measured both entrainment and centerline velocity decay for circular and non-circular jets of the same cross sectional area. Comparing the graphs of velocity decay and entrainment one can observe that there is a correlation between the results in that the jet which entrains more also exhibits the steeper velocity decay curve. This appears reasonable inasmuch as increased entrainment implies increased mixing, which, in turn, would be expected to cause an increase in the amount that the plume velocities are attenuated.

Regarding the deflected jet it is felt that the same reasoning may be applied; that is, that relative jet velocity decay may be used to infer relative mixing rates. It has been assumed here that total pressure decay curves will be relatively positioned (as  $w/l$  is varied)

in the same manner as centerline velocity decay curves. Therefore, the jet path total pressure curves (Figure 32) showing that the total pressure decays more rapidly as  $w/l$  increases are indicative of increased mixing. This, in turn, implies that the greater the  $w/l$  value the more the entraining strength of the jet.

The above argument can be further strengthened with some comparison of plume distortion (Figure 35) and the roll-up observed in the smoke studies. The latter indicate that a great deal of the entrained cross-flow fluid is found in the contra-rotating vortices (Figure 34). It may be recalled that the smoke tunnel velocities have been reduced to a level sufficient to obtain laminar flow. Hence this apparent dominance of vortex induced entrainment may be due to an absence of the turbulent mixing mechanism. However, it can be seen in Figure 35, where plume distortion data has been collected under turbulent conditions (jet Reynolds number is  $4.2 \times 10^6$ ), that regions where the distortion is greatest correspond to regions of roll-up in the smoke studies. Further it can be noted that the total pressure gradient is less steep in these roll-up regions than elsewhere. This in turn implies more mixing, hence more entrainment, has occurred in the roll-up regions by the time the jet plume reaches the particular  $s/a$  level at which the survey was conducted. Next it can be noted that the low-valued surface  $C_p$  contours shown close to the lateral edges of the jets (say at  $\lambda = 8$ , Figure 24) have positions which correspond to the relative location of the roll-up. The magnitude of these  $C_p$  contours decreases with  $w/l$  increasing thereby demonstrating that local velocities are increasing in the same manner. With the assumption that the

increase in these local velocities implies an increase in vortex strength associated with the roll-up the argument offered is as follows: The roll-up mechanism is a prime contributor to the overall entraining strength of the deflected jet; the strength of roll-up increases with  $w/l$ , therefore entrainment increases with  $w/l$ .

It must be emphasized that neither of the arguments stands alone as being conclusive, but the interpretation given for the distortion and roll-up behavior coupled with the arguments given in analyzing the total pressure decay do lend strength to the argument that for  $\lambda$  fixed entrainment increases with increasing  $w/l$ .

There is another factor which may play a role in relative entraining strengths and that is the rear surface area of the jet. The smoke studies indicate an increasing amount of entrainment of fluid into the aft portion of the plume as  $w/l$  increases. It may be possible that, for a  $w/l$  range which extends beyond that investigated here, entrainment variation with  $w/l$  would correlate directly with the increase in aft-facing area of the jet.

Another question remains. How appreciable is this entrainment variation with  $w/l$ ? It may be recalled that, in the argument regarding the cause of the wake surface pressure changes, the evidence was generally in favor of a blockage increase (as  $w/l$  increased with  $\lambda$  fixed). It only remained, in this section on plume behavior, to show that entrainment was not decreasing under those conditions. However with plume data indicating an entrainment increase with  $w/l$  increasing, but with surface pressure data indicating a blockage increase, the implications are that the entrainment increases with increasing  $w/l$  are

relatively small.

A brief summary of the interpretation given thus far is as follows: As  $\lambda$  is increased for  $w/l$  fixed the observed changes in the surface pressure distributions are attributable, generally, to the increased entraining strength of the jet. Some evidences of blockage increases appear in close to the jet but they are very slight relative to the major effects of entrainment. Blockage changes occurring with  $\lambda$  increases do appear in the wake region for  $w/l = 3.4$  and  $4 \leq \lambda \leq 8$ . Above  $\lambda = 8$  entrainment effects dominate in all regions. The circular jet shows a similar correlation of wake pressures and blockage changes as  $\lambda$  is increased from 3 to 4, but again with increased entrainment strength being the dominant influencing factor on surface pressures for  $\lambda > 4$ .

Where  $\lambda$  is held fixed and  $w/l$  increased, the plume data suggests a slight increase in entraining strength, but the behavior of the surface pressures demonstrates a dominant influence of the blockage increase that occurs as the jet bluntness is increased.

The arguments for  $w/l$  fixed,  $\lambda$  increasing are in general agreement with those presented in reference 44 where a two dimensional potential flow model has been used to make a parametric study of the relative importance of blockage and entrainment effects on surface pressures. It is noted by that author that the relative dominance of entrainment over blockage can be mathematically related to the character of the singularities used. The influence of the doublet used to represent blockage decays with the square of the distance from the jet whereas the influence of a sink decays only by the first power of this distance.



As a side comment it is noted here that an effort was made to explore the possible correlation of surface pressures with jet path location. The hypothesis being tested was that the location of the contra-rotating vortices in the plume was the dominating factor of influence on the plate pressure behavior. No correlation was found. Figure 40 illustrates one of the salient counter examples where conditions of  $w/l = 3.4$ ,  $\lambda = 8$  and  $w/l = 1.0$ ,  $\lambda = 6.8$  yielded almost coincidental jet paths (Figure 31) but very different surface pressure distributions. A more detailed discussion of this tested hypothesis is given in reference 45.

Integrated Effects. Figure 27(a) indicates that the magnitude of the coefficient  $C_s$  increases with increasing  $w/l$  values; and that for fixed  $w/l$  the suction increases as  $\lambda$  increases. The trends in Figure 27(a) also suggest that there is a maximum which occurs as a function of  $\lambda$ . Figure 27(b) illustrates this peak more definitively and shows that its occurrence is related to the value of  $r_2/a$  for a particular exit configuration. This extremum can be anticipated by observing the behavior of the surface pressure distributions. It can be seen in Figure 24 that even though low pressures continue to extend further into the lateral and forward regions with increasing  $\lambda$ , the low pressures close to the jet concurrently experience a rise. Figure 27(b) shows that the lower the value of  $r_2$  used to evaluate the  $C_s$  integral, the sooner the peak occurs as a function of increasing  $\lambda$ .

This rise in the pressures close to the lateral edge of the jet can be explained using the earlier arguments about the relative dominance of entrainment and blockage. As the effects of entrainment increase over

those of blockage (with  $\lambda$  increasing) the flow close to the jet is subjected to less curvature. However at the larger  $r$  locations (blockage effects having decayed rapidly with  $r$ ) increasing entrainment is manifest in the slow decrease in pressure with increasing  $\lambda$ .

Many considerations go into the design of a complete aircraft configuration, thus making it difficult to extend the results obtained here into the realm of design. However a few comments in this vein are offered with regard to the trends indicated by the suction coefficients. Figure 27 indicates that the streamwise configuration causes the least interference loss. Construction of such a shape on a large scale may prove difficult, but a similar effect could be accomplished with two circular nozzles in a close tandem arrangement. On the other hand, the blunt jet may become desirable if, structural problems notwithstanding, it could be placed near the trailing edge of a wing lower surface. Such a location begins to approach a jet flap configuration which is the optimum arrangement for the relative positioning of thrust efflux and a wing.

It may be recalled from the introductory remarks of Chapter I that the interference losses are of practical aerodynamic importance when flight speed is slow enough to cause a reliance on vertical thrust for much of the lift force. Accordingly, the interference lift loss as a percentage of vertical thrust component becomes a variable of prime practical interest. This term,  $\Delta L/T$ , is evaluated using  $C_g$  as follows:

$$\frac{\Delta L}{T} = \frac{\frac{1}{2} \rho_\infty V_\infty^2 S C_s}{\rho_j V_j^2 \pi a^2}$$

where  $S$  is the area of the wing surface in question. In the present study

$$S = \pi r_2^2$$

so

$$\frac{\Delta L}{T} = \frac{1}{2} \left\{ \frac{(r_2/a)^2 C_s}{\lambda^2} \right\}$$

Figure 41 shows the results of this expression using  $1/\lambda$  as the abscissa. This usage is commensurate with the literature on aircraft configuration studies where increasing  $1/\lambda$  represents increasing forward flight speed at constant thrust. The figure demonstrates that, as a percentage of thrust, lift loss increases with increasing  $(1/\lambda)$ . Hence the region of most serious lift loss, practically speaking, is where  $\lambda$  is small. In light of earlier arguments, this means that much of this loss is associated with the extensive low pressures existing in the wake region which arise when the blockage properties of the jet are dominant. Thus devices which will reduce the extent of the low pressure region in the wake of the jet will help reduce the lift loss in this  $\lambda$  range. One

might think analogously in terms of methods of reducing the drag on a solid cylinder, but care must be taken that any remedy steps do not at the same time cause adverse entrainment effects. For example, one common method of reducing cylinder drag is to add a trailing edge fairing. However this would very likely cause a change in the entrainment effect normally experienced by fluid in the wake region and the net result might be no improvement or even more lift loss.

The results of a satisfactory corrective modification are shown in Figure 42, taken from reference 26. In this arrangement, fences with a height of one jet diameter and streamwise length of two diameters are placed on either side of the jet as shown. The authors of that paper suggest that the favorable results occur because the fences delay the growth of the vortex flow behind the jet. It is this author's opinion that, speaking in terms of blockage and entrainment, the favorable effects result more directly from the fact that the fences attenuate the sharp pressure drop usually experienced on the lateral edge of the jet. This in turn results in higher wake pressures and hence less total suction force on the lower surface. At the same time that this blockage-induced suction is being attenuated the fences do not alter the entrainment effect of the jet appreciably as witnessed by the exposed downstream surface of the jet.

Another important point is brought out when using the  $\Delta L/T$  variable regarding the effect of the ratio of jet size to wing surface area. Referring to Figure 27(b) one can see that the suction coefficient increases with diminishing  $r_2/a$ , the upper limit of integration. However

when  $\Delta I/T$  is calculated (Figure 41) the trend is reversed because of the corresponding surface area reduction and thus practically speaking it becomes desirable to keep the  $r_2/a$  ratio small. (As a cautionary remark, it is noted that finite wing effects cannot be evaluated here.)

#### Flow Field Data

Extensive Survey for  $w/l = 1.0$ ,  $\lambda = 8$ . This survey was conducted primarily to provide data for checking the results of mathematical models. Within the range,  $-5 \leq x/a \leq 16$ ,  $1 \leq y/a \leq 10$ ,  $6 \leq z/a \leq 30$ , approximately 324 data points have been taken with each data point providing three components of velocity (expressed in terms of  $q$ ) and total pressure. Figure 43(a) shows graphically a small sampling of this data; the complete set being listed in Table 4. It can be seen here that flow at the highest  $z/a$  stations is being pushed upward and outward, or away from the jet path, by blockage effects. As  $z/a$  decreases the outward component becomes greater and eventually an increase in  $P_o$  shows that the plume has been pierced by the vertical cut. Continuing downward one sees the vector swing in toward the jet, for example at  $x/a = 10$ ,  $y/a = 6$ ,  $z/a = 12$ . Here the  $P_o$  value is still slightly greater than  $P_{o_{\infty}}$  indicating the data point is on the fringes of the plume. The lowest  $z/a$  point indicates a flow component that is in toward the jet, but the fluid is not in the plume proper nor wake as indicated by the  $P_o/P_{o_{\infty}} = 1.00$  reading.

The vortex roll-up in the plume and its influence on adjacent cross flow fluid can be seen more clearly by plotting only the  $y$  and  $z$  components of the  $q$  vector. Figure 43(b) shows this type of illustration

in the  $x/a = 10$  plane. The view shown is as one looks in an upstream direction into this plane with the resultants of only the  $q_y/q_\infty$  and  $q_z/q_\infty$  components shown. The roll-up in the plume proper is then made clear by locating the vectors with  $P_o/P_{o_\infty} > 1$ . The influence of the roll-up on cross-flow fluid can then be seen by noticing the similar vortex-type pattern of the flow where  $P_o/P_{o_\infty} = 1.00$ . Only representative points have been shown to avoid cluttering the figure. If one were to plot additional points (from Table 4) with values where  $P_o/P_{o_\infty} < 1$ , a wake region becomes discernible. The outer boundaries of this wake roughly coincide with the heavy lines of separated flow seen in the surface oil film tests (Figure 29). (One can also plot more points, from Table 4, where  $P_o/P_{o_\infty} > 1$  if a map of the plume shape is desired.)

The mechanical limits of vertical traverse for the pressure probe were such that investigation could not be made below  $z/a \approx 6$  (occasionally  $z/a = 5$  was achieved). However, the oil flow tests (Figure 29) and flow visualization studies conducted just above the surface in reference 46, indicate a smaller roll-up near the plate with a circulation opposite to the larger vortex in the plume. Figure 43(c) depicts this smaller vortex (see region F) included in an illustration which represents this author's interpretation of the flow pattern on and near the surface. This interpretation is as follows: Oncoming cross-flow fluid from an upstream direction is diverted by the blockage effect of the jet (region A). It begins to accelerate much as it would under blockage conditions only, but with the jet this acceleration is more rapid due to entrainment which is predominant on the lateral and downstream edges of the jet. Much of the cross-flow fluid close to the

jet is entrained along the lateral edges. This fluid spirals in an upward path as it is drawn into the plume roll-up (region B). At region C, on the plate surface, there is a dividing streamline ( $m - n$ ) which stagnates upon reaching the wake boundary line ( $p - q$ ). Flow on the surface which is upstream of  $m - n$  moves back toward the jet ( $r - s$ ), while that on the downstream side turns away from the jet ( $t - u$ ). (lines  $m - n$  and  $p - q$  can be seen distinctly in a majority of the oil pictures.) Some fluid just slightly above the surface at region C separates and starts to rise as it enters the wake, still under the influence of entrainment. It meets similar flow coming from the opposite side of the jet (i.e., reflects from the plane of symmetry) in region D. It turns downward and divides again, leaving evidence of a stagnation region in the oil. The flow that is still responding to entrainment rolls up as it continues forward (region E) and eventually flows into the large vortex. The downward flow at D that cannot make the turn, breaks away and continues downstream inside the wake, forming another roll-up pattern (region F). Both of the roll-up formations (E and F) have components which stagnate with opposing components of the fluid on the outside of the wake boundary. This causes the wake boundary ( $p - q$ ) to appear darker than it normally does behind a solid body.

Tufts studies suggest that the behavior just described at D exists very close to the plate. The majority of the flow exhibits a large upflow component (region H) as witnessed by the tuft studies on the plate (Figure 30) and a single tuft on the end of a wand. Since the surface pressures exhibit no rise in this region, the accelerating

up-flow component appears to be the dominant influencing factor on the local pressure distribution.

Lateral and Forward Regions. The lateral field data at  $z/a = 6$  was presented and discussed earlier. Figure 44 extends the presentation of this data into regions where  $z/a > 6$ . One of the most pronounced features exhibited here is the pitch of local vectors, which increases in a downward manner as  $\lambda$  is increased. This suggests that entrainment is strongest at small  $z/a$  values, and as  $\lambda$  is increased this behavior becomes more pronounced. Blockage changes may be entering into this downward pitching, however. Additional data from solid blockage models is needed in this region before more definitive arguments can be made.

Directly upstream of the jet several solid blockage surveys were made with the rubber hose approximating the jet path at  $\lambda \approx 4$  and  $\lambda \approx 8$ . The results are shown in Figure 45. These can be compared, in Figures 46(a) and 46(b), with the flow field behavior occurring when the path of the actual fluid jet is changed from  $\lambda = 4$  to  $\lambda = 8$ . This comparison demonstrates that solid blockage changes associated with changing plume path (i.e., increased penetration) cause a very slight upflow, whereas penetration increases, which result from increased  $\lambda$  in the real fluid jet case, cause a downflow. Thus, on the upstream centerline, the downward pitch exhibited in the flow field behavior appears to be due to a relative dominance of entrainment at low  $z/a$  values (along the jet path).



## CHAPTER V

## CONCLUSIONS

The jet influences the surface pressure distributions through a combination of blockage and entrainment effects on the cross flow. Oncoming cross-flow fluid near the surface decelerates due to the blockage effect as it approaches the upstream side of the jet, giving rise to a region of high pressures in that region. It is then diverted around the side of the jet and attains high velocities in the lateral regions, causing a drop in pressure. Entrainment of cross-flow fluid into the plume primarily occurs along the lateral and downstream edges of the jet. A wake region exists behind the jet consisting of low surface static pressures and total pressures which are below that of the undisturbed cross-flow.

When the effective velocity ratio is increased, the blocking effect on the cross flow changes due to a change in the plume location (more penetration) and the entrainment effect increases due to an increase in the  $V_j - V_\infty$  difference. The way in which surface pressures respond to these changes depends on the effective velocity ratio  $\lambda$  and the width-to-length ratio of the jet exit  $w/l$ . When the effective velocity ratio is increased from  $\lambda = 4$ , for the circular jet, the blockage changes are minimal and the observed changes in the pressure distribution are attributable to a relative dominance of increased entrainment effects. These pressure changes are : (1) a decrease in the

region over which the high pressures exist immediately upstream of the jet and a decrease in their magnitude; (2) an increase in the radial distance both upstream and laterally to which low pressures ( $C_p < 0$ ) extend; and (3) an increase in the magnitude of the low pressures in the wake region, with an accompanying decrease in the distance to which these pressure contours extend downstream.

When the effective velocity ratio of the bluff jet ( $w/l = 3.4$ ) is increased above the level of  $\lambda = 4$ , entrainment increases are the dominating factor of influence on surface pressure changes in the forward and lateral regions just as with the circular jet. But variations in the wake pressure distributions are influenced by a relative dominance of the blockage changes accompanying the change in plume location. For  $\lambda$  increasing in the range  $4 \leq \lambda \leq 8$  this blockage change causes low surface pressure contours in the wake to extend further downstream. For  $\lambda > 8$  entrainment increase is the dominant factor of influence on surface pressure changes in all regions and the pressure behavior is the same as that for the circular jet.

The changes in wake pressure distribution behind the circular jet, as  $\lambda$  is increased from 3 to 4, exhibit the same blockage-dominated behavior as described for the bluff jet in the range  $4 \leq \lambda \leq 8$ .

The generalized behavior is one of entrainment effects playing the dominant role in causing the observed pressure changes occurring with  $\lambda$  increases. However, in the wake region, this dominance requires that a specific level of  $\lambda$  be achieved before entrainment noticeably changes the effects of blockage. This required level increases with the increasing bluntness of the jet exit shape.

The total suction force (or lift loss), as determined by integration of the measured pressure distributions, increases with increasing  $w/l$ . When this lift loss is presented as a percentage of the gross thrust of the jet ( $\Delta L/T$ ) the greatest lift loss occurs for all three jets in the lower  $\lambda$  range. As  $\lambda$  increases  $\Delta L/T$  improves primarily due to an attenuation of the suction forces in the wake region.

## APPENDIX A

### NOZZLE DESIGN

For the circular nozzle the contraction from the six inch supply pipe to the two inch diameter at the nozzle exit was accomplished in a streamwise distance of 7.45 inches using one of a family of contours recommended in reference 47 (see Figure A-1(a)).

A literature search indicated a dearth of reports dealing with subsonic noncircular nozzle design, particularly when a cross-sectional shape change must be concurrently accomplished. The design method first attempted by this author was based on a criterion of constant curvature at the throat region with this curvature being again selected from reference 47 (see Figure A-1(b)). However, as can be seen in Figure A-2(a), the amount of the contour template that can be used to shape the portions of the nozzle upstream from the throat region will vary depending on peripheral position. For example, working from a position midway on the straight side of the exit, the contour of Figure A-1(b) can be used in its entirety. But working from the narrow edge of the exit periphery only a small portion of the recommended contour shape can be used before terminating at the outside diameter limit (as set by the 6" ID supply pipe). When filling in the rest of the contours, a scalloped effect to the nozzle shape was generated as shown in Figure A-2(b) by the dashed lines.

During construction of this nozzle painstaking efforts were taken to ensure symmetry about the major and minor axes. Preliminary check-out

tests, under free jet conditions indicated uniform exit flow conditions. However, the unsymmetrical behavior exhibited when the jet was subjected to a cross flow (oil film test, Figure A-3) confirmed that the exit flow was unsatisfactory. It was felt that the particular contour design was giving rise to swirl in the jet flow. This conjecture was strengthened when honeycomb, inserted in the nozzle exit, yielded a symmetrical flow field.

Another nozzle was constructed which proved to be satisfactory. This time the contour of Figure A-1(b) was used again from the midpoint of the straight side of the exit periphery but the criterion of constant curvature around the periphery of the throat region was relaxed. Instead it was considered desirable to avoid the scalloped effect previously described and shape the nozzle so that the transition of cross-sectional shape from circle to slot was accomplished in as smooth a manner as possible. Figure A-4 gives a one quadrant, top view of the cross-sectional templates that were used to shape a wooden mandrel.

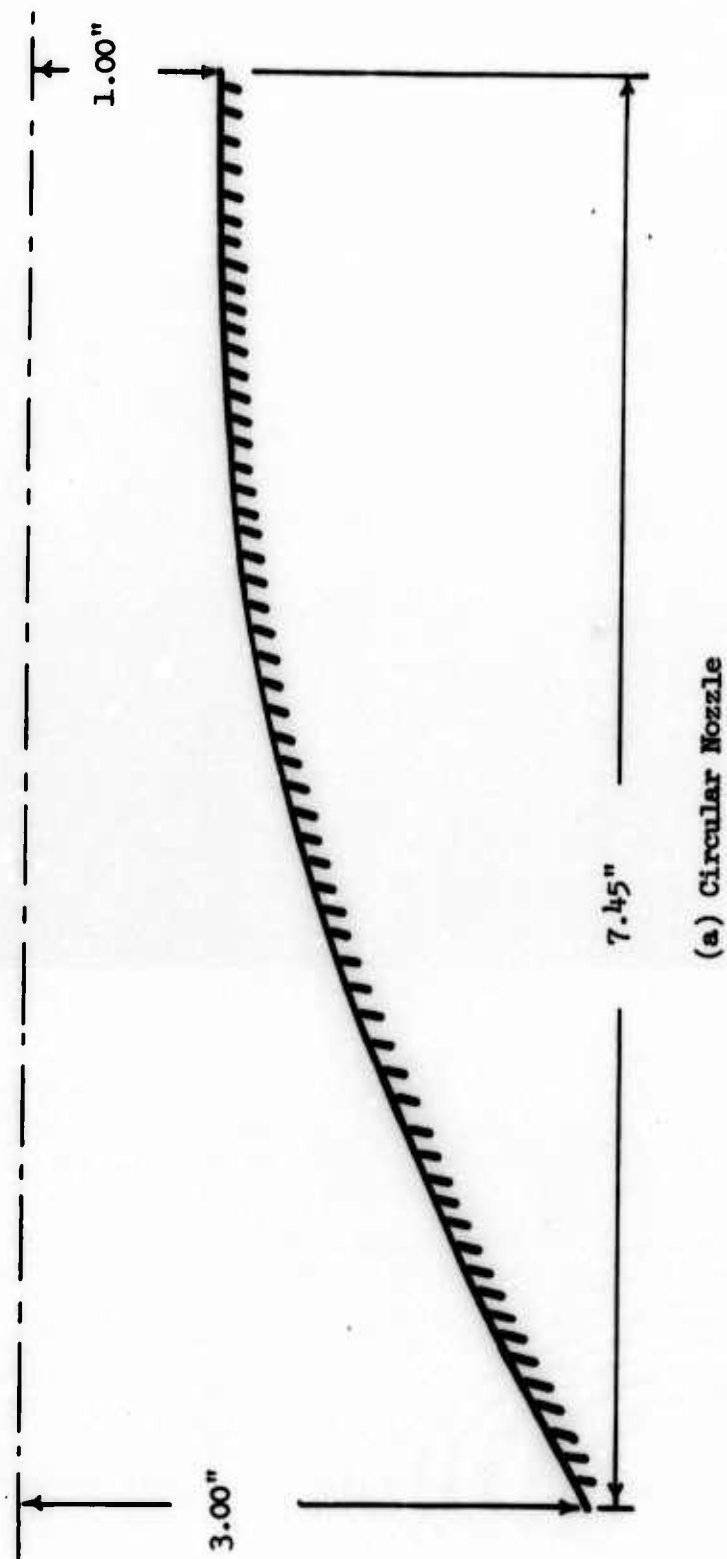
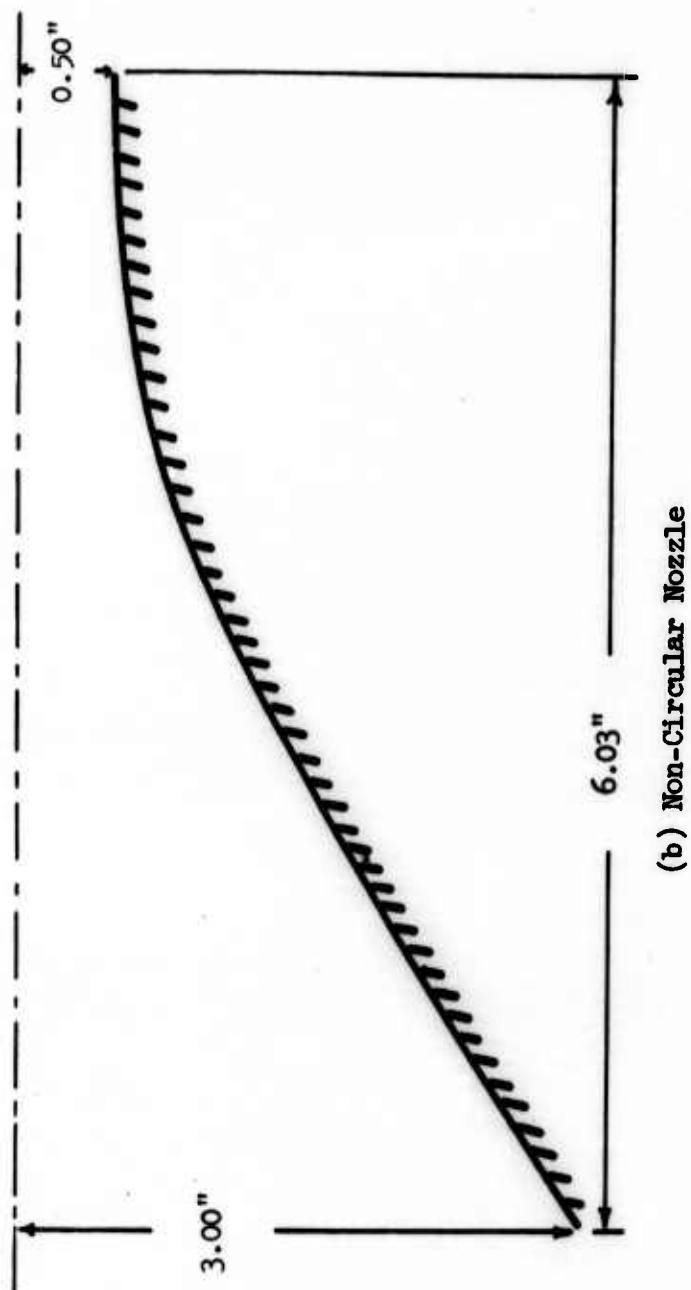
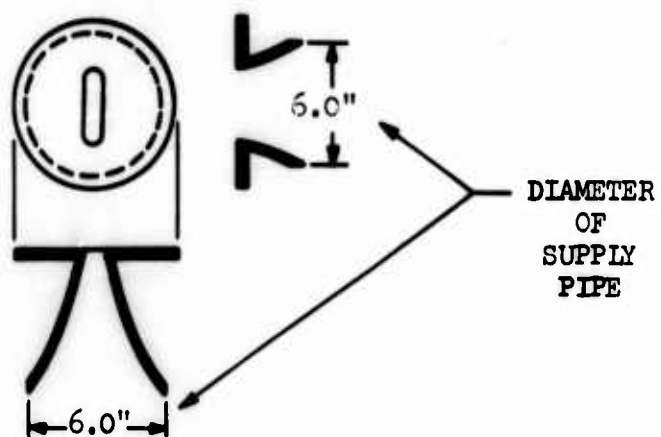


Figure A-1. Nozzle Contours.



(b) Non-Circular Nozzle

Figure A-1. Nozzle Contours (Concluded).



(a) Useable Contour Length as a Function of Peripheral Position.



(b) Resulting Scallop Effect.

Figure A-2. Non Circular Nozzle, Original Design.





Figure A-3. Oil Visualization at  $\lambda = 8$ , Original Design.

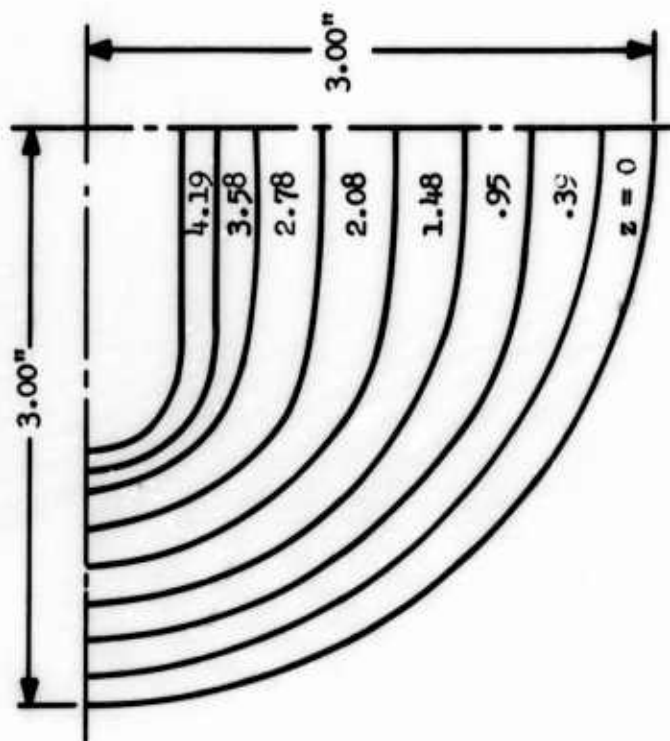


Figure A-4. Cross Sectional Template Shapes, Modified Design.

## CITED LITERATURE

1. Margason, R. J. and Gentry, G. L., "Aerodynamic Characteristics of a Five-Jet VTOL Configuration in the Transition Speed Range," TN D-4812, Oct. 1968, NASA.
2. Spreeman, K. P., "Induced Interference Effects on Jet and Buried-Fan VTOL Configurations in Transition," TN D-731, Mar. 1961, NASA.
3. Otis, J. H., "Induced Interference Effects on a Four-Jet VTOL Configuration with Various Wing Planforms in the Transition Speed Range," TN D-1400, Sept. 1962, NASA.
4. Vogler, R. D., "Interference Effects of Single and Multiple Round or Slotted Jets on a VTOL in Transition," TN D-2380, Aug. 1964, NASA.
5. Hickey, D. H. and Ellis, D. R., "Wind Tunnel Tests of a Semispan Wing with a Fan Rotating in the Plane of the Wing," TN D-88, Oct. 1959, NASA.
6. Gentry, G. L., and Margason, R. J., "Jet-Induced Lift Losses on VTOL Configurations Hovering In and Out of Ground Effects," TN D-3166, Feb. 1966, NASA.
7. Hickey, D. and Hall, L. "Aerodynamic Characteristics of a Large-Scale Model with Two High Disc-Loading Fans Mounted in the Wing," TN D-1650, Feb. 1963, NASA.
8. Kirk, J. V., Hickey, D. H., and Hall, L. P., "Aerodynamic Characteristics of a Full-Scale Fan-in-Wing Model Including Results in Ground Effect with Nose-Fan Pitch Control," TN D-2368, July 1964, NASA.
9. Margason, R. J., "Jet-Induced Effects in Transition Flight," SP-116, April 1966, NASA.
10. Hammond, A. D., "Thrust Losses in Hovering for Jet VTOL Aircraft," SP-116, April 1966, NASA.
11. Trebble, W. J. G. and Williams, J., "Exploratory Wind-Tunnel Investigations on a Bluff Body Containing a Lifting Fan," C. P. No. 597, Apr. 1961, British Royal Aircraft Establishment.

12. Callaghan, E. E. and Ruggeri, R. S., "Investigation of the Penetration of an Air Jet Directed Perpendicularly to an Air Stream," TN 1615, June 1948, NACA.
13. Callaghan, E. E. and Bowden, D. T., "Investigation of Flow Coefficients of Circular, Square and Elliptical Orifices at High Pressure Ratios," TN 1947, Sept. 1949, NACA.
14. Ruggeri, R., Callaghan, E., and Bowden, D., "Penetration of Air Jets Issuing from Circular, Square, and Elliptical Orifices Directed Perpendicularly to an Air Stream," TN 2019, Feb. 1950, NACA.
15. Gordier, R., "Studies of Fluid Jets Discharging Normally into Moving Liquid," Technical Paper No. 28, Series B. 1959, St. Anthony Falls Hydro Lab, University of Minnesota.
16. Jordinson, R., "Flow in a Jet Directed Normal to the Wind," R & M 3074, October 1956, British Aero. Res. Council.
17. Keffer, J. F. and Baines, W. D., "The Round Turbulent Jet in a Cross Wind," Journal of Fluid Mechanics, Vol. 15, Part 4, 1963, pp. 481-496.
18. Pratte, B. D. and Baines, W. D., "Profiles of the Round Turbulent Jet in a Cross Flow," Journal of the Hydraulics Division, Proceedings of the ASCE, Vol. 92, No. HY6, Nov. 1967, pp. 53-64.
19. Platten, J. L. and Keffer, J. F., "Entrainment in Deflected Axisymmetric Jets at Various Angles to the Stream," UTME-TP 6808, June 1968, University of Toronto.
20. Hardy, W. G., "Non-Parallel Flow Interactions," M.A.E. Thesis, University of Virginia, 1967.
21. Vogler, R. D., "Surface Pressure Distribution Induced on a Flat Plate by a Cold Air Jet Issuing Perpendicularly from the Plate and Normal to a Low Speed Free Stream Flow," TN D-1629, March 1963, NASA.
22. Bradbury, L. J. S. and Wood, M. N., "The Static Pressure Distribution Around a Circular Jet Exhausting Normally from a Plane Wall into an Airstream," Tech. Note No. Aero 2978, Aug. 1964, British Royal Aircraft Establishment.
23. Gelb, G. H. and Martin, W. A., "An Experimental Investigation of the Flow Field about a Subsonic Jet Exhausting into a Quiescent and a Low Velocity Air Stream," Canadian Aeronautics and Space Journal, Vol. 12, No. 8, October 1966, pp. 333-342.

24. Wooler, P. T., Burghart, G. H. and Gallagher, J. T. "The Pressure Distribution on a Rectangular Wing with a Jet Exhausting Normally into an Airstream," Journal of Aircraft, Vol. 4, No. 6, Nov.-Dec. 1967, pp. 537-543.
25. Peake, D. J., "The Pressures on a Surface Surrounding a Jet Issuing Normal to a Mainstream," Aeronautical Report LR-410, Nov. 1964, National Research Council of Canada, Ottawa, Can.
26. Williams, J. and Wood, M. N., "Aerodynamic Interference Effects with Jet-Lift V/STOL Aircraft under Static and Forward-Speed Conditions," Zeitschrift fur Flugwissenschaften, Vol. 15, No. 7, July 1967, pp. 237-256.
27. Lee, C. C. "A Review of Research on the Interaction of a Jet with an External Stream," Technical Note R-184, Mar. 1966, Brown Engineering Company, Inc.
28. Margason, R. J., "Review of Propulsion. Induced Effects on Aerodynamics of Jet/STOL Aircraft," TN D-5617, Feb. 1970, NASA.
29. Abramovich, G. N., The Theory of Turbulent Jets, M.I.T. Press, Massachusetts Institute of Technology, Cambridge, Mass., 1963.
30. Margason, R. J., "The Path of a Jet Directed at Large Angles to a Subsonic Free Stream," TN D-4919, Nov. 1968, NASA.
31. Margason, R. J. and Fearn, R., "Jet Wake Characteristics and Their Induced Aerodynamic Effects on V/STOL Aircraft in Transition Flight," SP-218, Sept. 1969, NASA.
32. Wu, J. C., McMahon, H. M., Mosher, D. K., and Wright, M. A., "Experimental and Analytical Investigations of Jets Exhausting into a Deflecting Stream," Journal of Aircraft, Vol. 7, No. 1, Jan-Feb. 1970.
33. Monical, R. E., "A Method of Representing Fan-Wing Combinations for Three-Dimensional Potential Flow Solutions," Journal of Aircraft, Vol. 2, No. 6, Nov. 1965, pp. 527-530.
34. Wooler, P. T., "On the Flow Past a Circular Jet Exhausting at Right Angles from a Flat Plate or a Wing," Journal of the Royal Aeronautical Society, Vol. 71, March 1967, pp. 216-218.
35. Crowe, C. T. and Riesebieter, H., "An Analytical and Experimental Study of Jet Deflection in a Cross-Flow," Fluid Dynamics of Rotor and Fan Supported Aircraft at Subsonic Speeds, Paris: Advisory Group for Aerospace Research and Development Preprint, 1967.

36. McAllister, J. D., "A Momentum Theory for the Effects of Cross Flow on Incompressible Turbulent Jets," Ph.D. Thesis, August 1968, University of Tennessee.
37. Wu, J. C. and Wright, M. A., "A Blockage-Sink Representation of Jet Interference Effects for Noncircular Jet Orifices," Analysis of a Jet in a Subsonic Crosswind, SP-218, Sept. 1969, NASA.
38. Cusisk, C. F., "Flow Meter Engineering Handbook," Minneapolis-Honeywell Regulator Co., Brown Instrument Division, Philadelphia, Pa., 1961.
39. Utterback, N. G. and Griffith, T., Jr., "Reliable Submicron Pressure Readings with a Capacitance Manometer," Review of Scientific Instruments, Vol. 37, No. 7, July 1966.
40. Rainbird, W. J., "Errors in Measurement of Mean Static Pressure of a Moving Fluid due to Pressure Holes," DME/NAE Quarterly Bulletin No. 1967(3), Oct. 1967, National Aeronautical Establishment, Ottawa.
41. Hinze, J. O., Turbulence, McGraw-Hill, New York, 1959.
42. Pope, A. and Harper, J. J., Low-Speed Wind Tunnel Testing, John Wiley and Sons, Inc., New York, New York, 1966.
43. Trentacoste, N. and Sforza, P., "Further Experimental Results for Three-Dimensional Free Jets," AIAA Journal, Vol. 5, No. 5, May 1967.
44. Wright, M. A., "A Two-Dimensional Representation of the Crosswind for the Jet Interference Problem," Ph.D. Thesis, June 1970, Georgia Institute of Technology.
45. McMahon, H. M. and Mosher, D. K., "Experimental Investigation of Pressures Induced on a Flat Plate by a Jet Issuing into a Subsonic Crosswind," Analysis of a Jet in a Subsonic Crosswind, SP-218, Sept. 1969, NASA.
46. "Flows with Large Velocity Fluctuations," Film No. 575, O.N.E.R.A.
47. Smith, R. H. and Wang, C. T., "Contracting Cones Giving Uniform Throat Speed," Journal of Aeronautical Sciences, Vol. 11, No. 4, Oct. 1944.

**TABLES**

Table 1. Surface Pressure Test Conditions and Result Index

$w/l$	$\lambda$	$q_{\infty}$ (mm Hg)	Results (Figure No.)	Comments
Data taken in the range $0 \leq \beta \leq 180^\circ$ , $r_1/a \leq r/a \leq$ 15.75, unless otherwise noted.				
0.3	4	1.07	47a	
↓	8	↓	47b	
	10		47c	
	12		47d	
	Solid		37	Right cylinder, wooden
1.0	0	1.07		
↓	3	↓	26	Data taken at $\beta = 180^\circ$ only
	4		47e	
	6.8		40	
	8		47f	
	10		47g	
	12		47h	
	Solid #1		25	Hose approximating path at $\lambda \approx 4$
	Solid #2		25	Hose approximating path at $\lambda \approx 8$
3.4	4		47i	
↓	7.5	↓	26	Data taken at $\beta = 180^\circ$ only
	9		26	Data taken at $\beta = 180^\circ$ only



Table 1. Surface Pressure Test Conditions and Result Index (Continued)

$w/l$	$\lambda$	$q_{\infty}$ (mm Hg)	Results (Figure No.)	Comments
3.4	8	1.07	47j	
↓	10	↓	47k	
	12		47l	
	20		47m	
	Solid	1.07	37	Right cylinder, wooden

Table 2. Pressure Probe Test Conditions and Result Index

Region Surveyed				Results		Comments
$w/l$	$\lambda$	$q_\infty$	$x/a$	$y/a$	$z/a$	Figure Table No.
0.3	4	1.07	0 to 10	0	as needed	31
	8					
	12					
	4		-4	0	6 to 22	46
	12					
	4		-3 to 3	4	6 to 14	36 & 44
	8					
	12					
	4		-5 to 5	10		
	12					
1.0	4	1.07	0 to 10	0	as needed	31
	6.8					
	8					

Determination of jet path

Upstream survey

Lateral flow field survey

Determination of jet path

Table 2. Pressure Probe Test Conditions and Result Index (Continued)

$w/l$	Region Surveyed					Results	
	$\lambda$	$q_\infty$	$x/a$	$y/a$	$z/a$	Figure Table No.	Comments
1.0	12	1.07	0 to 10	0	as needed	31	Determination of jet path
	Solid #1		-1	0	5 to 24	45	Upstream survey: hose for $\lambda \approx 4$
	Solid #2		↓	↓	↓	↓	hose for $\lambda \approx 8$
	4		-3 to 3	4	6 to 14	44 & 36	Lateral flow field survey
	8		↓	↓	↓	↓	
	12		↓	↓	↓	↓	
	4		-5 to 5	10	↓	↓	
	8		↓	↓	↓	↓	
	12		↓	↓	↓	↓	
1.0	8	1.07	0 to 16	0 to 10	6 to 30	43	Extensive flow field survey
3.4	4	1.07	0 to 10	0	as needed	31	Determination of jet path
	8		↓	↓	↓	↓	
	12		↓	↓	↓	↓	



Table 3. Flow Visualization Test Conditions and Result Index

Medium	w/l	$\lambda$	$q_{\infty}$ (mm Hg)	Results (Figure No.)	Comments
Oil	0.3	4	1.07	29a	9' wind tunnel
		8		29b	
		12		29c	
		Solid		29d	Right cylinder
	1.0	4		29e	
		8		29f	
		12		29g	
		Solid		29h	Right cylinder
	3.4	4		29i	
		8		29j	
		12		29k	
		Solid		29l	
Tufts	0.3	4			
		8			
		12			
	1.0	4			
		8		30	
		12			
	3.4	4			
		8			
		12			

Table 3. Flow Visualization Test Conditions and Result Index (Continued)

Medium	w/l	$\lambda$	$q_{\infty}$ (mm Hg)	Results (Figure No.)	Comments
Smoke	0.08	*	*	33/34	2"x24" wind tunnel
↓	0.3	↓	↓	↓	↓
	1.0	↓	↓	↓	↓
	3.4	↓	↓	↓	↓
↓	12.5	↓	↓	↓	↓

\* Not measured explicitly; see Chapter III for procedure. Range was approximately  $4 \leq \lambda \leq 8$ .

Table 4. Extensive Flow Field Survey for  $w/l = 1.0$ ,  $\lambda = 8$ 

$x/a$	$y/a$	$z/a$	$q/q_\infty$	$q_x/q_\infty$	$q_y/q_\infty$	$q_z/q_\infty$	$P_o/P_{o_\infty}$
6	1	6	0.75	0.73	0.05	0.58	0.85
		10	0.76	0.68	0.16	2.21	0.96
		12	2.25	1.61	0.40	2.40	1.04
		14	4.78	3.26	0.63	1.97	0.87
		16	3.60	2.36	0.32	2.71	2.44
		18	2.25	1.07	0.16	3.43	4.17
		20	2.65	0.95	-0.63	1.52	2.04
		22	2.56	0.67	-1.11	0.28	0.91
		24	0.95	0.67	-0.34	0.16	0.98

Sign Convention		
Component	Sign	Direction of Component
x	+	Downstream
	-	Upstream
y	+	Away from jet path
	-	Toward jet path
z	+	Up (away from plate surface)
	-	Down

Table 4. Extensive Flow Field Survey for  $w/l = 1.0$ ,  $\lambda = 8$  (Continued)

$x/a$	$y/a$	$z/a$	$q/q_\infty$	$q_x/q_\infty$	$q_y/q_\infty$	$q_z/q_\infty$	$P_o/P_{o_\infty}$
10	1	6	0.85	0.80	-0.12	0.28	0.80
		8	0.93	0.80	-0.19	0.44	0.87
		10	1.14	0.80	-0.36	0.73	0.97
		12	1.72	0.85	-0.55	1.40	0.95
		14	2.06	0.89	-0.39	1.81	0.87
		16	2.16	1.08	-0.03	1.87	0.91
		18	1.89	1.23	0.25	1.41	1.00
		20	2.61	2.09	0.28	1.55	2.09
		22	2.84	2.33	0.31	1.60	2.48
		24	1.38	1.21	0.19	0.64	1.30
		26	0.86	0.82	0.11	0.23	0.97
		28	0.85	0.84	0.00	0.13	1.00
16	1	6	0.84	0.83	-0.06	0.15	0.77
		8	0.90	0.86	-0.08	0.24	0.83
		10	0.93	0.86	-0.10	0.33	0.87
		12	1.05	0.89	-0.18	0.52	0.96
		14	1.37	0.96	-0.35	0.90	0.94
		16	1.62	0.96	-0.35	1.25	0.96
		18	1.54	0.95	-0.16	1.21	0.83
		20	1.40	0.96	0.16	1.00	0.78
		22	1.40	1.16	0.20	0.76	0.91
		24	1.94	1.74	0.18	0.83	1.61



Table 4. Extensive Flow Field Survey for  $w/l = 1.0$ ,  $\lambda = 8$  (Continued)

$x/a$	$y/a$	$z/a$	$q/q_\infty$	$q_x/q_\infty$	$q_y/q_\infty$	$q_z/q_\infty$	$P_o/P_{o_\infty}$
16	1	26	1.96	1.78	0.17	0.81	1.65
		28	1.24	1.17	0.08	0.41	1.15
		30	0.95	0.92	0.04	0.21	1.00
6	2	6	1.13	0.86	-0.57	0.46	0.97
		10	3.51	2.35	-1.51	2.12	1.30
		12	4.07	2.79	-0.23	2.95	2.26
		14	3.60	2.47	0.59	2.55	2.26
		16	4.28	3.03	0.88	2.90	3.39
		18	3.86	2.67	1.09	2.56	3.39
		20	1.59	1.19	0.56	0.88	1.44
		22	0.75	0.69	0.21	0.20	0.94
		24	0.81	0.79	0.10	0.14	1.00
8	2	6	0.98	-0.88	-0.28	0.33	0.96
		8	1.16	0.89	-0.54	0.52	0.99
		10	1.71	1.07	-0.97	0.92	0.87
		12	3.07	2.05	-0.87	2.11	1.04
		14	3.42	2.38	0.0	2.46	1.57
		16	2.96	2.13	0.56	1.98	1.65
		18	3.40	2.59	0.67	2.10	3.04
		20	3.27	2.50	0.78	1.96	2.78
		22	1.51	1.23	0.47	0.74	1.30
		24	0.85	0.79	0.18	0.24	0.96

Table 4. Extensive Flow Field Survey for  $w/l = 1.0$ ,  $\lambda = 8$  (Continued)

$x/a$	$y/a$	$z/a$	$q/q_\infty$	$q_x/q_\infty$	$q_y/q_\infty$	$q_z/q_\infty$	$P_o/P_{o_\infty}$
8	2	26	0.84	0.82	0.10	0.16	1.00
		28	0.87	0.86	0.05	0.12	1.00
10	2	6	0.94	0.89	-0.19	0.25	0.93
		8	0.99	0.88	-0.29	0.36	0.97
		10	1.23	0.88	-0.62	0.59	0.96
		12	2.02	1.30	-0.87	1.28	0.87
		14	2.56	1.77	-0.54	1.77	0.96
		16	2.43	1.78	0.17	1.65	1.30
		18	2.04	1.58	0.47	1.20	1.48
		20	2.87	2.32	0.56	1.58	2.35
		22	2.59	2.13	0.53	1.37	2.13
		24	1.24	1.11	0.28	0.49	1.16
		26	0.87	0.84	0.13	0.19	0.97
		28	0.88	0.87	0.07	0.15	1.00
		30	0.89	0.89	0.00	0.11	1.00
13	2	6	0.91	0.88	-0.13	0.18	0.90
		9	0.95	0.87	-0.20	0.31	0.96
		12	1.28	0.97	-0.56	0.63	1.02
		15	1.81	1.26	-0.55	1.17	0.70
		18	1.80	1.38	0.30	1.13	0.96
		21	1.96	1.64	0.41	0.99	1.57
		24	2.29	1.99	0.41	1.06	1.87

Table 4. Extensive Flow Field Survey for  $w/l = 1.0$ ,  $\lambda = 8$  (Continued)

$x/a$	$y/a$	$z/a$	$q/q_\infty$	$q_x/q_\infty$	$q_y/q_\infty$	$q_z/q_\infty$	$P_o/P_{o_\infty}$
13	2	27	1.05	0.99	0.18	0.32	1.02
		30	0.90	0.89	0.05	0.14	1.00
16	2	6	0.91	0.89	-0.10	0.14	0.87
		8	0.92	0.89	-0.12	0.21	0.91
		10	0.96	0.91	-0.18	0.31	0.97
		12	1.07	0.92	-0.30	0.45	1.00
		14	1.43	1.08	-0.52	0.78	0.98
		16	1.74	1.24	-0.51	1.12	0.85
		18	1.76	1.37	-0.09	1.11	0.87
		20	1.70	1.32	0.33	1.02	0.91
		22	1.60	1.35	0.35	0.78	1.13
		24	2.03	1.82	0.33	0.83	1.65
		26	1.85	1.68	0.28	0.73	1.57
		28	1.23	1.16	0.17	0.38	1.13
		30	0.95	0.92	0.09	0.19	0.99
6	3	6	1.25	1.05	-0.64	0.25	0.98
		8	1.97	1.53	-1.18	0.37	0.97
		10	3.78	3.36	-1.10	1.35	1.48
		12	4.87	4.13	0.50	2.53	2.78
		14	4.63	3.65	0.97	2.69	3.26
		16	4.35	3.22	1.51	2.50	3.35
		18	2.93	2.13	1.23	1.58	2.44

Table 4. Extensive Flow Field Survey for  $w/\ell = 1.0$ ,  $\lambda = 8$  (Continued)

$x/a$	$y/a$	$z/a$	$q/q_\infty$	$q_x/q_\infty$	$q_y/q_\infty$	$q_z/q_\infty$	$P_o/P_{o_\infty}$
6	3	20	1.24	1.01	0.58	0.44	1.07
		22	0.77	0.72	0.24	0.14	0.94
		24	0.83	0.81	0.12	0.11	1.00
10	3	6	0.98	0.94	-0.22	0.20	0.98
		8	1.06	0.95	-0.37	0.28	1.00
		10	1.35	1.08	-0.71	0.38	1.00
		12	2.24	1.83	-1.06	0.75	0.96
		14	3.02	2.66	-0.39	1.38	1.44
		16	3.04	2.58	0.61	1.49	1.96
		18	2.90	2.40	0.84	1.39	2.00
		20	2.94	2.44	0.84	1.41	2.35
		22	2.02	1.69	0.71	0.86	1.74
		24	1.07	0.97	0.34	0.31	1.05
		27	0.88	0.87	0.12	0.13	1.00
		30	0.91	0.90	0.04	0.10	1.00
16	3	6	0.95	0.94	-0.13	0.12	0.95
		8	0.97	0.94	-0.16	0.17	0.89
		10	1.00	0.95	-0.22	0.23	1.00
		12	1.11	0.98	-0.40	0.33	1.02
		14	1.57	1.26	-0.71	0.60	1.00
		16	1.98	1.71	-0.55	0.82	0.92
		18	2.07	1.87	0.00	0.89	1.17

Table 4. Extensive Flow Field Survey for  $w/l = 1.0$ ,  $\lambda = 8$  (Continued)

$x/a$	$y/a$	$z/a$	$q/q_\infty$	$q_x/q_\infty$	$q_y/q_\infty$	$q_z/q_\infty$	$P_o/P_{o_\infty}$
16	3	20	1.75	1.54	0.46	0.71	1.17
		22	1.93	1.70	0.51	0.76	1.44
		24	2.13	1.92	0.48	0.79	1.70
		26	1.78	1.63	0.38	0.62	1.44
		28	1.17	1.11	0.21	0.31	1.09
		30	0.96	0.94	0.12	0.16	1.00
6	4	6	1.31	1.17	-0.57	0.17	0.98
		8	1.83	1.59	-0.90	0.05	0.99
		10	2.77	2.66	-0.79	0.11	1.09
		12	3.33	3.21	0.40	0.82	1.48
		14	3.52	3.03	1.23	1.29	2.00
		16	2.91	2.37	1.30	1.08	1.91
		18	1.76	1.42	0.93	0.49	1.22
		21	0.87	0.81	0.32	0.10	0.95
8	4	24	0.88	0.87	0.12	0.11	1.00
		6	1.13	1.05	-0.38	0.18	0.99
		8	1.33	1.17	-0.61	0.17	1.00
		10	2.03	1.78	-0.98	0.12	1.02
		12	2.79	2.68	-0.66	0.42	1.22
		14	3.42	3.20	0.58	1.06	1.91
		16	3.43	2.92	1.18	1.34	2.35
		18	2.85	2.38	1.09	1.12	2.00

Table 4. Extensive Flow Field Survey for  $w/l = 1.0$ ,  $\lambda = 8$  (Continued)

$x/a$	$y/a$	$z/a$	$q/q_\infty$	$q_x/q_\infty$	$q_y/q_\infty$	$q_z/q_\infty$	$P_o/P_{o_\infty}$
8	4	20	1.81	1.52	0.79	0.60	1.30
		22	0.99	0.88	0.40	0.18	0.97
		24	0.89	0.86	0.21	0.12	0.98
		26	0.90	0.89	0.11	0.10	1.00
10	4	7	1.06	1.00	-0.31	0.18	1.00
		9	1.22	1.09	-0.52	0.20	1.00
		12	1.99	1.82	-0.80	0.20	0.96
		15	2.97	2.86	0.00	0.83	1.65
		18	2.99	2.57	1.04	1.11	2.09
		21	2.15	1.82	0.87	0.74	1.70
		24	1.01	0.93	0.35	0.21	0.99
		27	0.91	0.89	0.13	0.12	1.00
13	4	30	0.92	0.92	0.07	0.10	1.00
		7	1.05	1.00	-0.28	0.15	1.00
		9	1.06	1.00	-0.31	0.19	1.00
		12	1.48	1.28	-0.71	0.23	1.00
		15	2.46	2.34	-0.50	0.54	1.17
		18	2.83	2.60	0.68	0.89	1.74
		21	2.50	2.21	0.82	0.85	1.96
		24	1.71	1.52	0.57	0.55	1.41
		27	1.01	0.97	0.23	0.18	1.00
		30	0.94	0.93	0.09	0.11	1.00

Table 4. Extensive Flow Field Survey for  $w/l = 1.0$ ,  $\lambda = 8$  (Continued)

$x/a$	$y/a$	$z/a$	$q/q_\infty$	$q_x/q_\infty$	$q_y/q_\infty$	$q_z/q_\infty$	$P_o/P_{o_\infty}$
16	4	7	0.98	0.96	-0.15	0.12	1.00
		9	0.99	0.96	-0.20	0.16	1.00
		12	1.20	1.08	-0.45	0.25	1.03
		15	1.77	1.60	-0.68	0.37	0.96
		18	2.52	2.42	0.17	0.68	1.30
		21	2.28	2.07	0.65	0.71	1.61
		24	2.06	1.88	0.55	0.64	1.65
		27	1.23	1.16	0.31	0.30	1.13
0	6	30	0.96	0.94	0.13	0.13	1.00
		6	1.48	1.48	-0.07	-0.08	0.99
		10	1.31	1.30	0.09	-0.13	1.00
		14	1.11	1.10	0.13	-0.08	1.00
		18	0.95	0.94	0.12	-0.01	1.00
		21	0.93	0.92	0.08	0.01	1.00
2	6	24	0.93	0.93	0.04	0.03	1.00
		6	1.44	1.43	-0.17	-0.11	1.00
		9	1.56	1.54	-0.04	-0.23	1.00
		12	1.40	1.37	0.16	-0.23	1.00
		16	1.07	1.05	0.21	-0.09	1.00
		20	0.95	0.94	0.14	-0.01	1.00
4	6	24	0.94	0.93	0.08	0.03	1.00
		6	1.43	1.39	-0.31	-0.04	1.00

Table 4. Extensive Flow Field Survey for  $w/l = 1.0$ ,  $\lambda = 8$  (Continued)

$x/a$	$y/a$	$z/a$	$q/q_\infty$	$q_x/q_\infty$	$q_y/q_\infty$	$q_z/q_\infty$	$P_o/P_{o_\infty}$
4	6	9	1.63	1.59	-0.20	-0.25	1.00
		12	1.65	1.60	0.13	-0.36	1.01
		16	1.22	1.17	0.29	-0.14	1.00
		20	0.98	0.96	0.19	-0.01	1.00
		24	0.93	0.92	0.10	0.03	1.01
6	6	5	1.21	1.16	-0.32	0.05	0.99
		8	1.45	1.39	-0.39	-0.10	1.00
		10	1.69	1.63	-0.33	-0.27	1.00
		12	1.79	1.74	-0.12	-0.39	1.04
		13.5	1.78	1.73	0.20	-0.37	1.04
		15	1.66	1.57	0.41	-0.30	1.03
		18	1.21	1.14	0.39	-0.13	1.00
		21	0.98	0.95	0.22	-0.01	1.00
		24	0.93	0.92	0.14	0.04	1.01
8	6	5	1.14	1.11	-0.28	0.06	0.99
		8	1.28	1.22	-0.39	0.00	1.00
		10	1.49	1.41	-0.44	-0.14	1.00
		12	1.76	1.70	-0.29	-0.33	1.05
		15	1.90	1.84	0.36	-0.30	1.00
		18	1.58	1.46	0.60	-0.10	1.04
		20	1.17	1.09	0.42	-0.06	1.00
		22	1.01	0.97	0.28	0.00	1.00



Table 4. Extensive Flow Field Survey for  $w/l = 1.0$ ,  $\lambda = 8$  (Continued)

$x/a$	$y/a$	$z/a$	$q/q_\infty$	$q_x/q_\infty$	$q_y/q_\infty$	$q_z/q_\infty$	$P_o/P_{o_\infty}$
8	6	26	0.94	0.93	0.12	0.05	1.00
10	6	5	1.08	1.05	-0.23	0.07	1.00
		8	1.16	1.11	-0.33	0.05	1.00
		10	1.35	1.28	-0.44	-0.04	1.00
		12	1.64	1.55	-0.47	-0.23	1.04
		14	1.96	1.92	-0.21	-0.32	1.08
		15	2.12	2.10	0.10	-0.28	1.17
		18	1.90	1.77	0.69	-0.03	1.22
		21	1.27	1.18	0.48	0.03	1.04
		24	1.00	0.97	0.24	0.04	1.00
		27	0.6	0.95	0.13	0.06	1.00
		30	0.96	0.95	0.07	0.05	1.00
13	6	5	1.04	1.02	-0.18	0.08	0.99
		8	1.08	1.05	-0.25	0.08	1.00
		10	1.16	1.11	-0.36	0.05	1.00
		12	1.36	1.28	-0.46	-0.05	1.02
		14	1.73	1.66	-0.43	-0.21	1.09
		16	2.03	2.02	-0.07	-0.19	1.24
		18	2.20	2.12	0.56	0.01	1.44
		20	2.03	1.89	0.74	0.14	1.44
		24	1.23	1.15	0.41	0.12	1.06
		27	0.99	0.97	0.19	0.07	1.00

Table 4. Extensive Flow Field Survey for  $w/l = 1.0$ ,  $\lambda = 8$  (Continued)

$x/a$	$y/a$	$z/a$	$q/q_\infty$	$q_x/q_\infty$	$q_y/q_\infty$	$q_z/q_\infty$	$P_o/P_{o_\infty}$
13	6	30	0.97	0.97	0.10	0.07	1.00
16	6	6	1.02	1.00	-0.17	0.06	1.00
		8	1.01	0.99	-0.19	0.07	1.00
		10	1.06	1.02	-0.28	0.08	1.00
		12	1.21	1.15	-0.39	0.02	1.00
		14	1.47	1.39	-0.48	-0.08	1.04
		16	1.78	1.74	-0.35	-0.17	1.13
		18	2.16	2.15	0.22	-0.05	1.39
		20	2.19	2.09	0.66	0.13	1.57
		22	2.02	1.88	0.69	0.26	1.52
		24	1.52	1.41	0.54	0.19	1.29
		26	1.18	1.12	0.37	0.13	1.07
		28	1.02	1.00	0.22	0.08	0.99
		30	0.99	0.98	0.13	0.08	1.00
0	8	5	1.33	1.33	-0.12	-0.04	1.00
		7	1.33	1.33	-0.08	-0.07	1.00
		9	1.26	1.26	-0.02	-0.09	1.00
		12	1.18	1.18	0.04	-0.10	1.00
		15	1.10	1.09	0.10	-0.07	1.00
		18	1.00	1.00	0.09	-0.04	1.00
		21	0.98	0.98	0.08	-0.01	1.00
		24	0.96	0.96	0.05	0.01	1.00

Table 4. Extensive Flow Field Survey for  $w/\lambda = 1.0$ ,  $\lambda = 8$  (Continued)

$x/a$	$y/a$	$z/a$	$q/q_\infty$	$q_x/q_\infty$	$q_y/q_\infty$	$q_z/q_\infty$	$P_o/P_{o_\infty}$
3	8	5	1.29	1.27	-0.19	-0.03	0.99
		7	1.31	1.29	-0.16	-0.09	0.99
		9	1.36	1.35	-0.10	-0.13	1.00
		12	1.31	1.30	0.00	-0.17	1.00
		15	1.20	1.19	0.12	-0.14	1.00
		18	1.06	1.05	0.14	-0.07	1.00
		21	1.00	0.99	0.11	-0.02	1.00
		24	0.97	0.97	0.07	0.01	1.00
6	8	5	1.21	1.19	-0.23	0.01	0.99
		7	1.23	1.21	-0.23	-0.04	0.99
		9	1.28	1.26	-0.20	-0.12	1.00
		12	1.39	1.37	-0.08	-0.22	1.00
		15	1.33	1.31	0.11	-0.23	1.00
		18	1.16	1.14	0.18	-0.12	1.00
		21	1.05	1.03	0.16	-0.05	1.00
		24	0.99	0.99	0.11	0.01	1.00
10	8	5	1.12	1.10	-0.21	0.04	1.00
		8	1.14	1.11	-0.25	0.00	0.99
		12	1.30	1.27	-0.23	-0.17	1.00
		16	1.42	1.39	0.06	-0.31	1.01
		20	1.20	1.17	0.25	-0.15	1.00
		25	1.00	0.99	0.14	0.00	1.00

Table 4. Extensive Flow Field Survey for  $w/l = 1.0$ ,  $\lambda = 8$  (Continued)

$x/a$	$y/a$	$z/a$	$q/q_\infty$	$q_x/q_\infty$	$q_y/q_\infty$	$q_z/q_\infty$	$P_o/P_{o_\infty}$
10	8	30	0.97	0.97	0.07	0.04	1.00
13	8	5	1.07	1.05	-0.19	0.04	0.99
		8	1.10	1.08	-0.22	0.02	1.00
		12	1.22	1.19	-0.27	-0.11	1.00
		16	1.44	1.41	-0.05	-0.32	1.04
		18	1.47	1.43	0.21	-0.29	1.07
		20	1.34	1.29	0.31	-0.19	1.04
		25	1.07	1.05	0.19	-0.01	1.00
		30	0.99	0.99	0.08	0.04	1.00
16	8	6	1.05	1.03	-0.18	0.04	1.00
		9	1.09	1.07	-0.22	0.03	1.00
		12	1.16	1.13	-0.27	-0.05	1.00
		15	1.34	1.30	-0.23	-0.23	1.04
		18	1.51	1.47	0.09	-0.30	1.13
		21	1.41	1.36	0.34	-0.14	1.13
		24	1.19	1.14	0.31	-0.04	1.03
		27	1.03	1.01	0.19	0.01	1.00
		30	1.02	1.01	0.10	0.04	1.00
3	10	5	1.25	1.24	-0.16	-0.01	0.99
		8	1.30	1.29	-0.13	-0.07	1.00
		12	1.24	1.23	-0.03	-0.10	1.00
		16	1.14	1.13	0.06	-0.09	1.00

Table 4. Extensive Flow Field Survey for  $w/\ell = 1.0$ ,  $\lambda = 8$  (Continued)

$x/a$	$y/a$	$z/a$	$q/q_\infty$	$q_x/q_\infty$	$q_y/q_\infty$	$q_z/q_\infty$	$P_o/P_{o_\infty}$
3	10	20	1.05	1.04	0.08	-0.04	1.00
		24	1.00	1.00	0.05	0.00	1.00
6	10	5	1.20	1.19	-0.20	0.01	0.99
		8	1.26	1.25	-0.19	-0.05	1.00
		12	1.30	1.29	-0.08	-0.12	1.00
		16	1.19	1.18	0.06	-0.13	1.00
		20	1.08	1.07	0.11	-0.07	1.00
		24	1.02	1.02	0.08	-0.02	1.01
10	10	5	1.14	1.12	-0.21	0.01	0.99
		8	1.17	1.15	-0.21	-0.02	1.00
		12	1.25	1.23	-0.19	-0.13	1.00
		16	1.27	1.26	-0.02	-0.20	1.00
		20	1.15	1.14	0.12	-0.13	1.00
		25	1.04	1.03	0.11	-0.03	1.00
		30	0.99	0.99	0.05	0.02	1.00
13	10	5	1.10	1.08	-0.20	0.02	0.99
		8	1.12	1.10	-0.21	-0.01	1.00
		12	1.18	1.16	-0.21	-0.10	1.00
		16	1.28	1.26	-0.08	-0.23	1.00
		20	1.21	1.19	0.12	-0.18	1.00
		25	1.07	1.06	0.12	-0.05	1.00
		30	0.99	0.99	0.07	0.01	1.00

Table 4. Extensive Flow Field Survey for  $w/l = 1.0$ ,  $\lambda = 8$  (Continued)

$x/a$	$y/a$	$z/a$	$q/q_\infty$	$q_x/q_\infty$	$q_y/q_\infty$	$q_z/q_\infty$	$P_o/P_{o_\infty}$
16	10	5	1.07	1.05	-0.19	0.00	0.99
		8	1.09	1.08	-0.19	0.00	1.00
		12	1.16	1.14	-0.20	-0.07	1.00
		16	1.25	1.23	-0.13	-0.23	1.02
		20	1.24	1.22	0.12	-0.23	1.03
		25	1.11	1.10	0.14	-0.06	1.00
		30	1.03	1.02	0.08	0.01	1.00

**ILLUSTRATIONS**

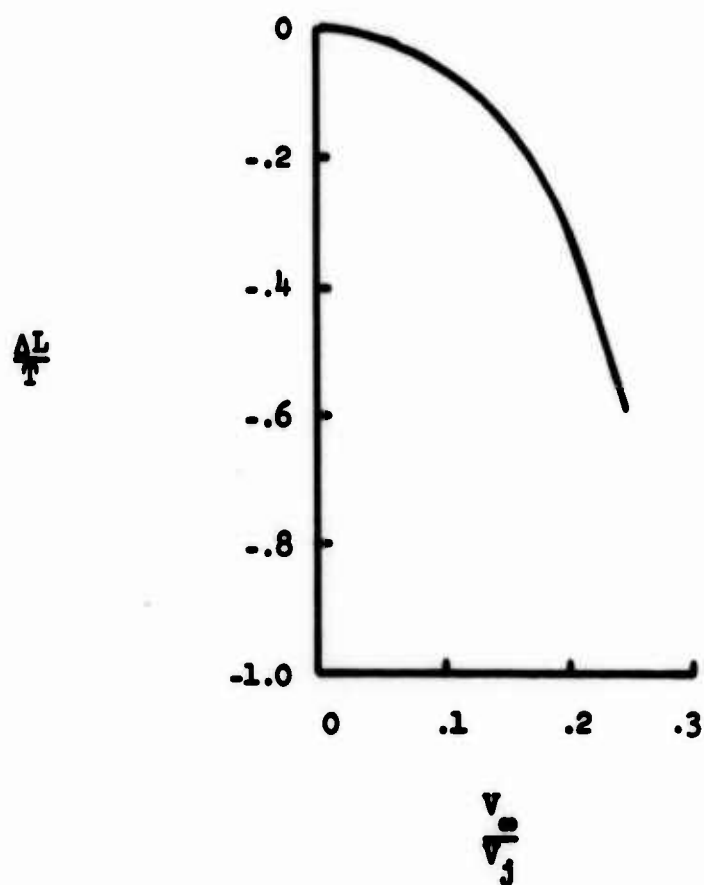


Figure 1. Lift Loss Due to Jet and Cross-Flow Interference (from Reference 4).



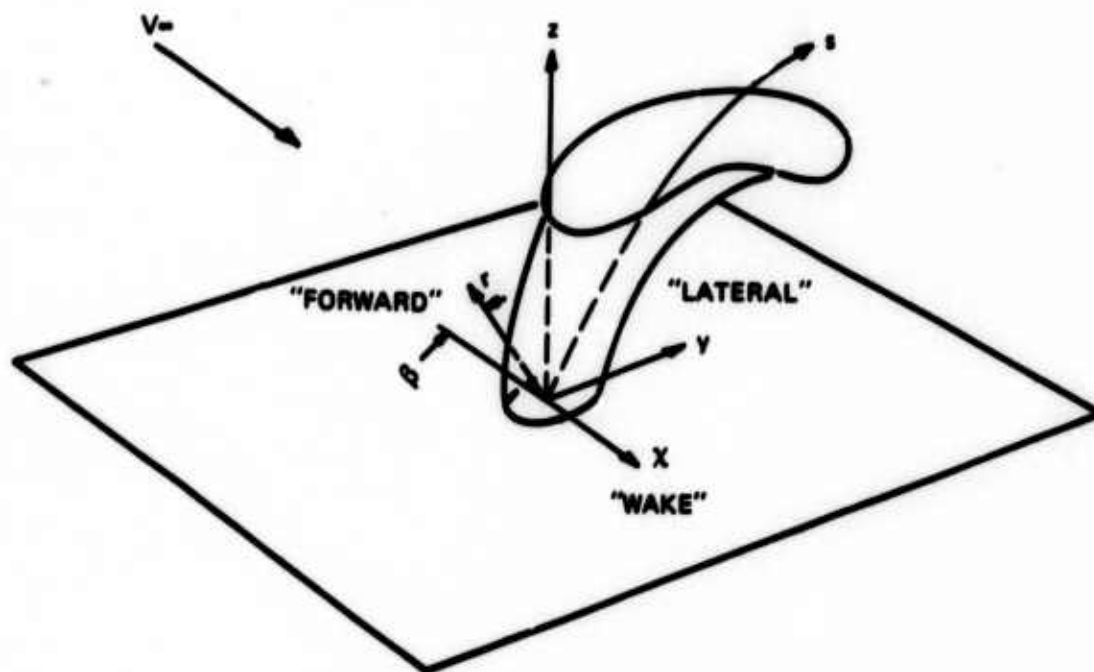
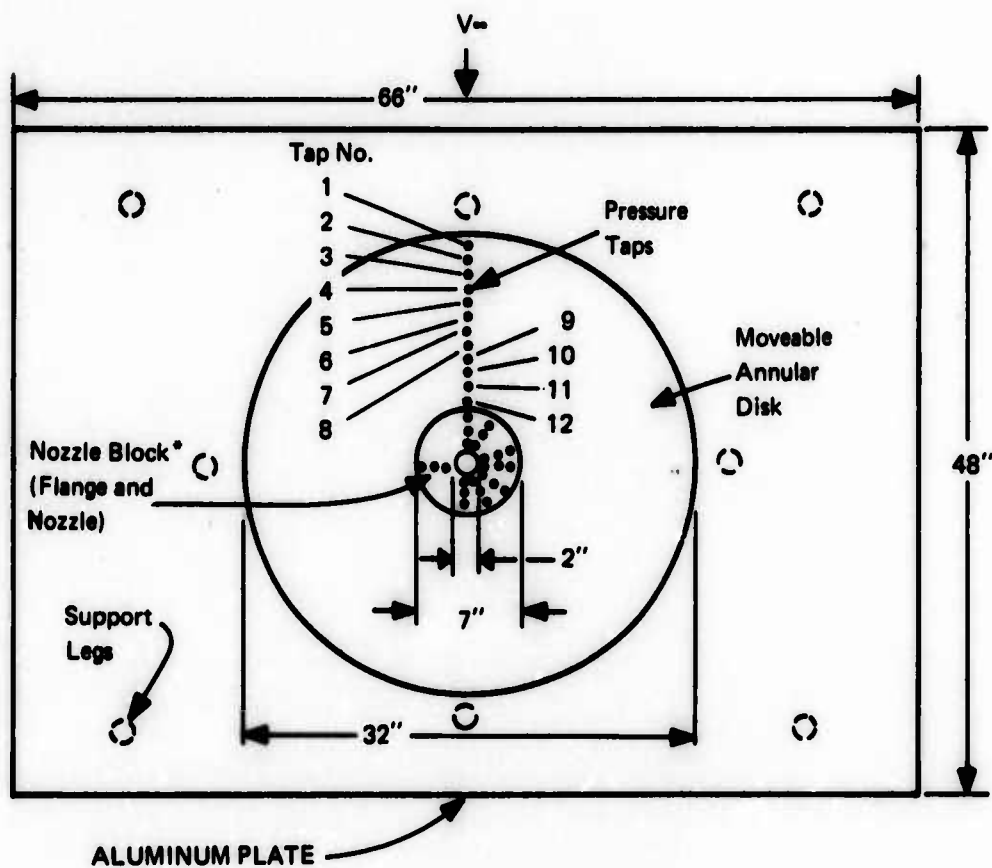


Figure 2. Coordinate System and Definition of Flow Region Terms.



\*See Figure 4  
for details

LOCATION OF PRESSURE TAPS ON ANNULAR DISK	
TAP NUMBER	r (inches)
1	15.75
2	13.75
3	13.00
4	12.00
5	11.00
6	10.00
7	9.00
8	8.00
9	7.00
10	6.00
11	5.00
12	4.25

Figure 3. Top View of Flat Plate.

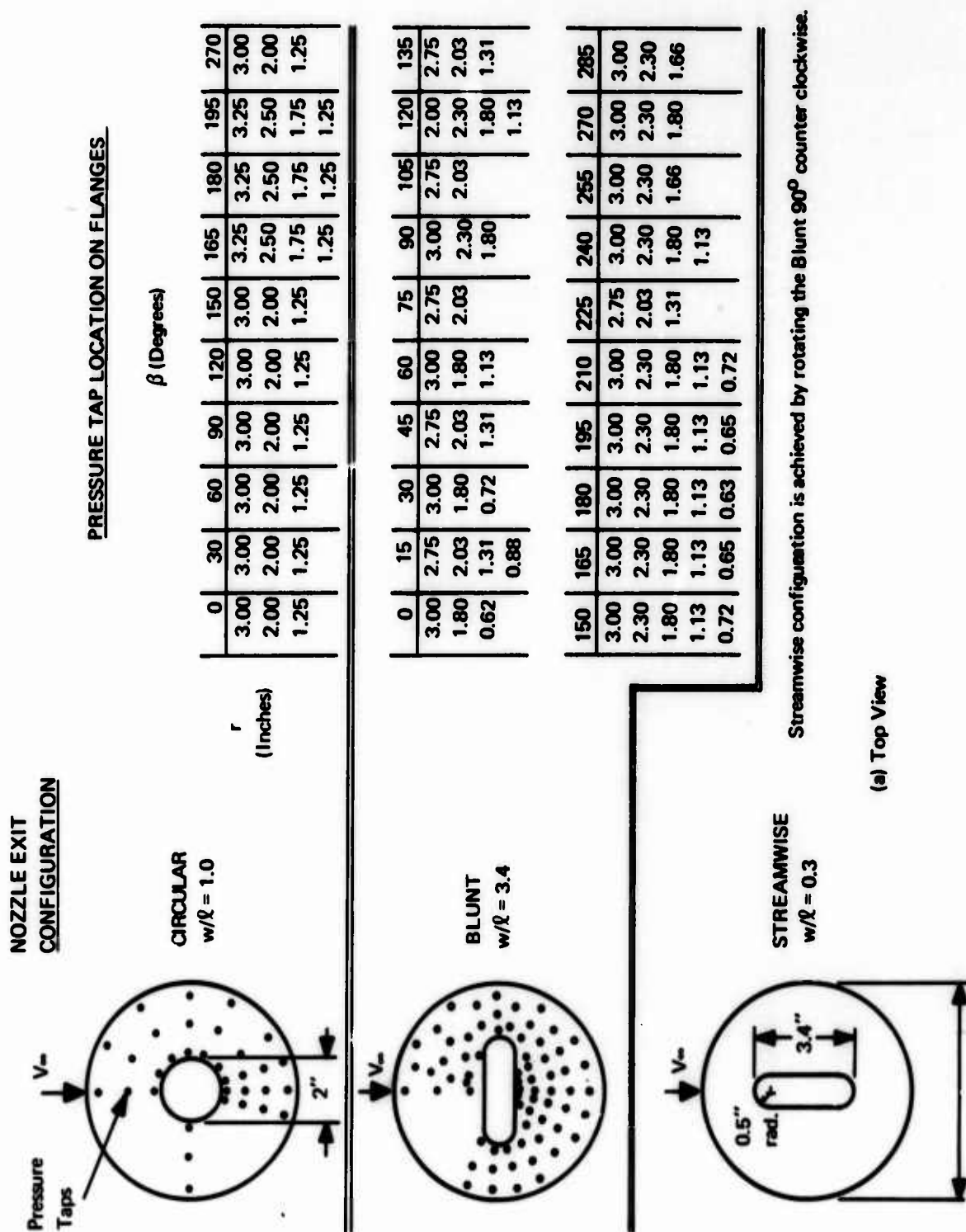
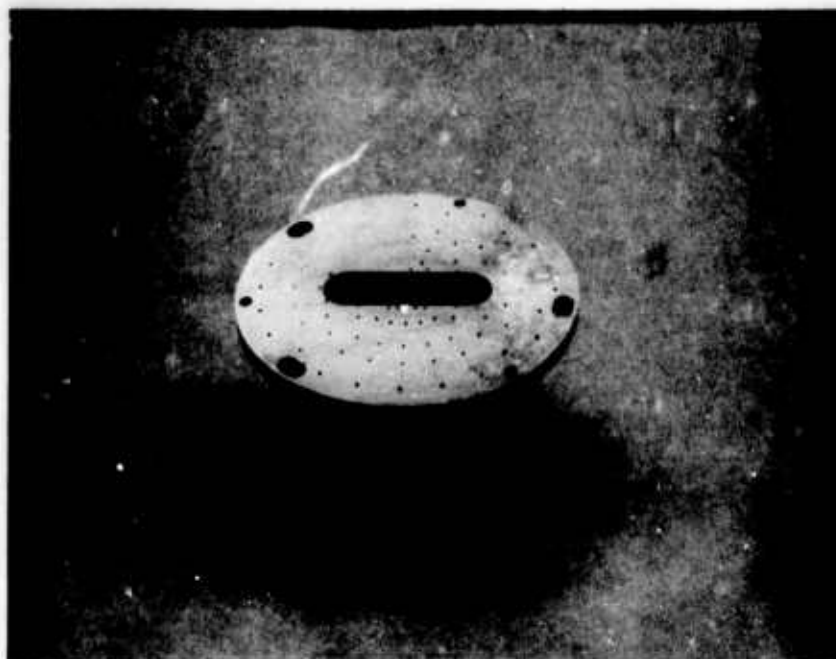


Figure 4. Nozzle Blocks: Exit Configurations and Flange Details.



(b) Oblique View.

Figure 4. Nozzle Blocks: Exit Configurations and Flange Details (Concluded).

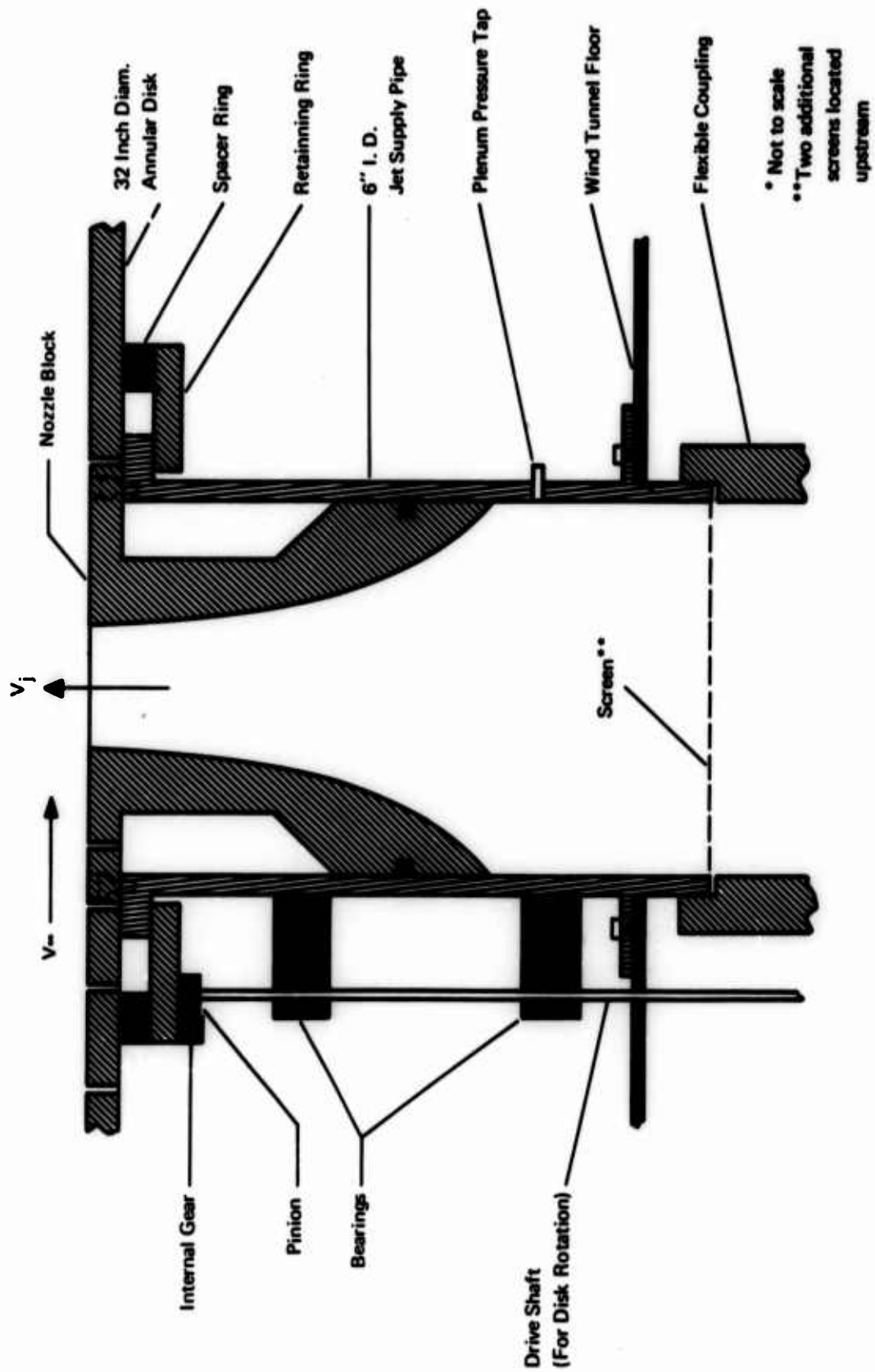


Figure 5. Side View of Nozzle Block in Jet Supply Pipe.\*



Figure 6. Plate Installed in the Wind Tunnel; Configuration for Acquiring Surface Pressures.

Speed: 3550 RPM

Inlet Conditions:

1. 14.7 psia
2. 68° F

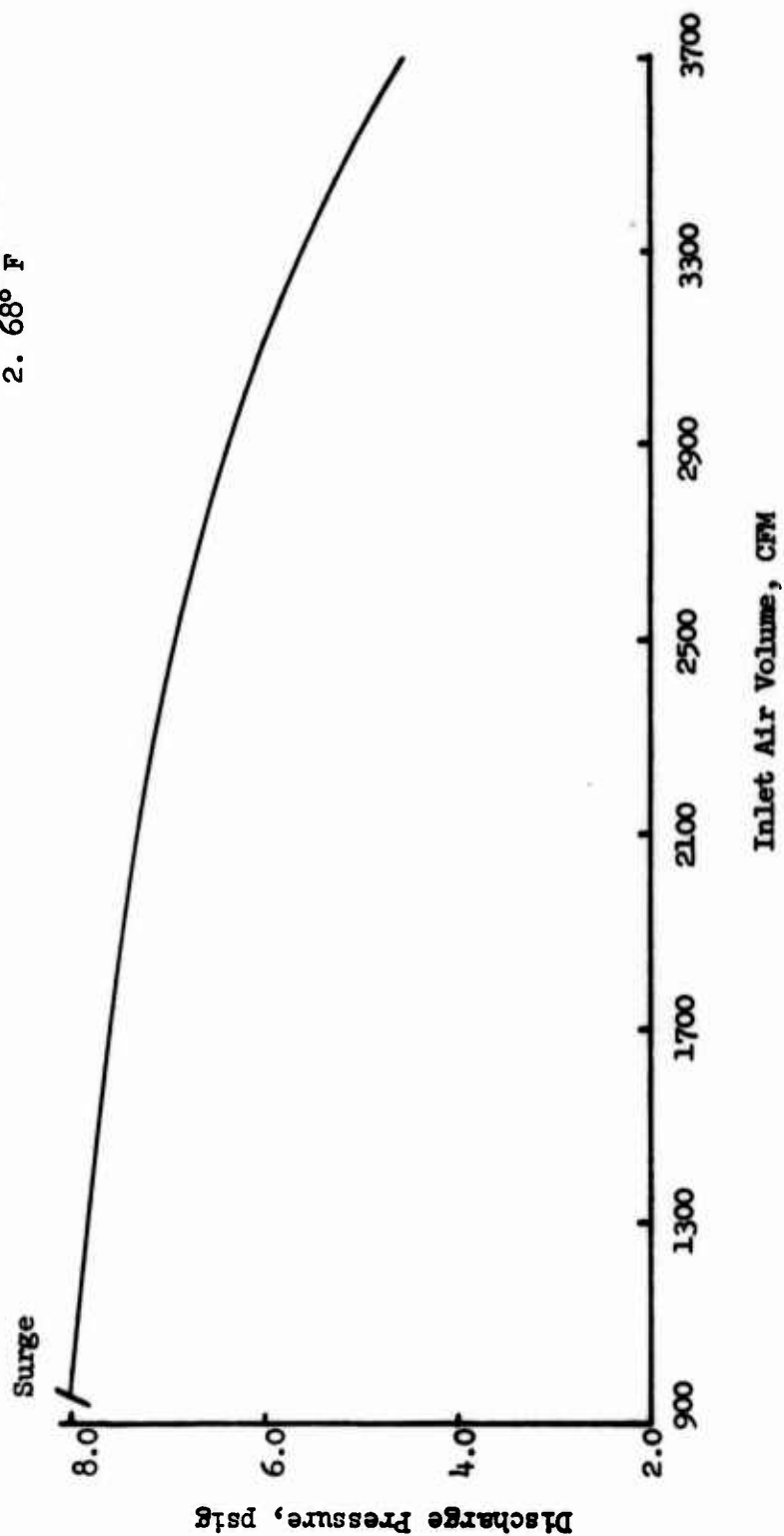


Figure 7. Blower Performance Curve.

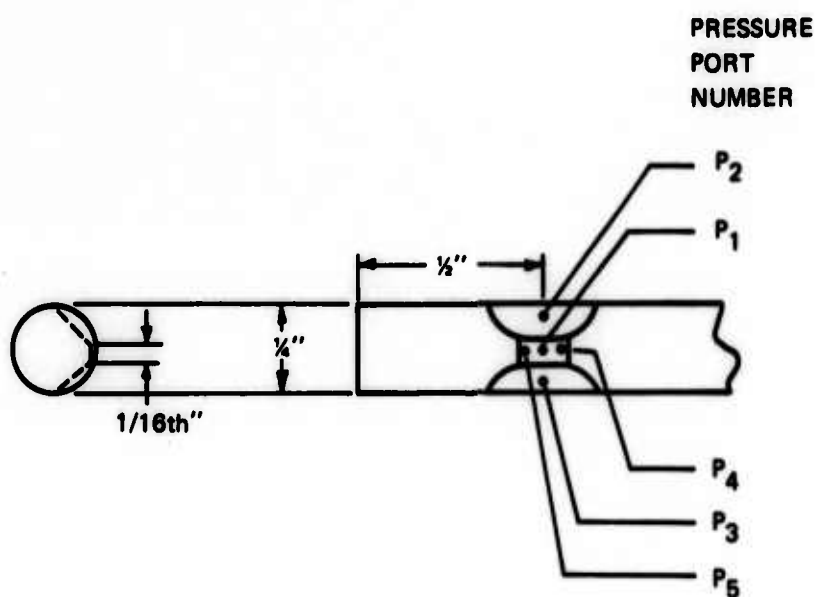
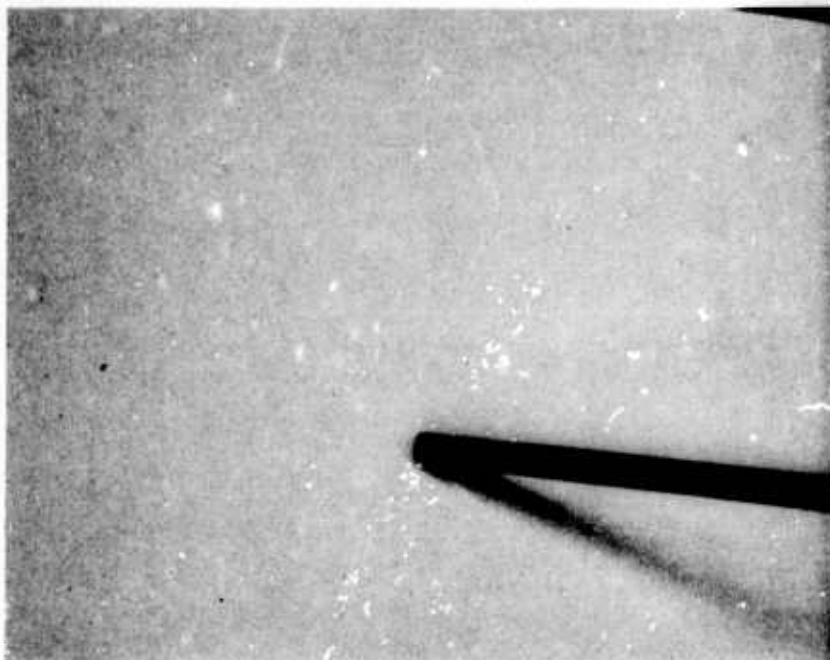


Figure 8. Pressure Probe.



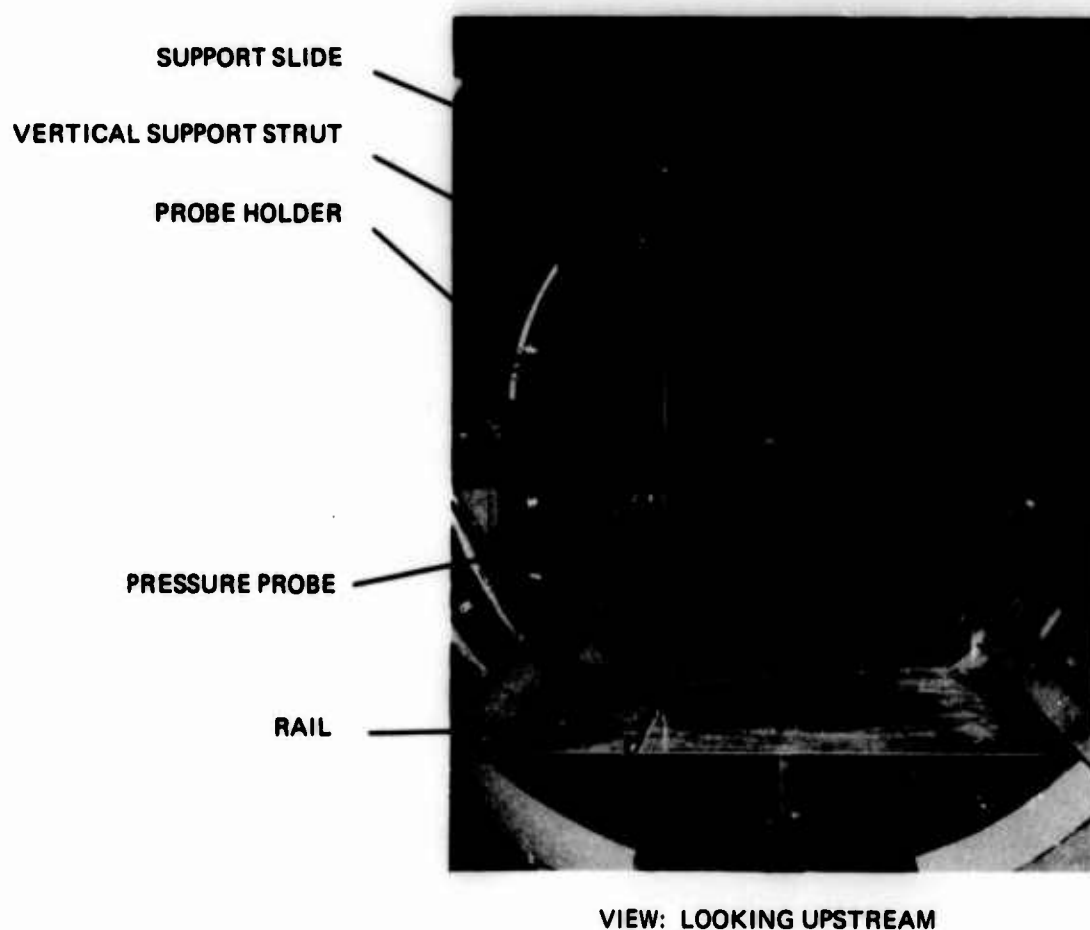


Figure 9. Pressure Probe and Traversing Mechanism Installation.



Figure 10. Total Pressure Rake.

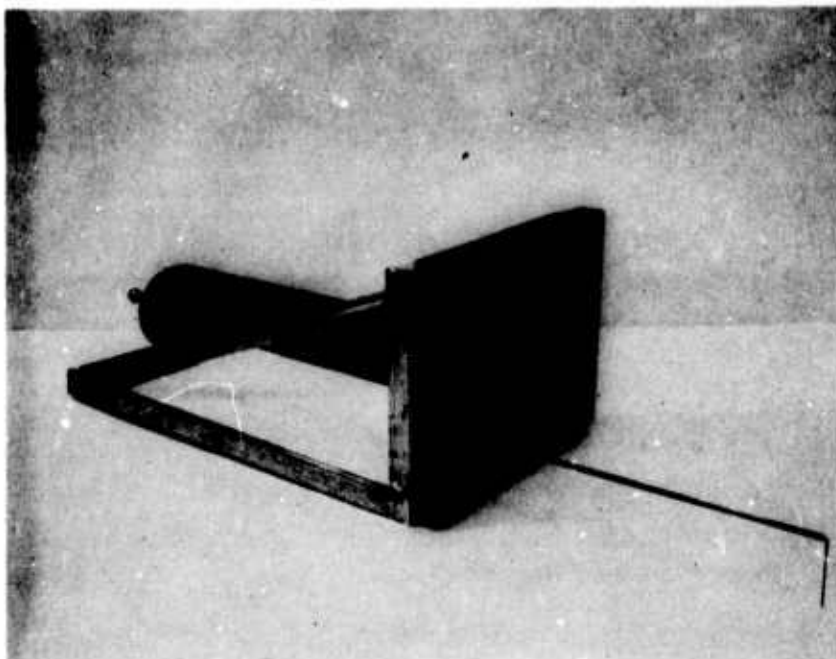
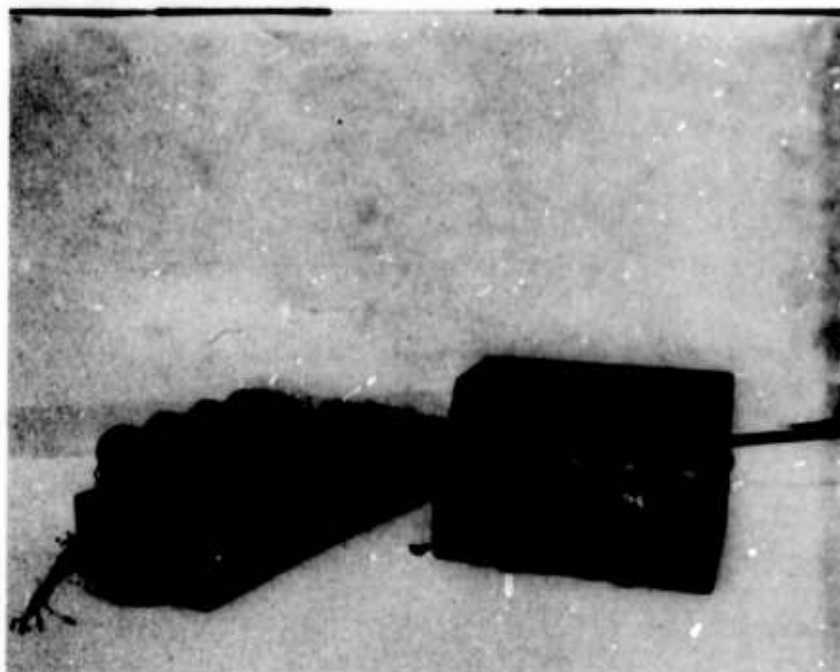
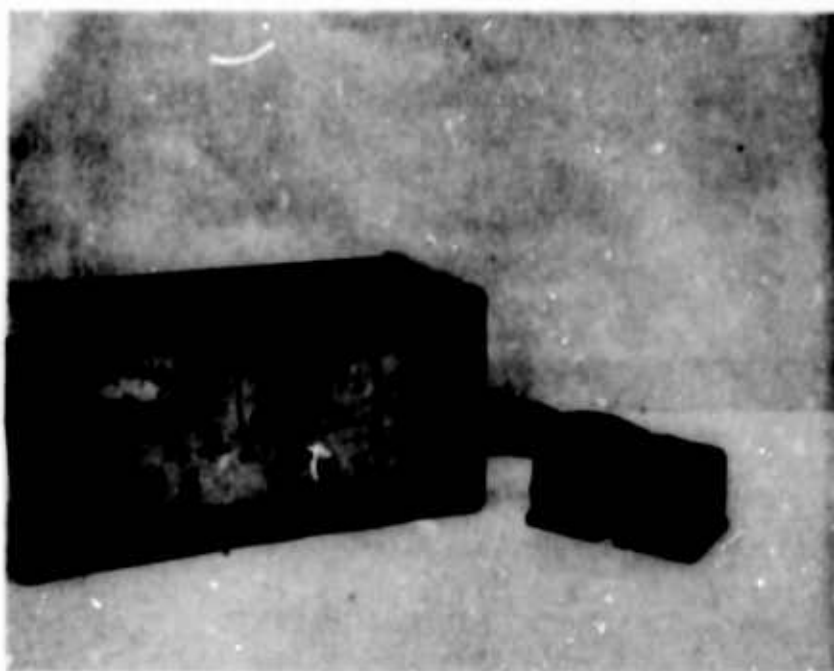


Figure 11. Total Pressure Probe and Stand.



**Figure 12. Fluid Wafer System.**



**Figure 13. Electronic Manometer System.**



Figure 14. Sacke Tunnel.

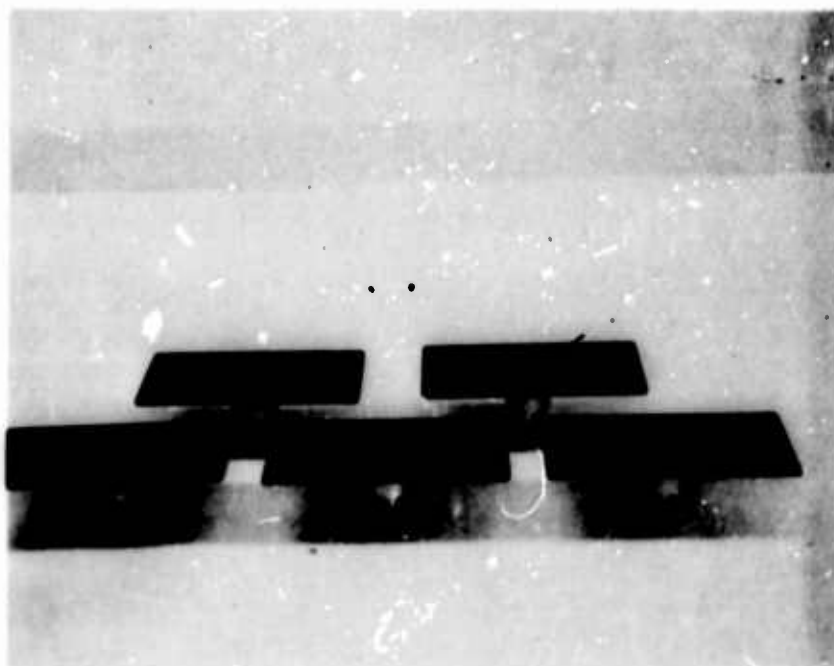


**Figure 15. Orifices and Plates Used in Smoke Studies.**

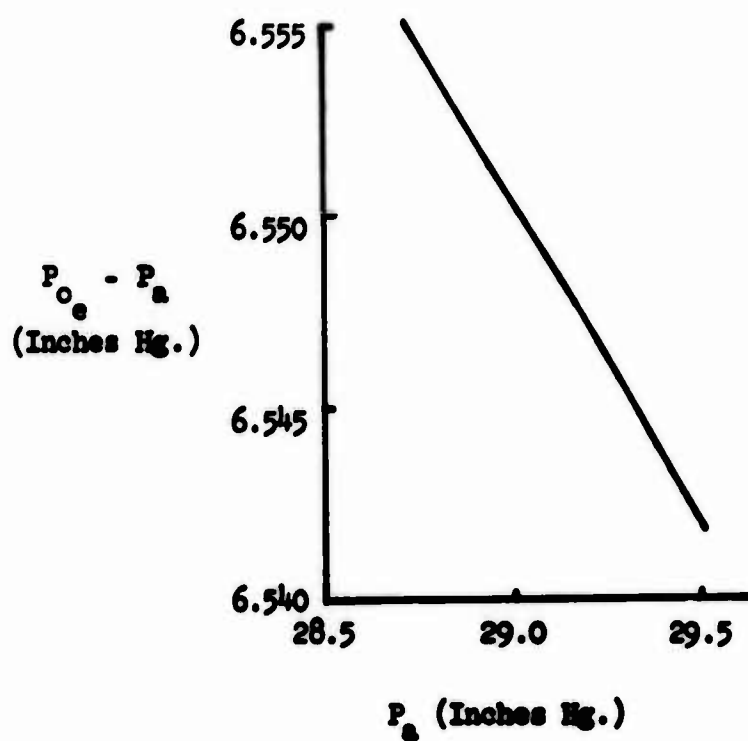
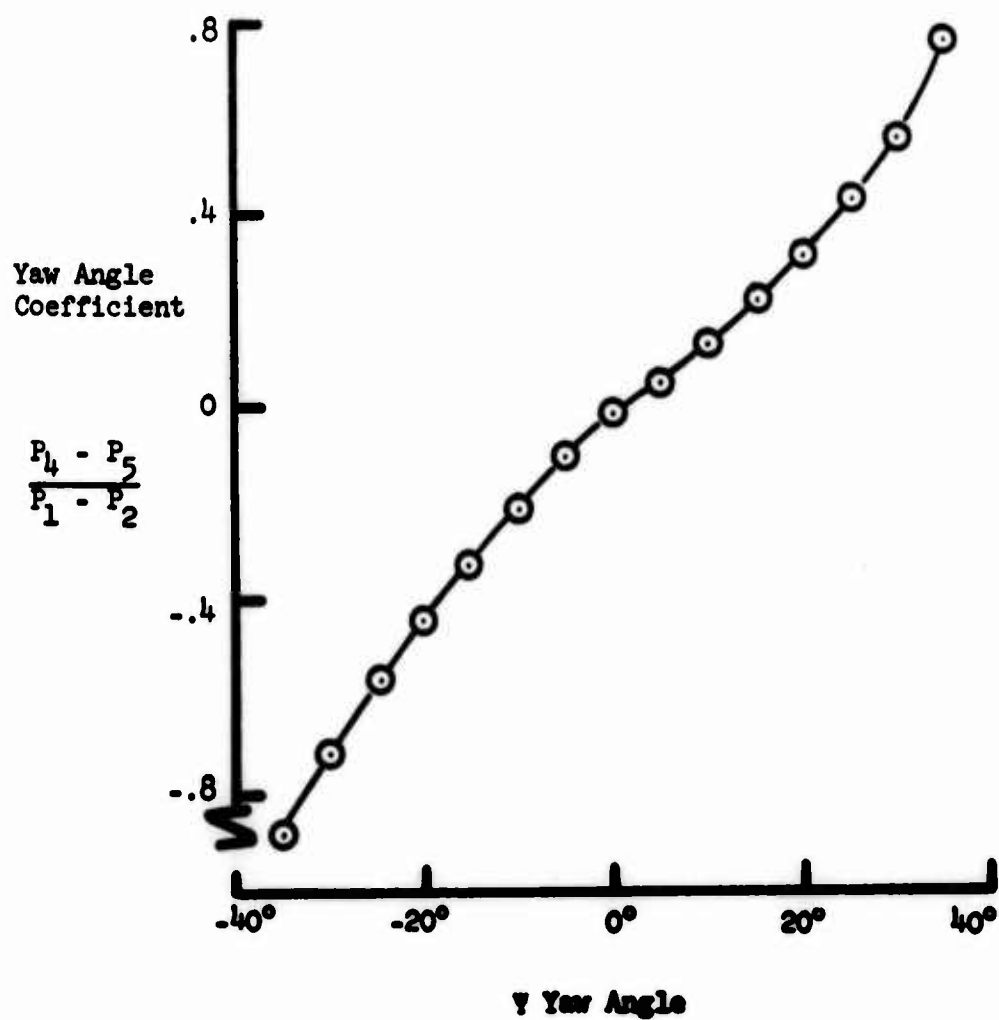


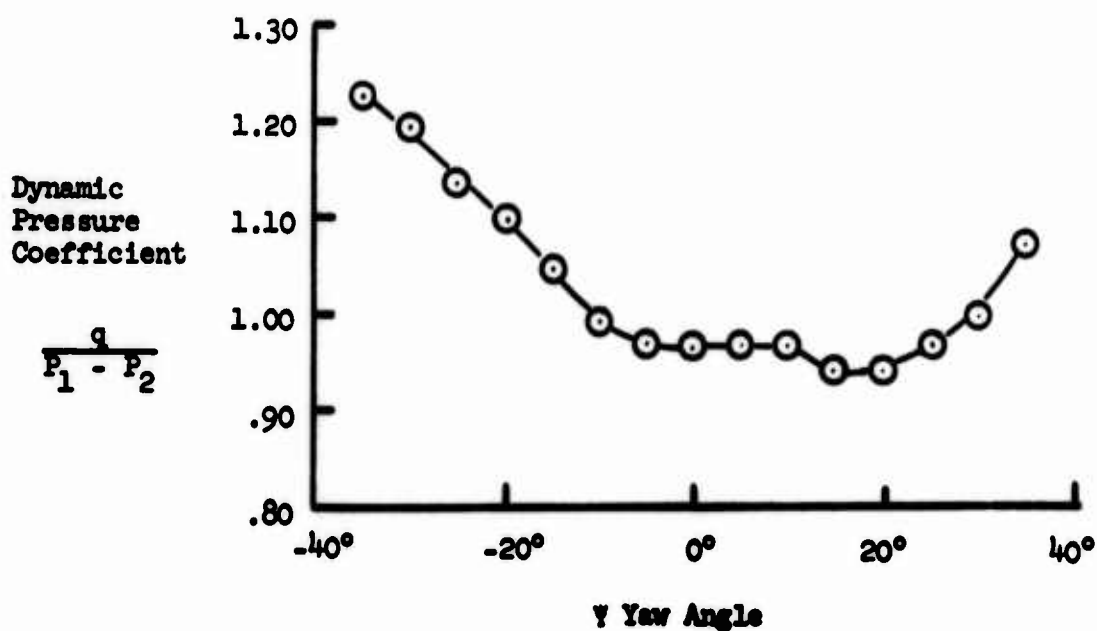
Figure 16. Jet Exit Total Pressure versus  $P_a$  for  $\lambda = 12$ ,  $V_\infty = 50$  ft./sec.



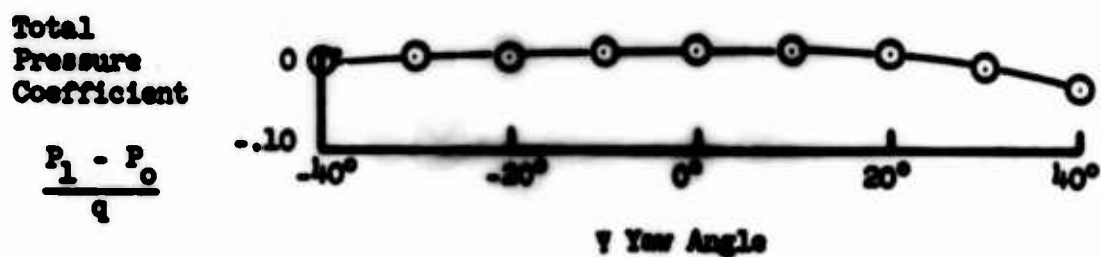


(a) Yaw Angle versus Yaw Angle Coefficient

Figure 17. Pressure Probe Calibration Curves.



(b) Yaw Angle versus Dynamic Pressure Coefficient



(c) Yaw Angle versus Total Pressure Coefficient

Figure 17. Pressure Calibration Curves (Concluded).

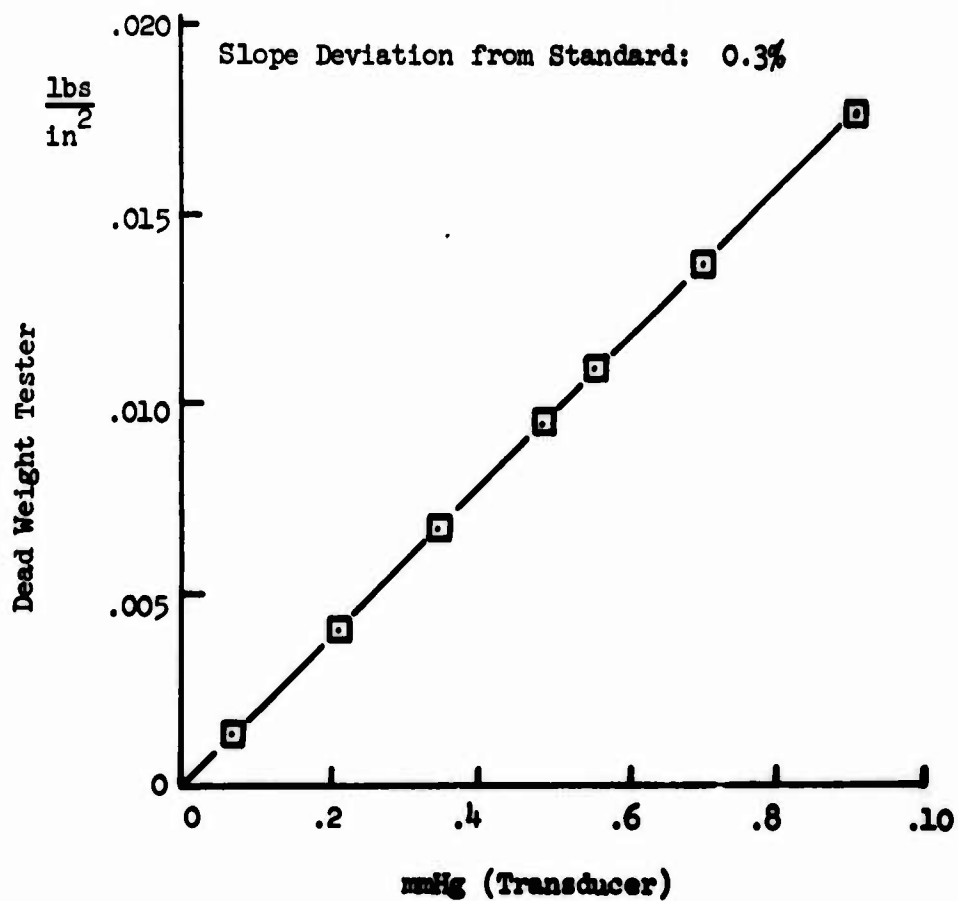


Figure 18. 10mmHg Transducer versus Dead Weight Tester.

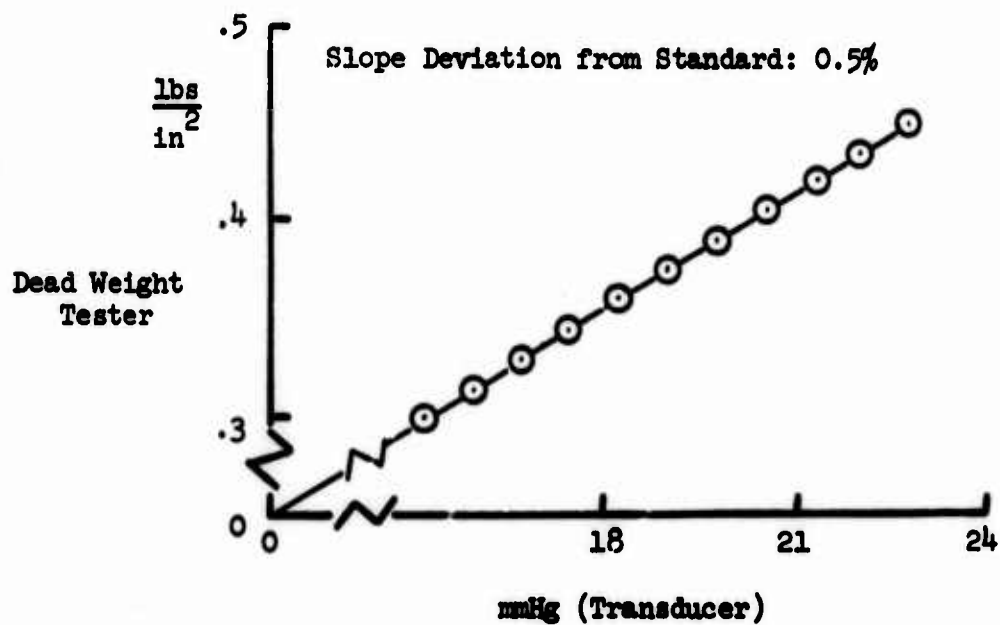


Figure 19. 1000mmHg Transducer versus Dead Weight Tester.



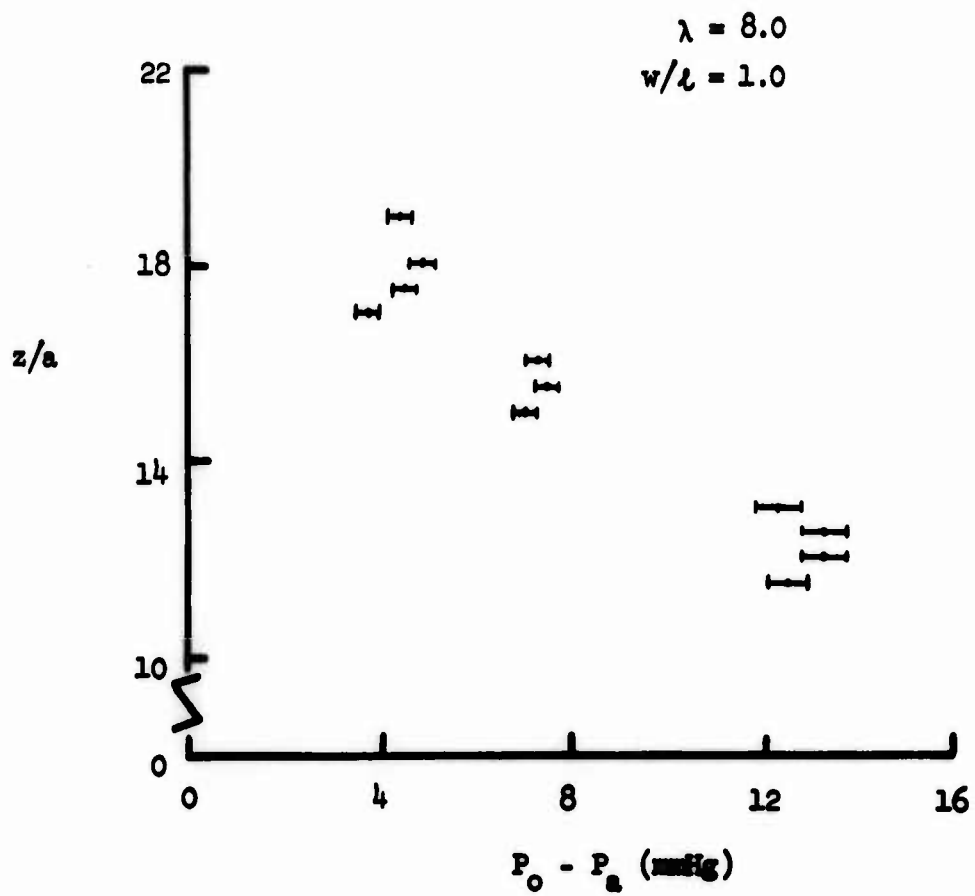
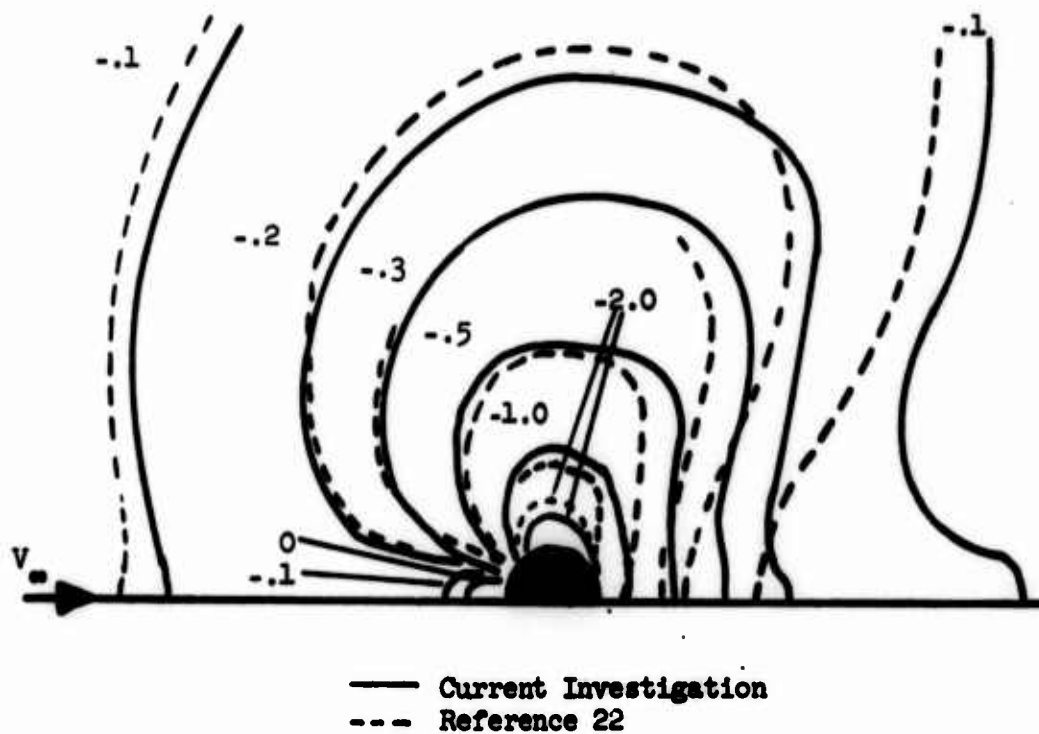


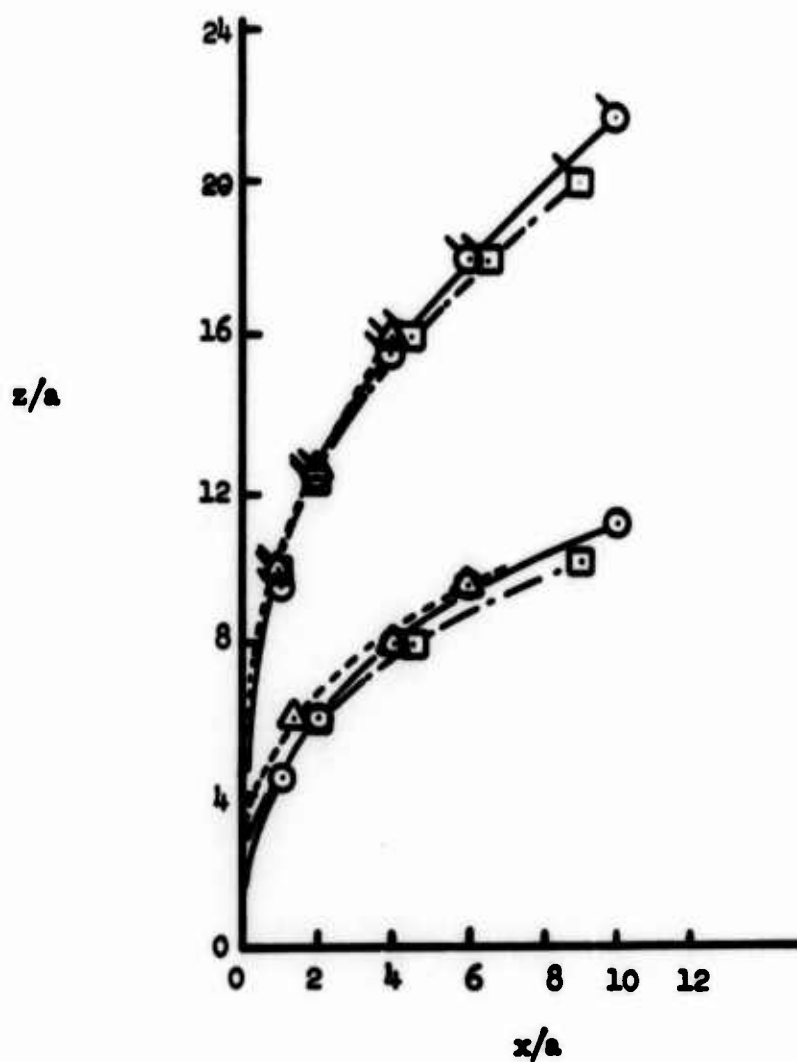
Figure 21. Jet Plume Reading Fluctuations, Typical.



(a) Surface  $C_p$ 's,  $\lambda = 8$ .

Figure 22. Comparison with Other Investigations.

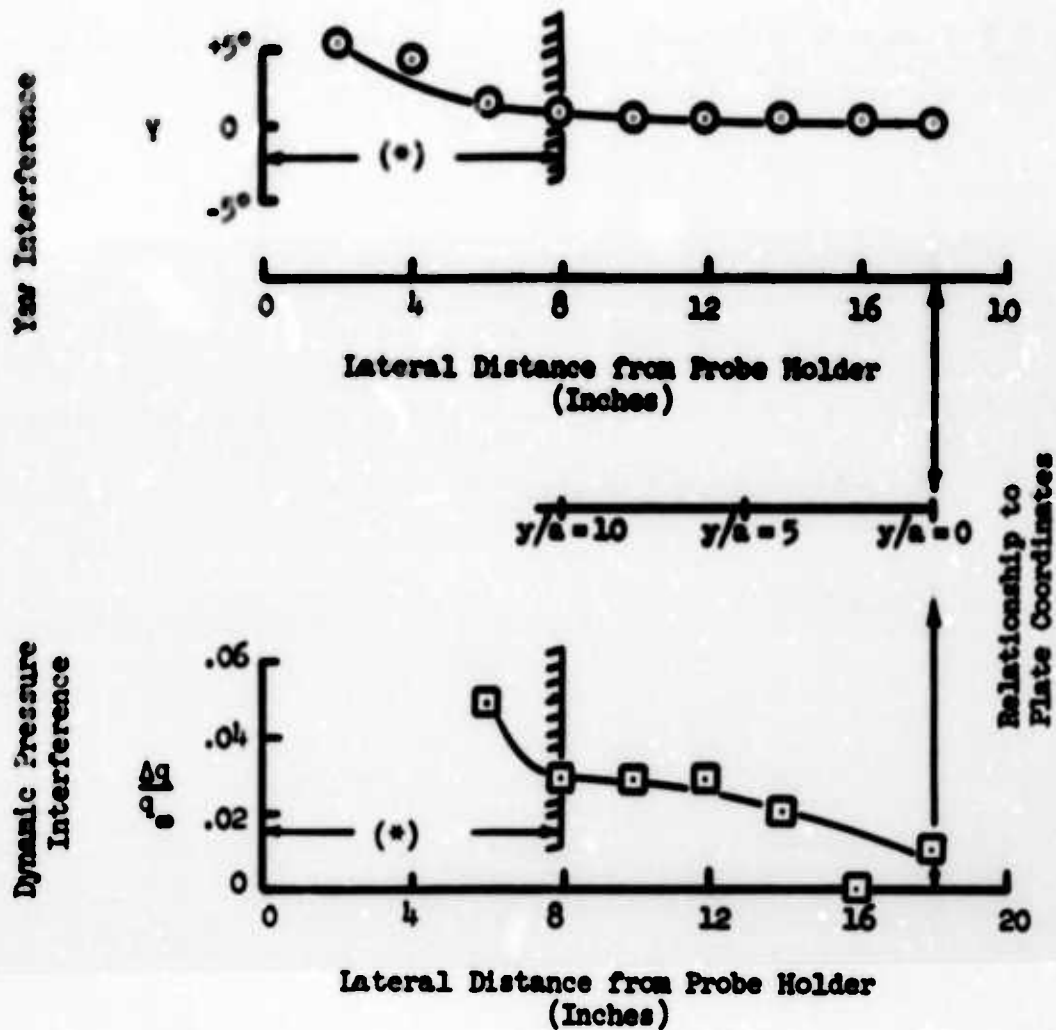
Symbol	Reference	$\lambda$	$w/l$
—○	Present Study	4	1.0
—□	16	4	1.0
---△	17	4	1.0
—○	Present Study	8	1.0
—□	16	8	1.0
---△	17	8	1.0



(b) Jet Paths

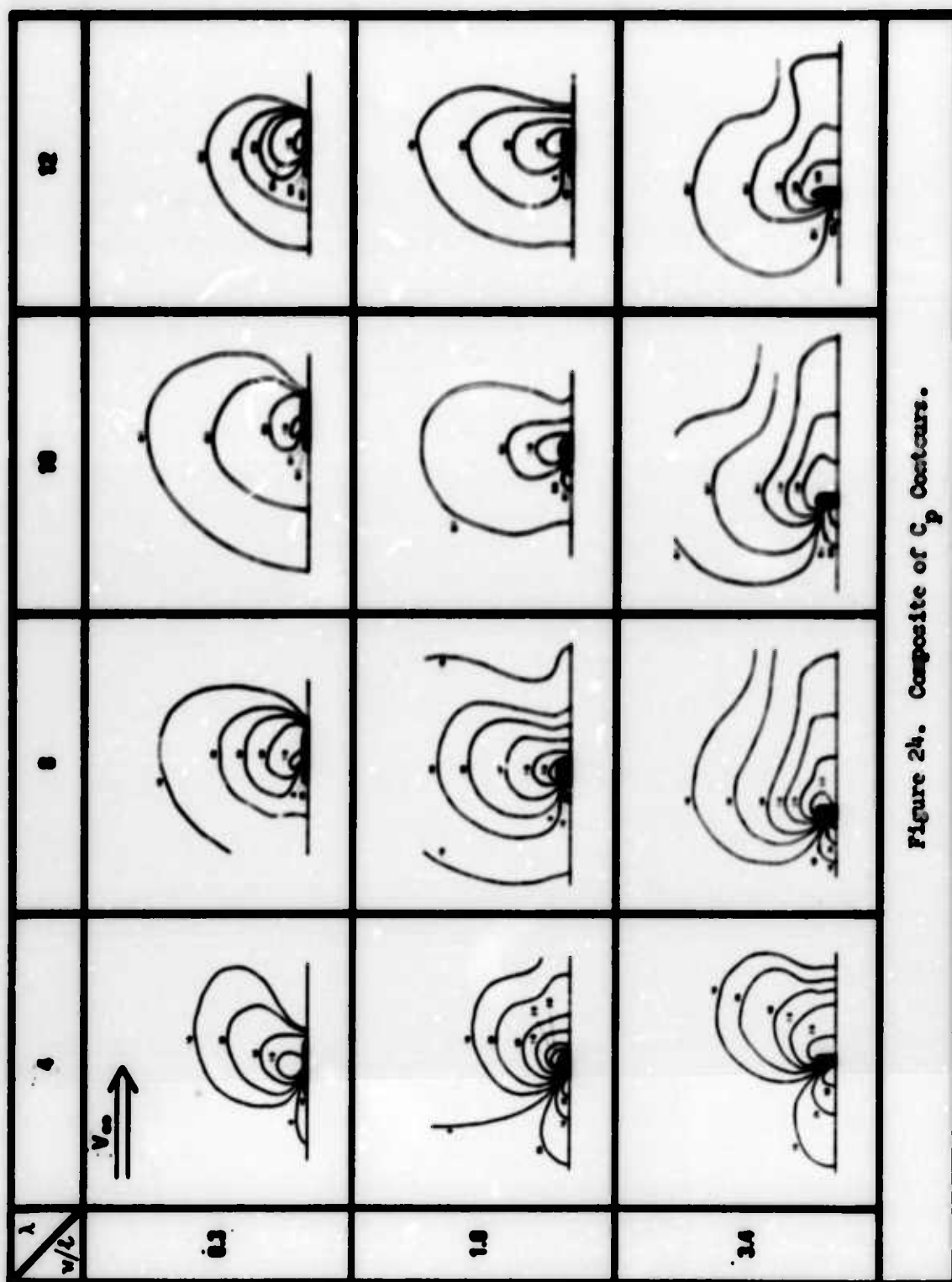
Figure 22. Comparison with Other Investigations (Concluded).





\*Note: No test data taken close to probe holder in this region.

Figure 23. Probe Holder Interference.

Figure 24. Composite of  $C_p$  Contours.

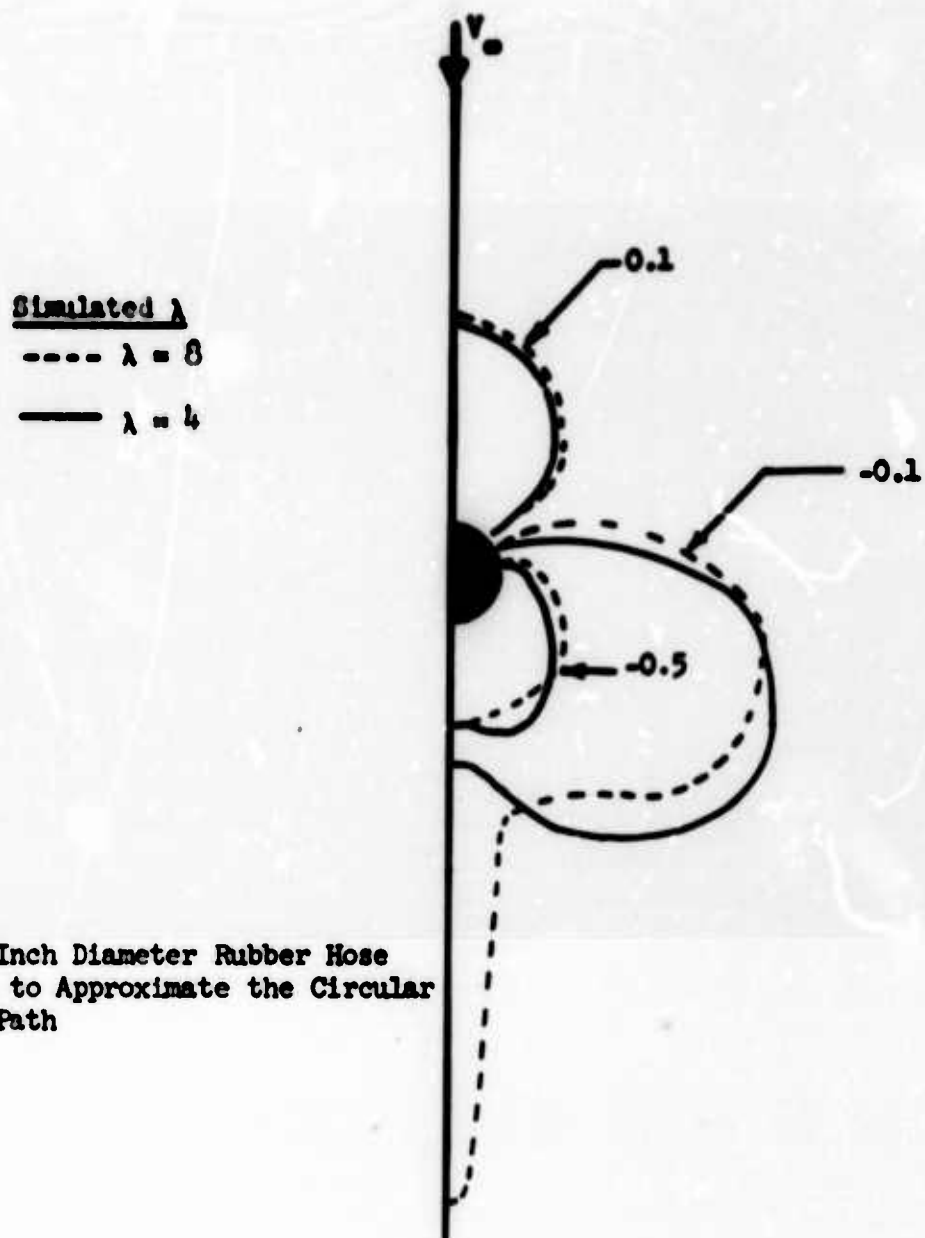
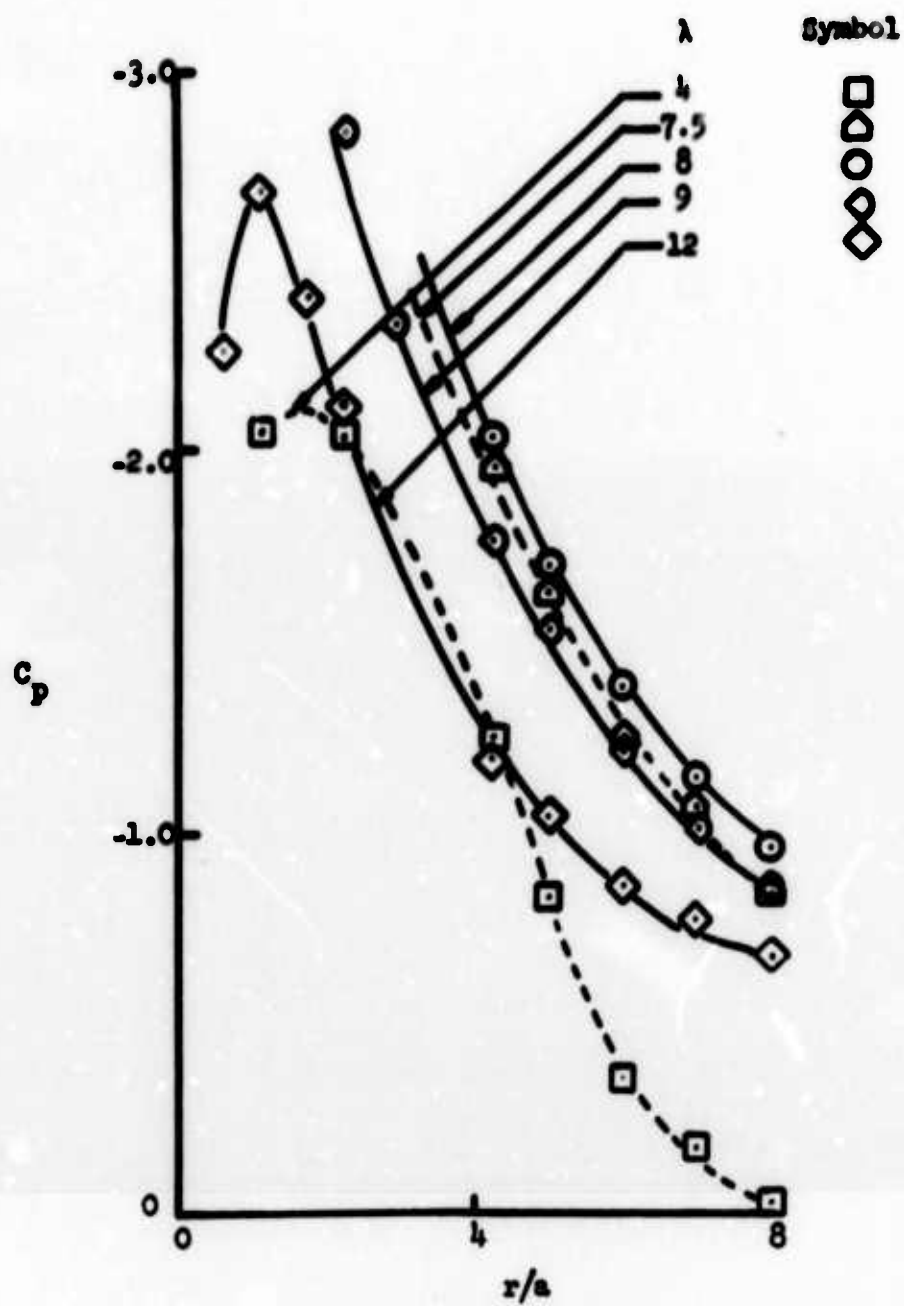
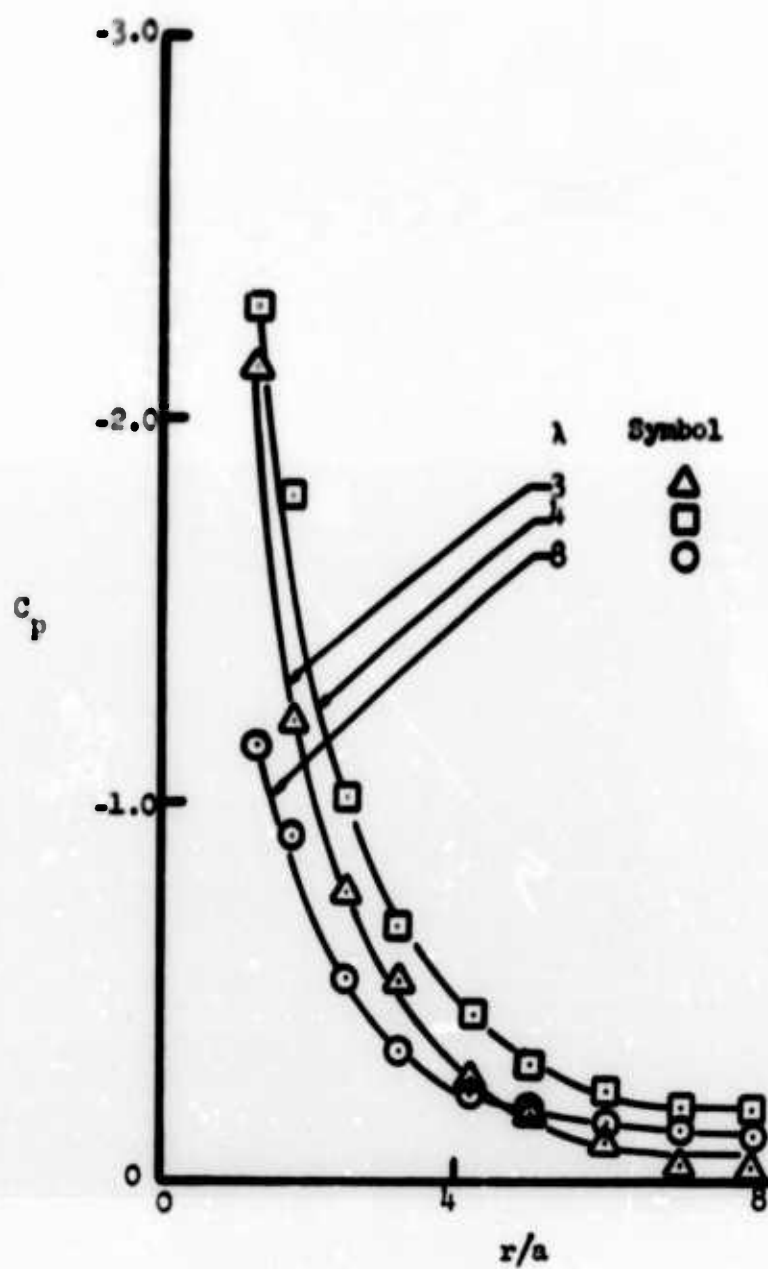


Figure 25.  $C_p$  Contours Around Solid Blockage Model.



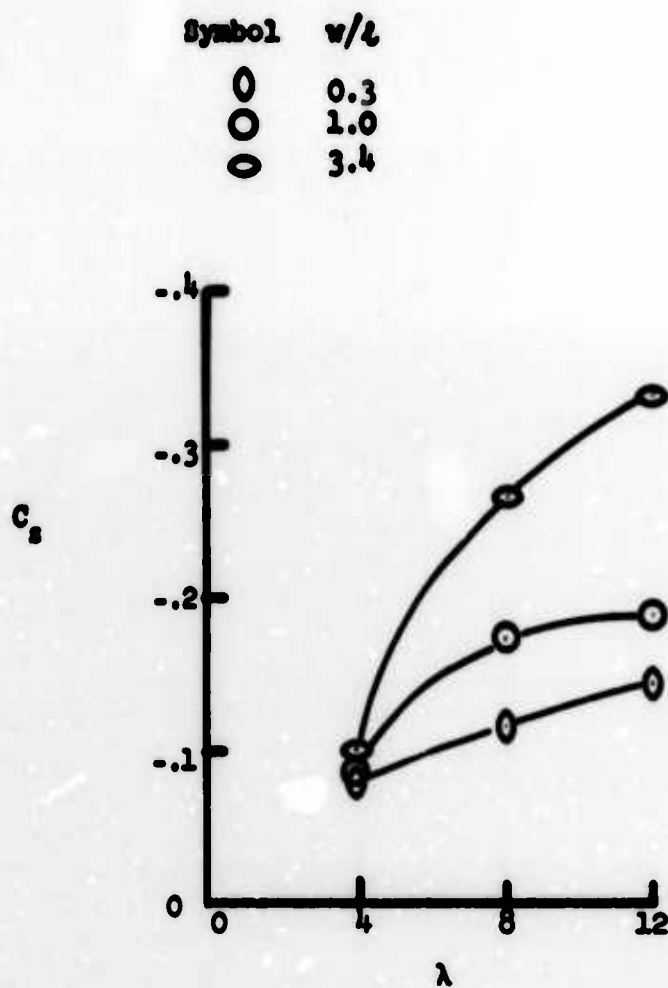
(a)  $w/l = 3.4$

Figure 26. Surface Pressures Behind the Jet,  $\beta = 180^\circ$ .



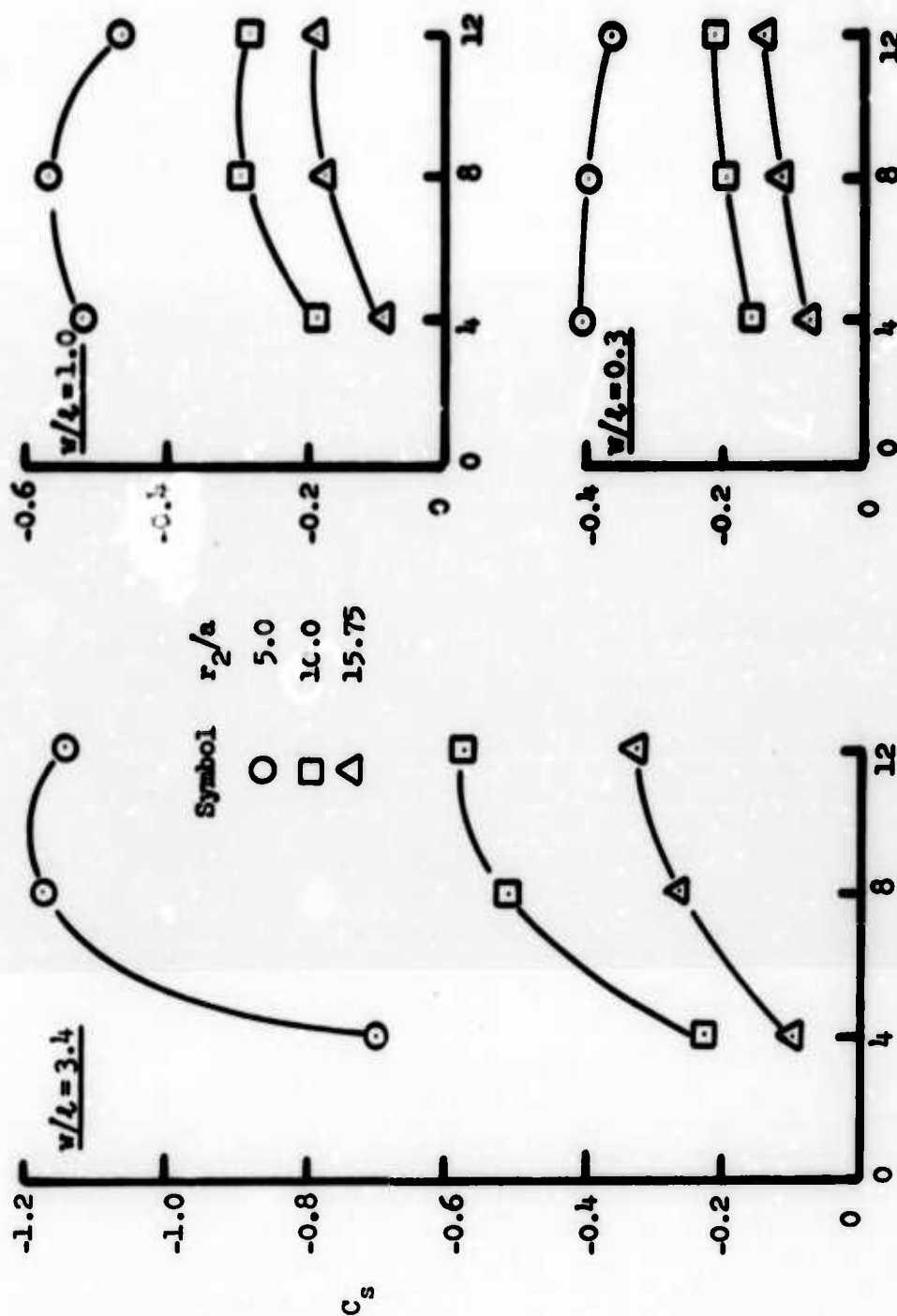
(b)  $w/l = 1.0$

Figure 26. Surface Pressures Behind the Jet,  $\beta = 160^\circ$  (Concluded).



(a) Effect of Exit Configuration at  $r_2/a = 15.75$ .

Figure 27. Mean Surface Pressures.



(b) Effect of Upper Limit of Integration.

Figure 27. Mean Surface Pressures (Concluded).

$$\bar{x} = \frac{\int_0^R \int_0^{2\pi} c_p x r dr d\theta}{\int_0^R \int_0^{2\pi} c_p r dr d\theta}$$

Symbol	w/l
$\triangle$	3.4
$\square$	1.0
$\circ$	0.3

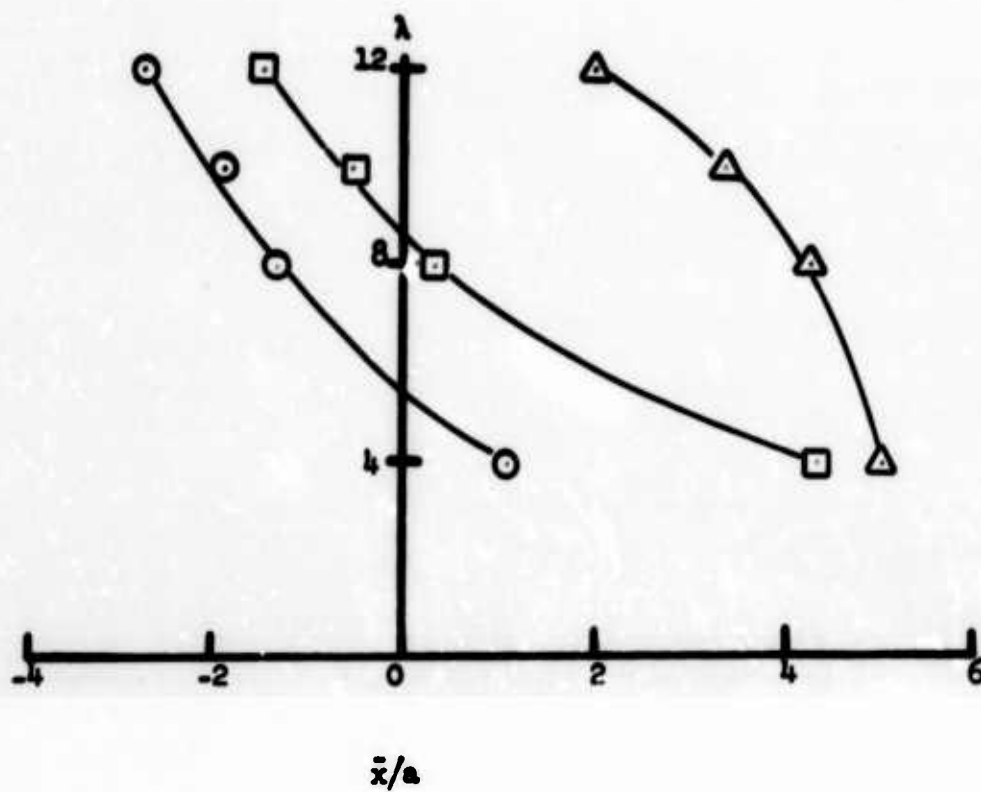


Figure 28. Center of Pressure.





(b)  $w/l = 0.3, \lambda = 8.$



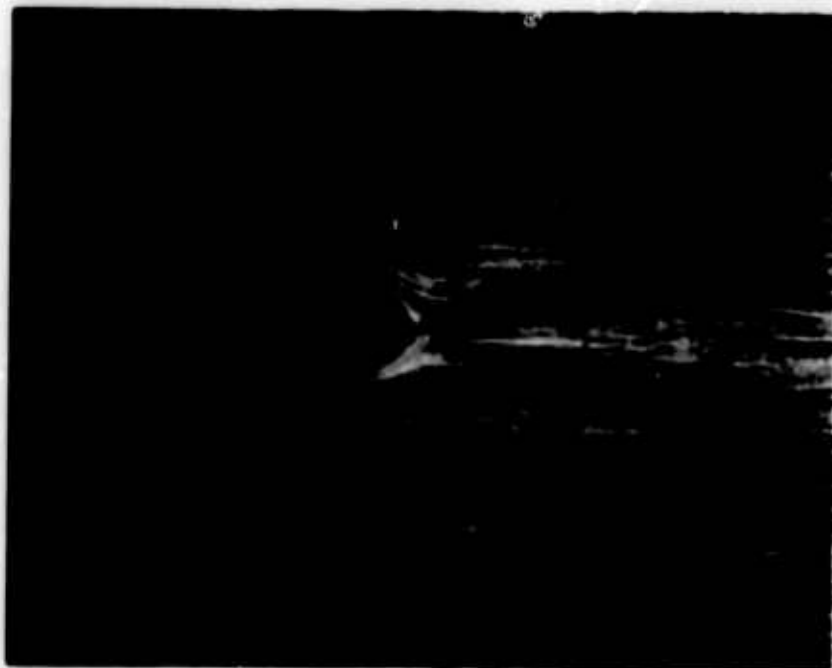
(a)  $w/l = 0.3, \lambda = 4.$



Figure 29. Oil Studies.



(c)  $w/l = 0.3$ ,  $\lambda = 12$ .



(d)  $w/l = 0.3$ ,  $\lambda = 0$  (Solid Blockage).

Figure 29. Oil Studies (Continued).

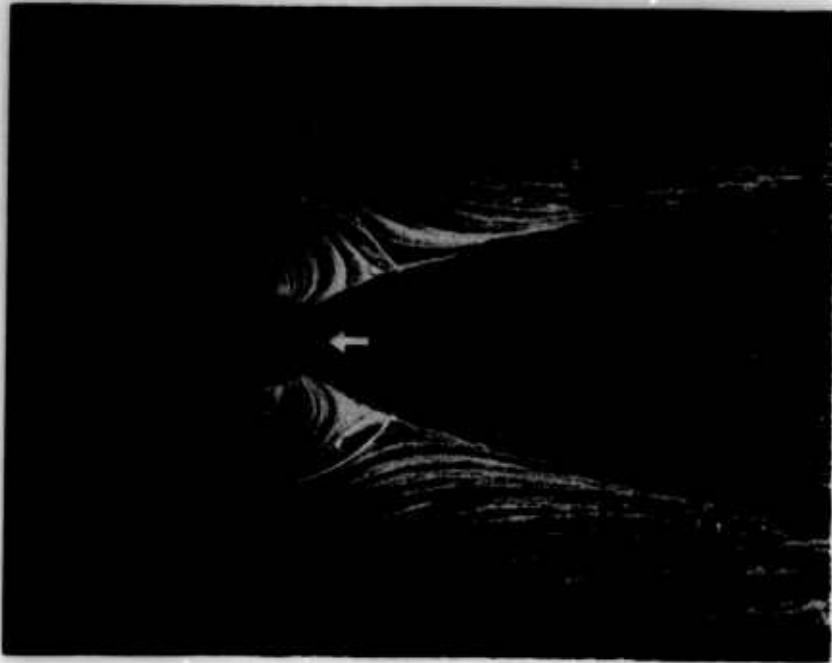


(e)  $w/l = 1.0$ ,  $\lambda = 4$ .

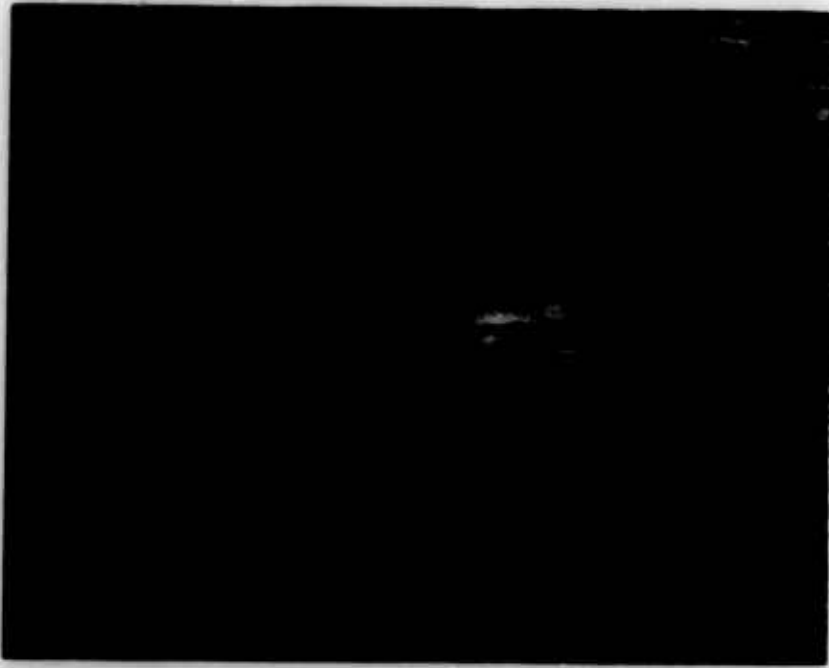


(f)  $w/l = 1.0$ ,  $\lambda = 8$ .

Figure 29. Oil Studies (Continued).

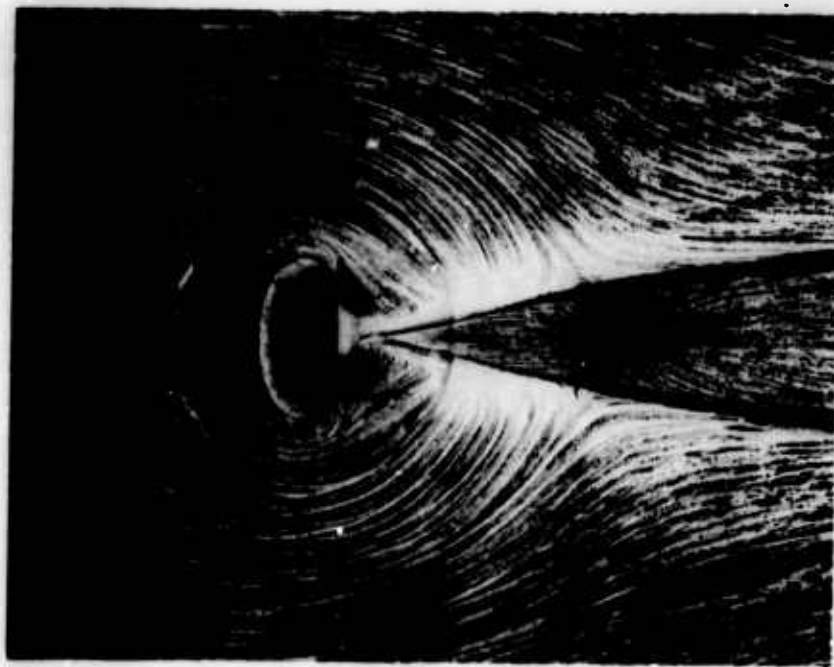


(g)  $w/l = 1.0, \lambda = 12.$

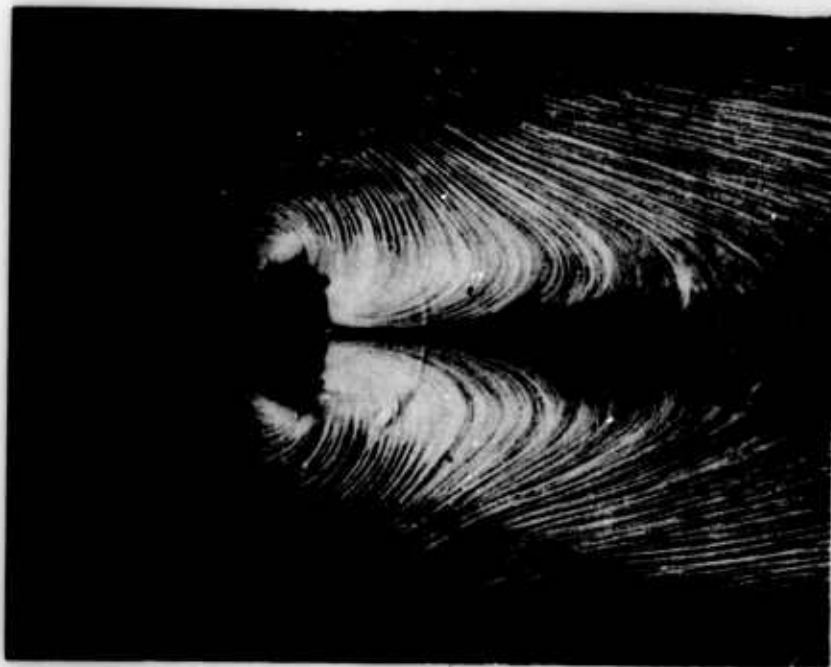


(h)  $w/l = 1.0, \lambda = 0$  (Solid Blockage).

Figure 29. Oil Studies (Continued).

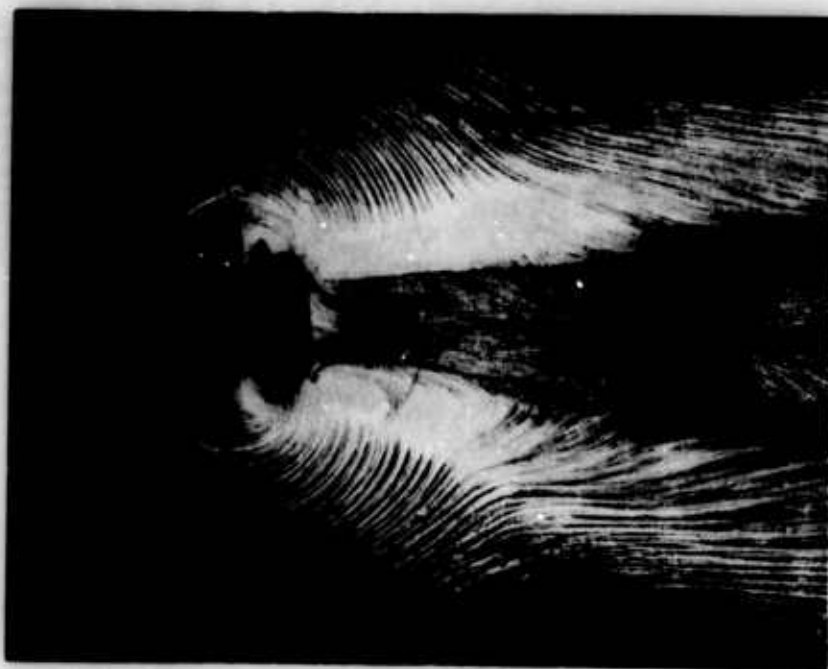


(i)  $w/l = 3.4$ ,  $\lambda = 4$ .

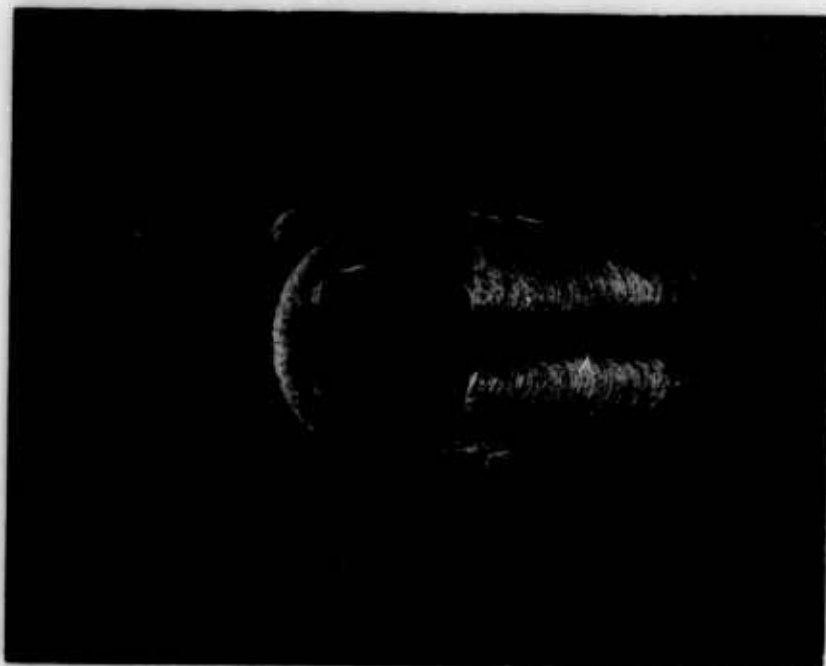


(j)  $w/l = 3.4$ ,  $\lambda = 8$ .

Figure 29. Oil Studies (Continued).



(k)  $w/l = 3.4$ ,  $\lambda = 12$ .



(l)  $w/l = 3.4$ ,  $\lambda = 0$  (Solid Blockage).

Figure 29. Oil Studies (Concluded).

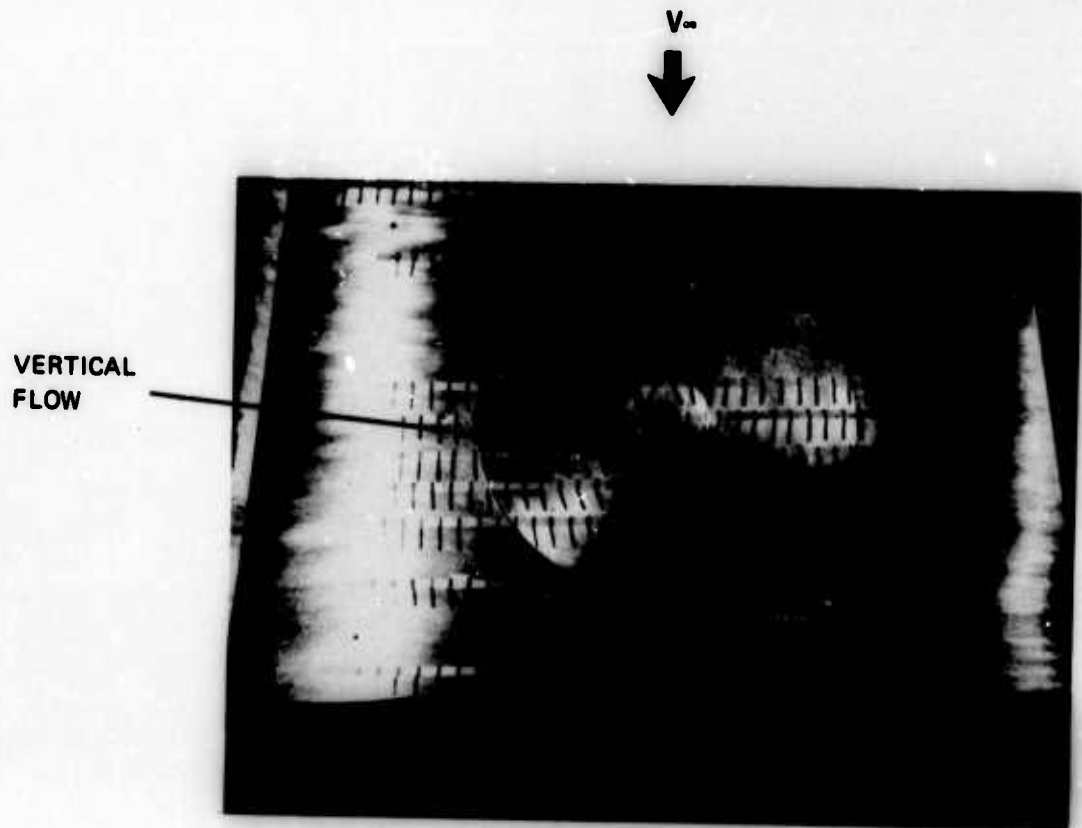


Figure 30. Tuft Study,  $w/l = 1.0$ ,  $\gamma$

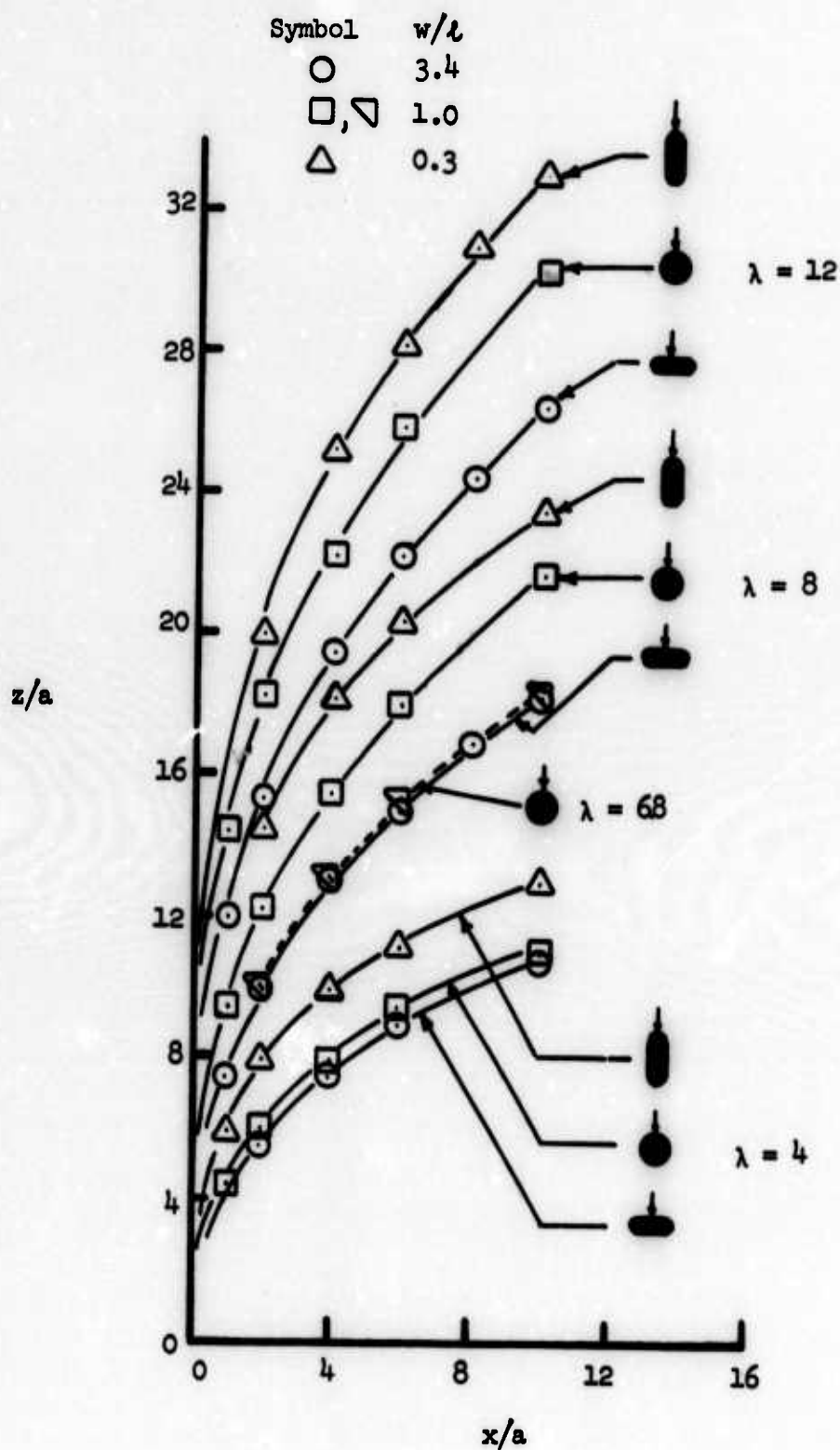


Figure 31. Jet Paths.



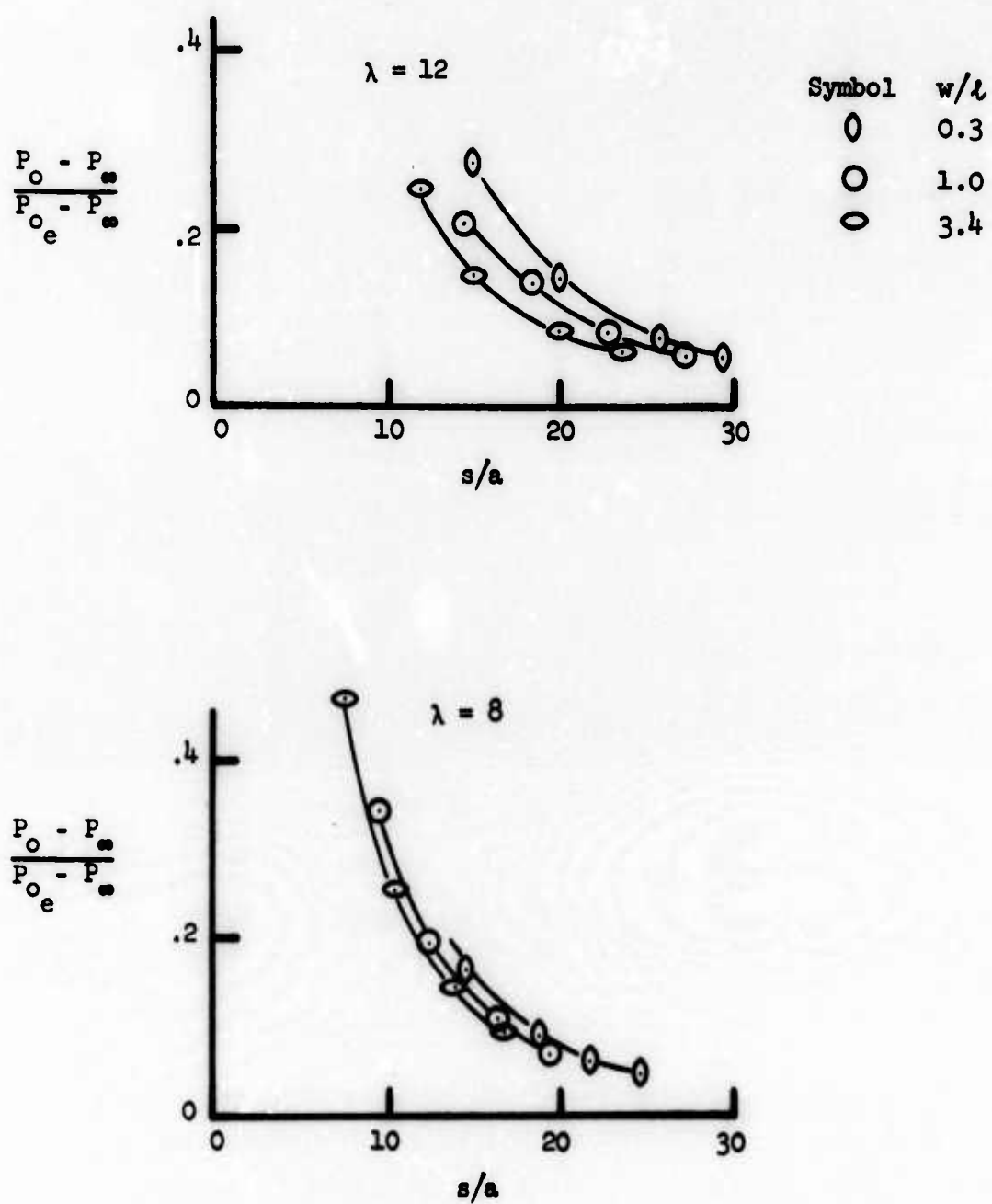
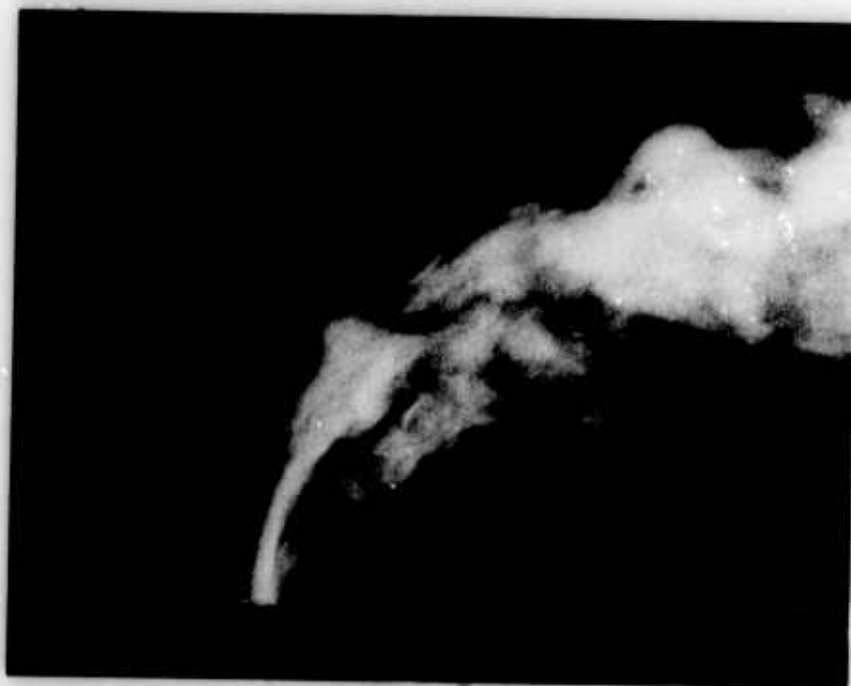
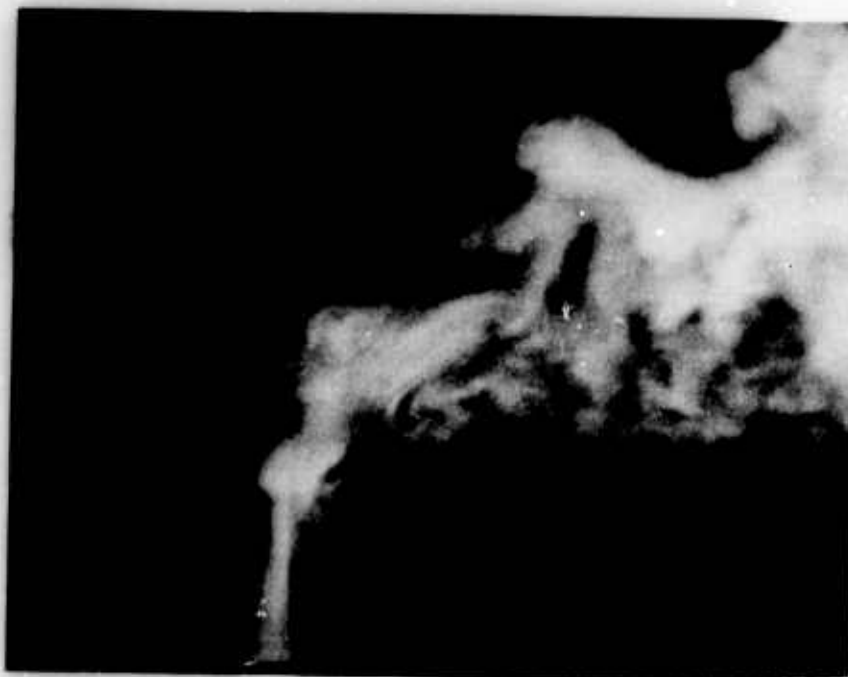


Figure 32. Total Pressure Decay Along Jet Path.



(a)  $w/l = 3.4$



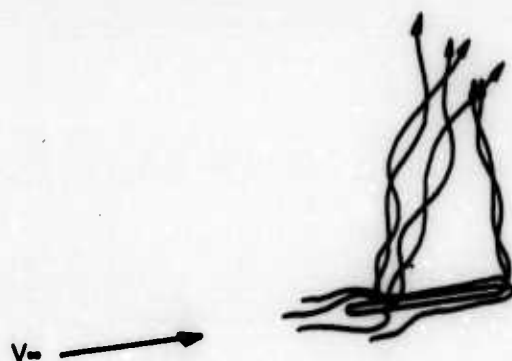
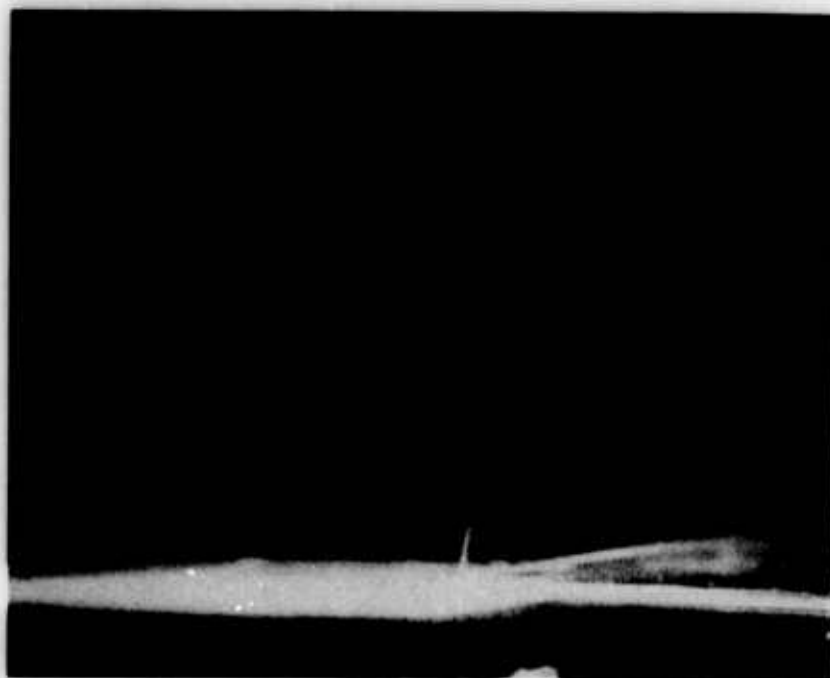
(b)  $w/l = 1.0$

Figure 33. Smoke Studies, Jet Injection.



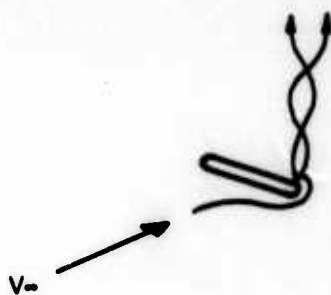
(c)  $w/l = 0.3$

Figure 33. Smoke Studies, Jet Injection (Concluded).



(a)  $w/l = 0.3$

Figure 34. Smoke Studies, Cross Flow Injection.



(b)  $w/l = 3.4$

Figure 34. Smoke Studies, Cross Flow Injection (Concluded).

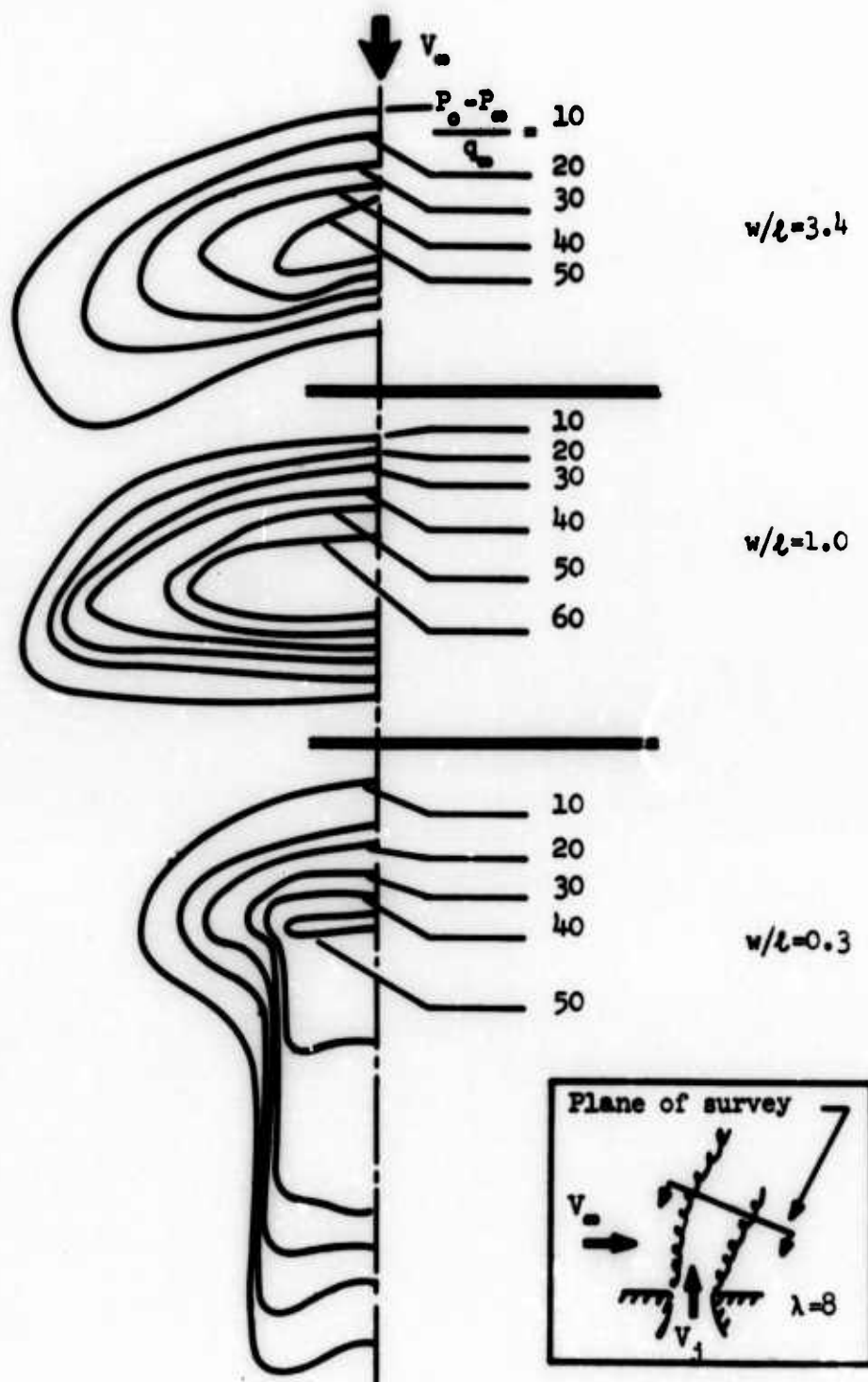


Figure 35. Total Pressure Contours in Plume Cross-Section,  $z/a=5$ ,  $\lambda=8$ .

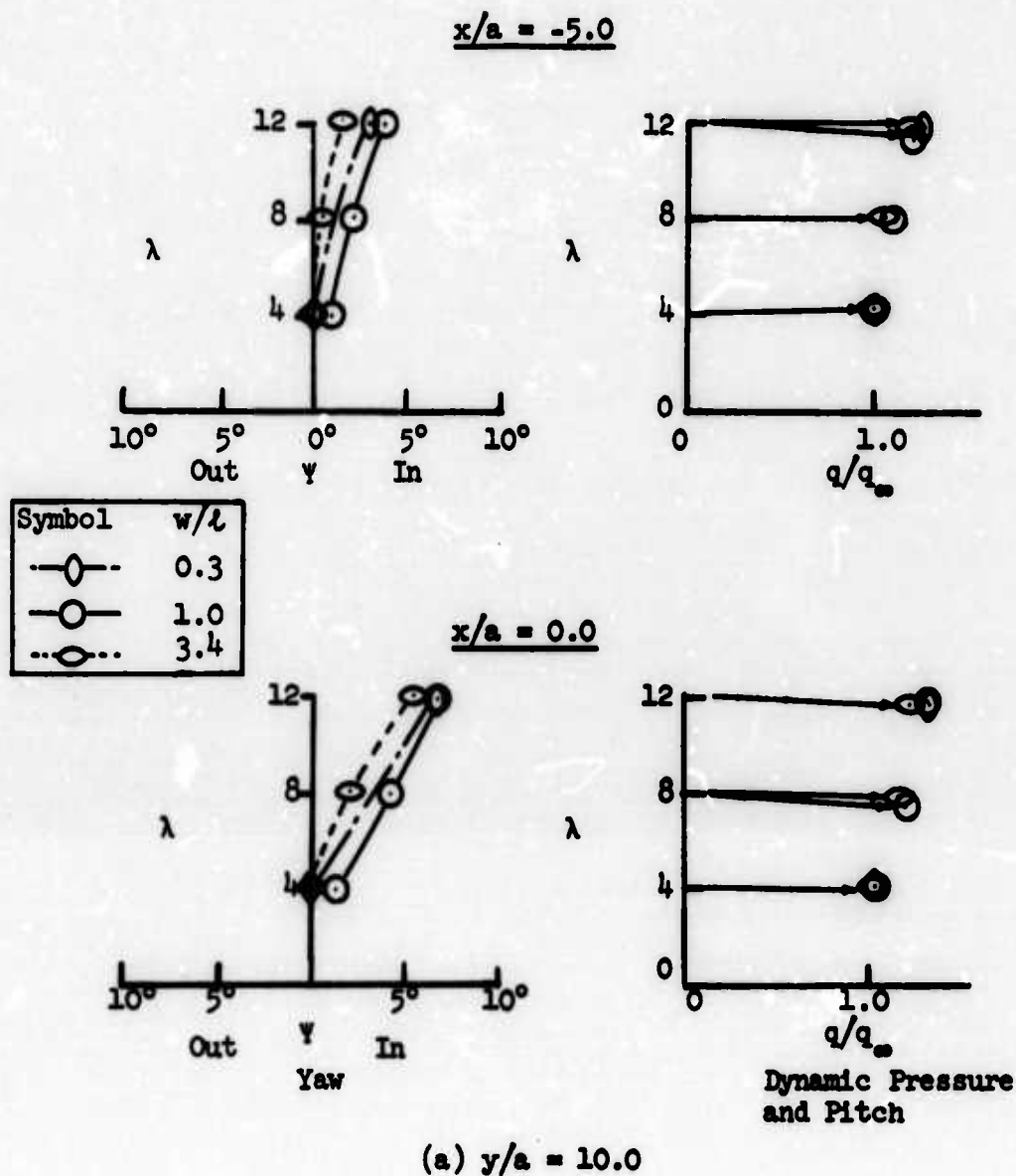
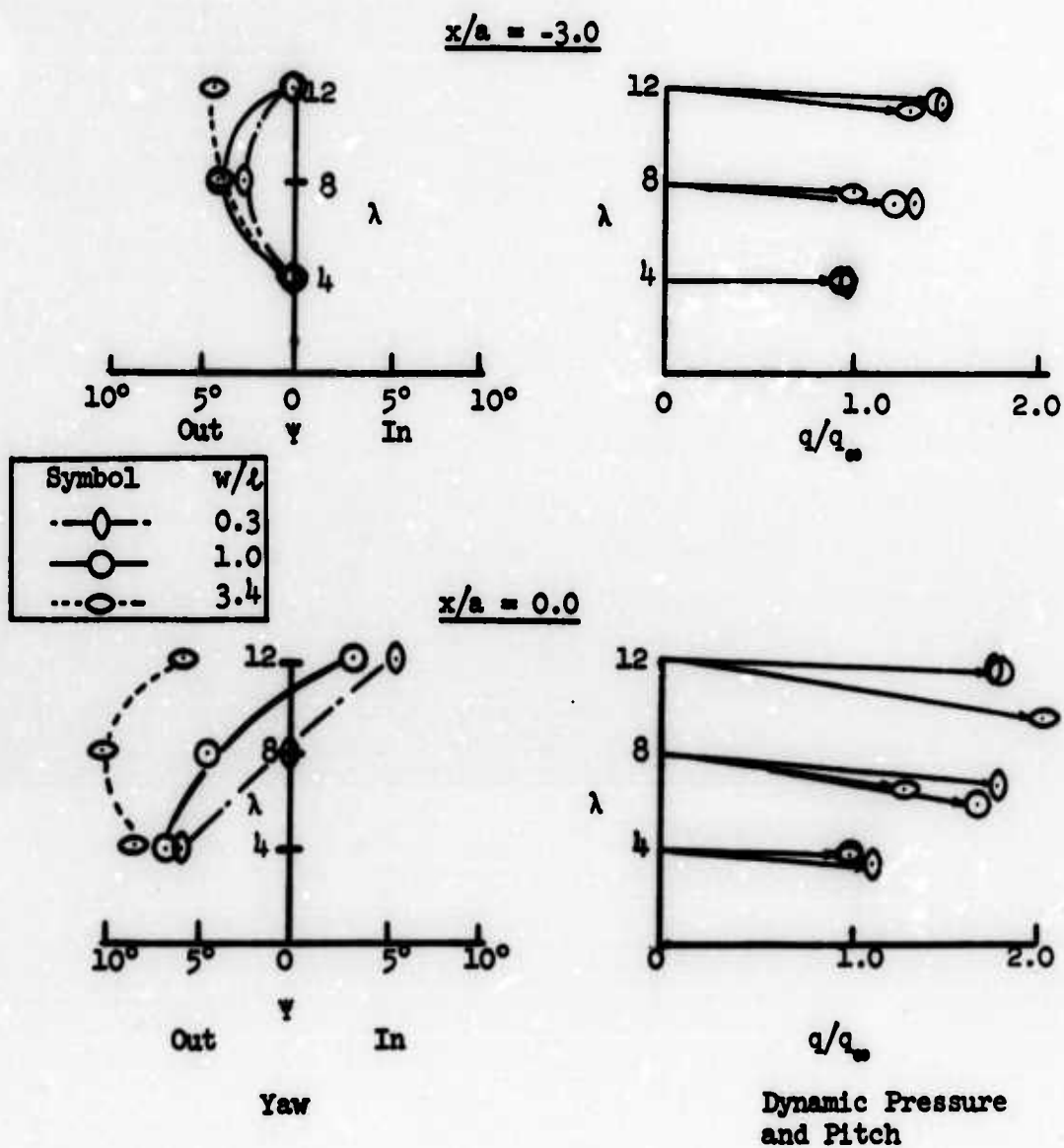


Figure 36. Lateral Flow Field Surveys at  $z/a = 6.0$ .



(b)  $y/a = 4.0$

Figure 36. Lateral Flow Field Surveys at  $z/a = 6.0$  (Concluded).



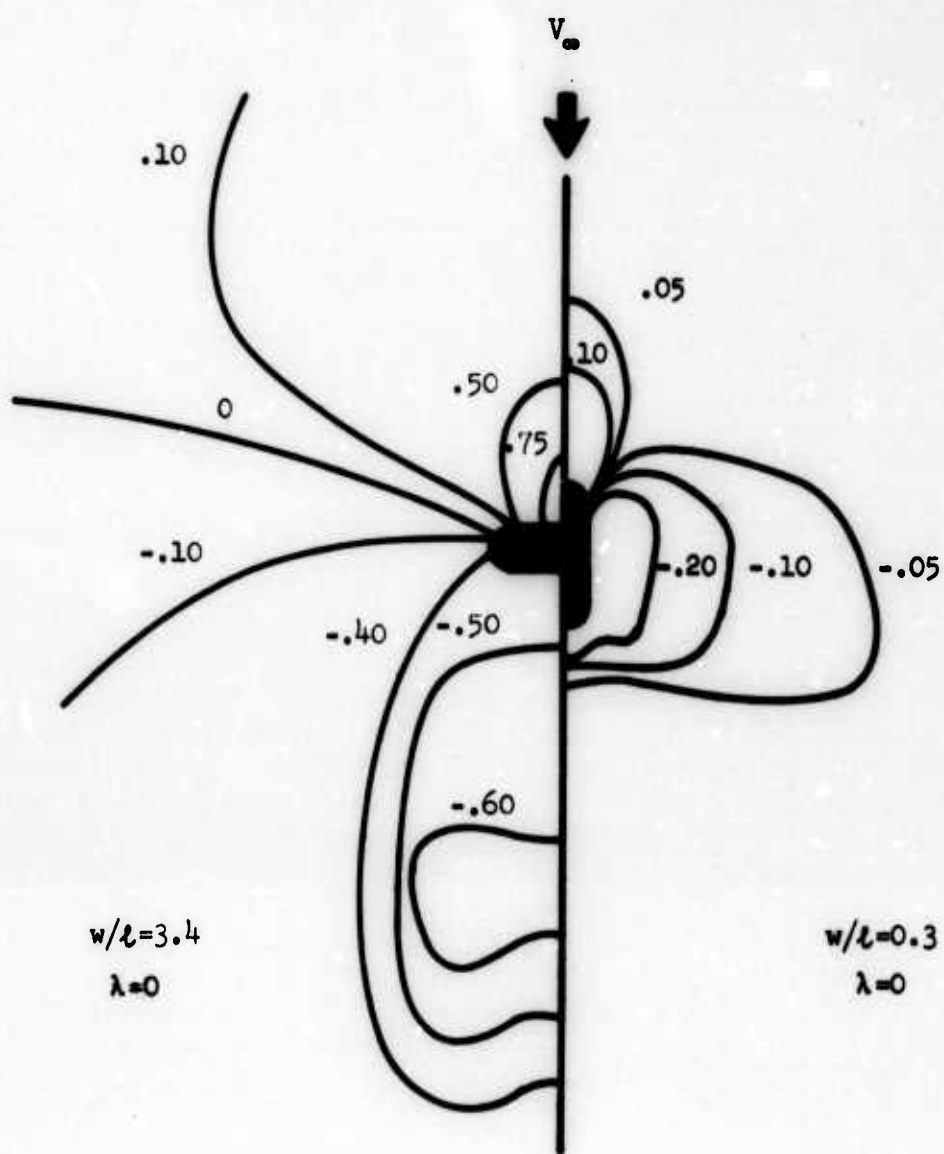


Figure 37. Surface  $C_p$  Contours for Solid Blockage Models.

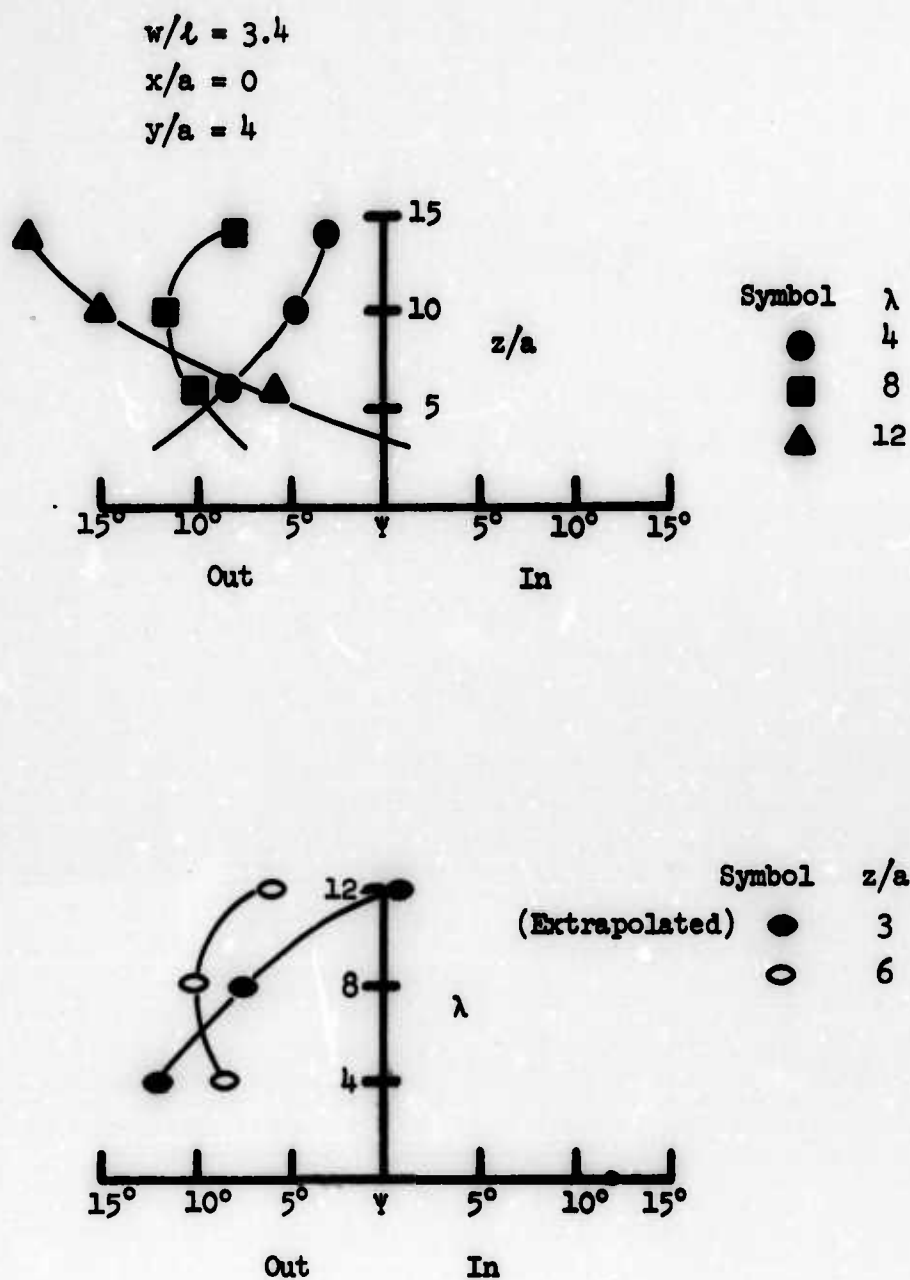
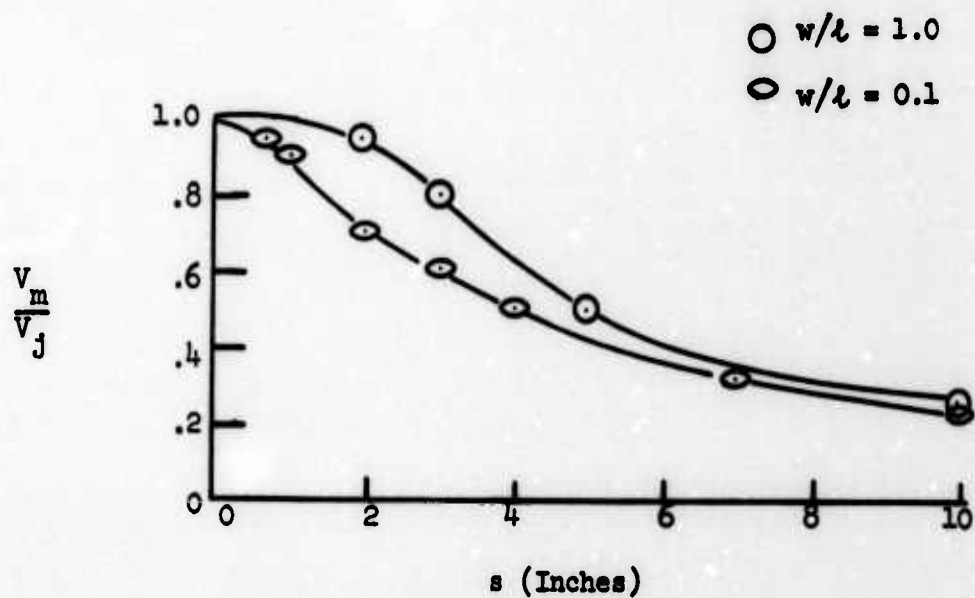
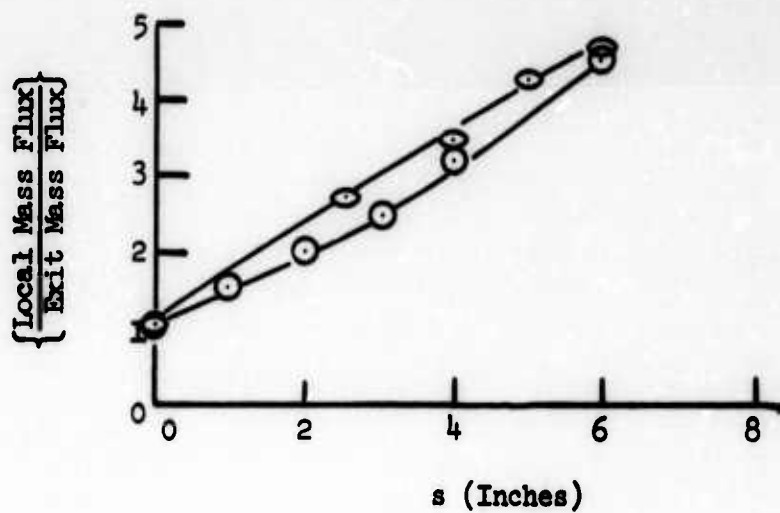


Figure 38. Effect of Extrapolation from  $z/a > 6$ ;  
 $w/\lambda = 3.4$ ,  $x/z = 0$ ,  $y/z = 4$ .



(a) Free Jet Velocity Decay



(b) Free Jet Entrainment

Figure 39. Free Jet Velocity Decay and Entrainment Data (from Reference 43).

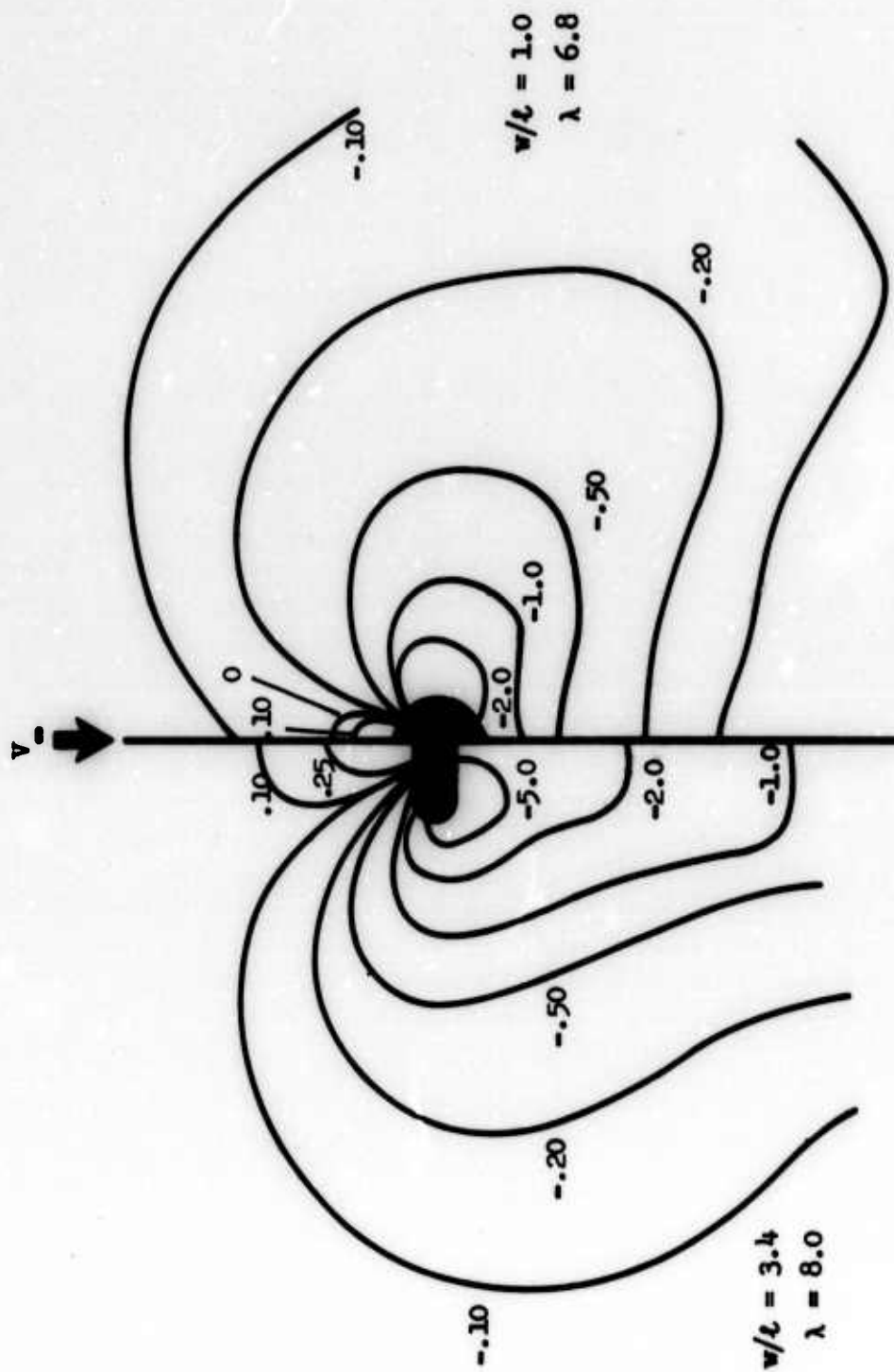


Figure 40. Surface Pressures for Matching Jet Paths.

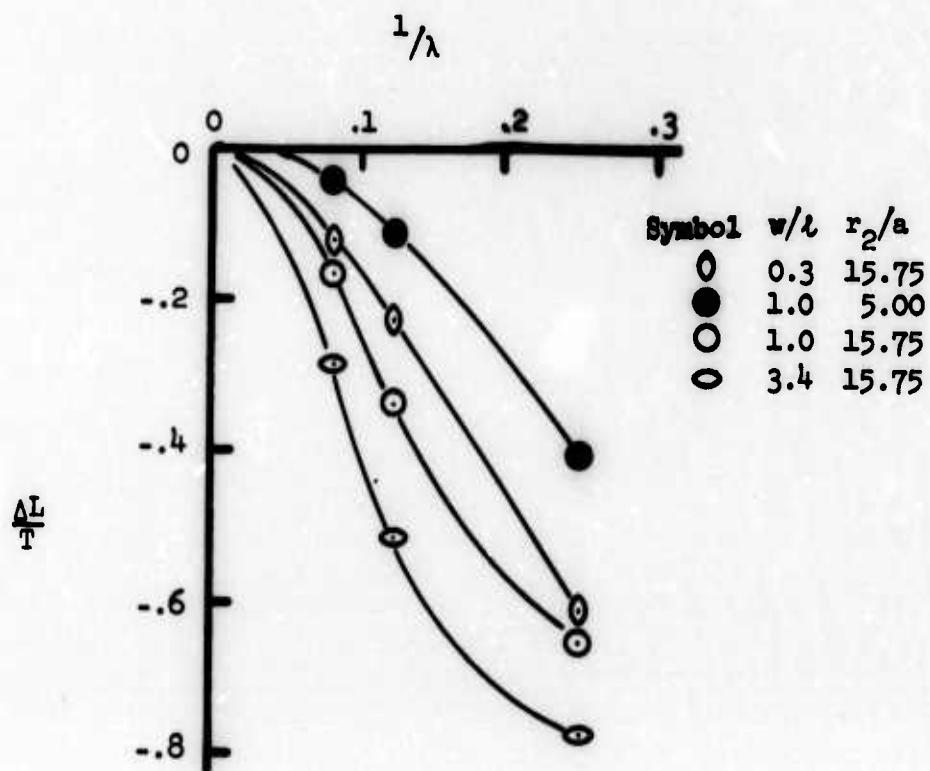


Figure 41. Interference Lift Loss as a Fraction of Thrust.

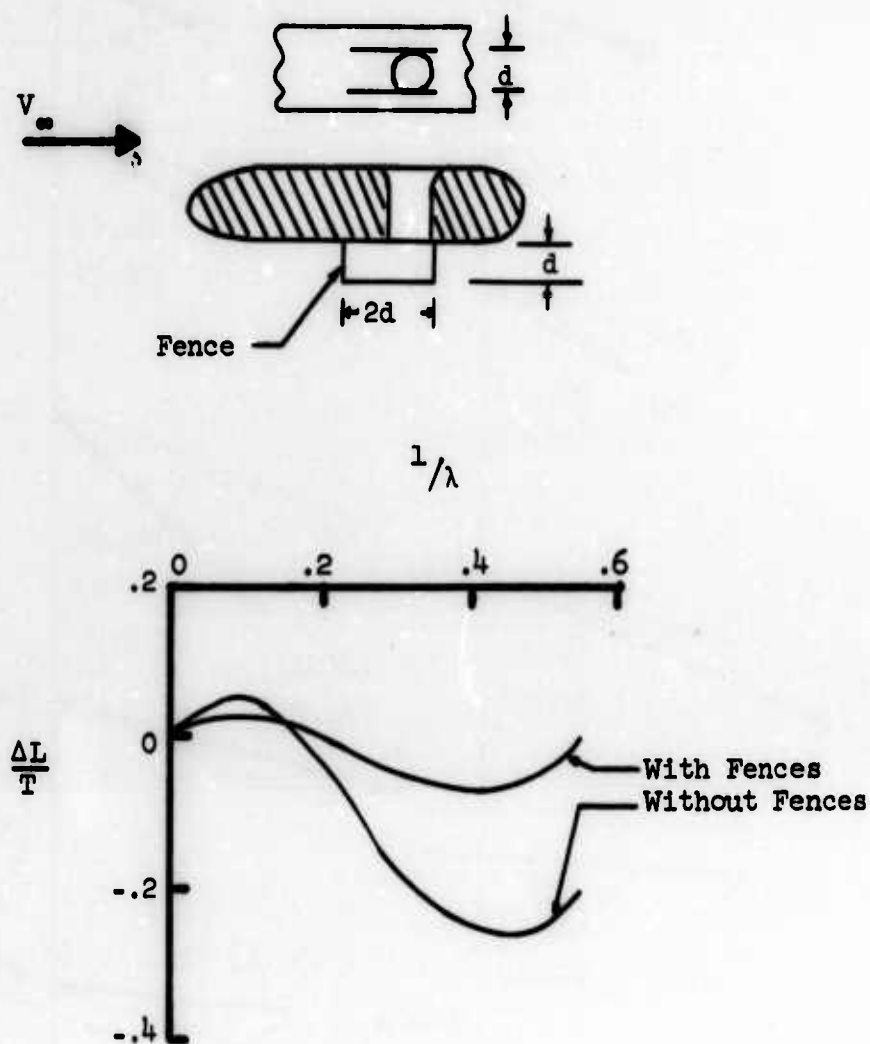


Figure 42. Attenuation of Lift Loss  
(from Reference 26).

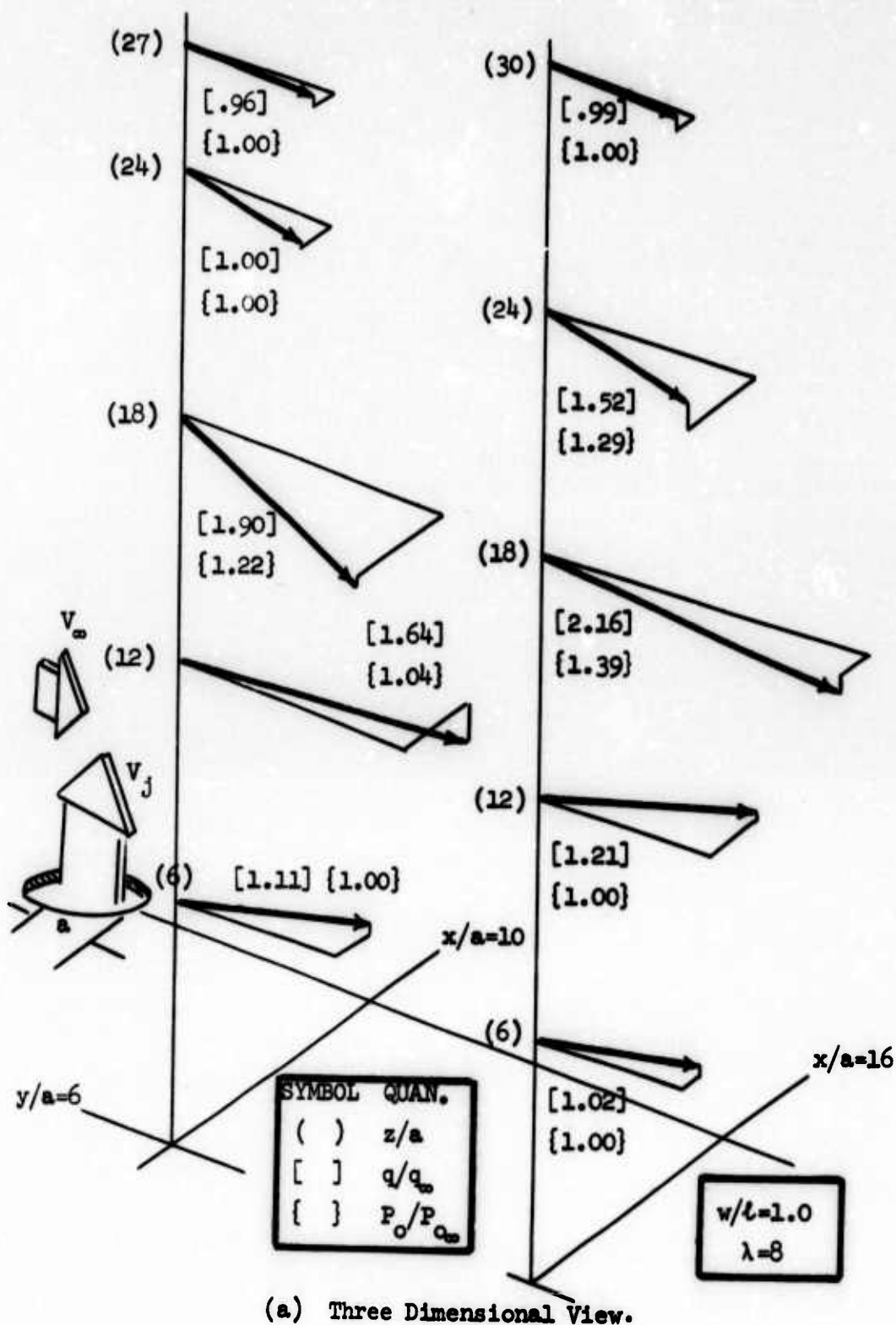
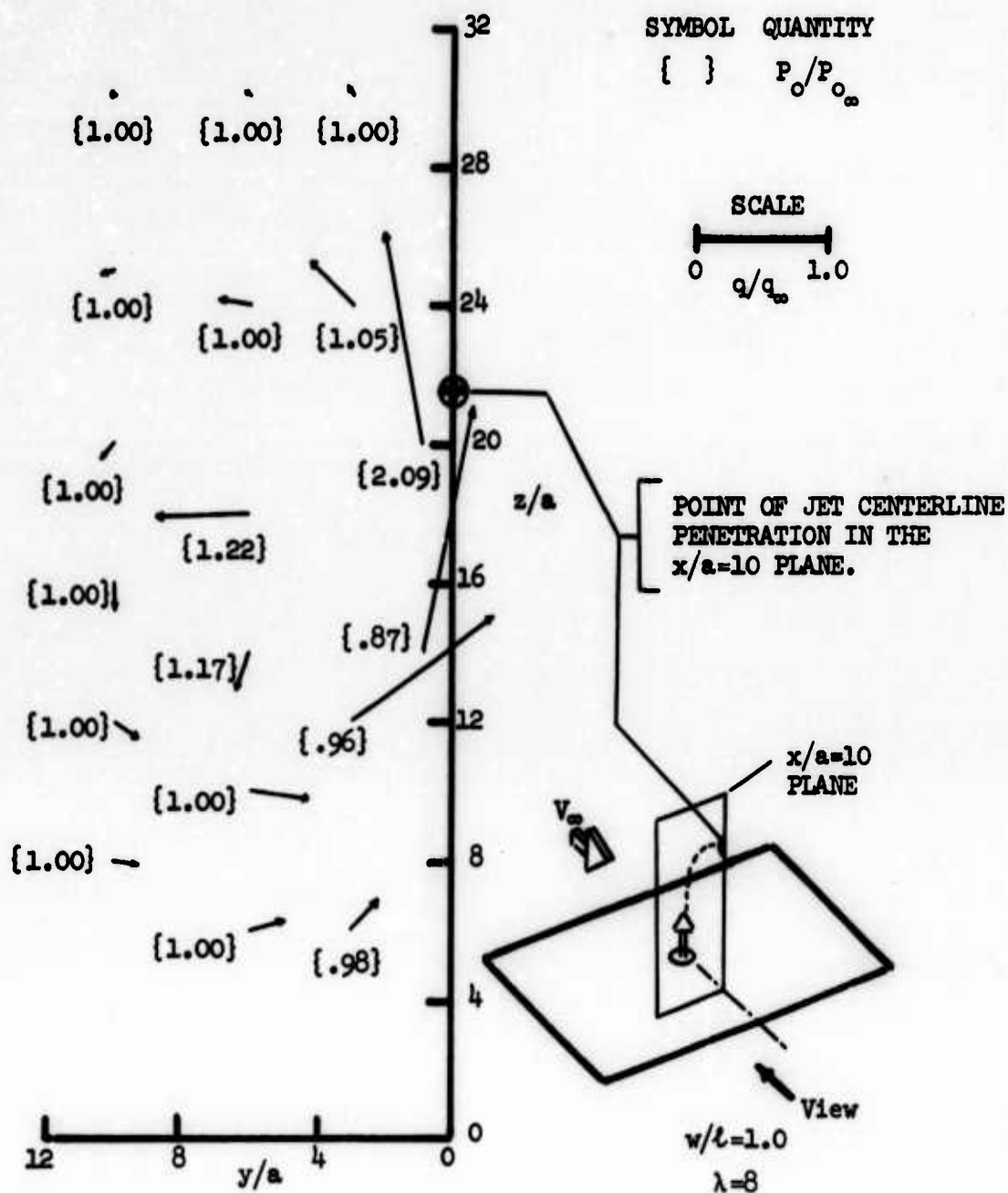


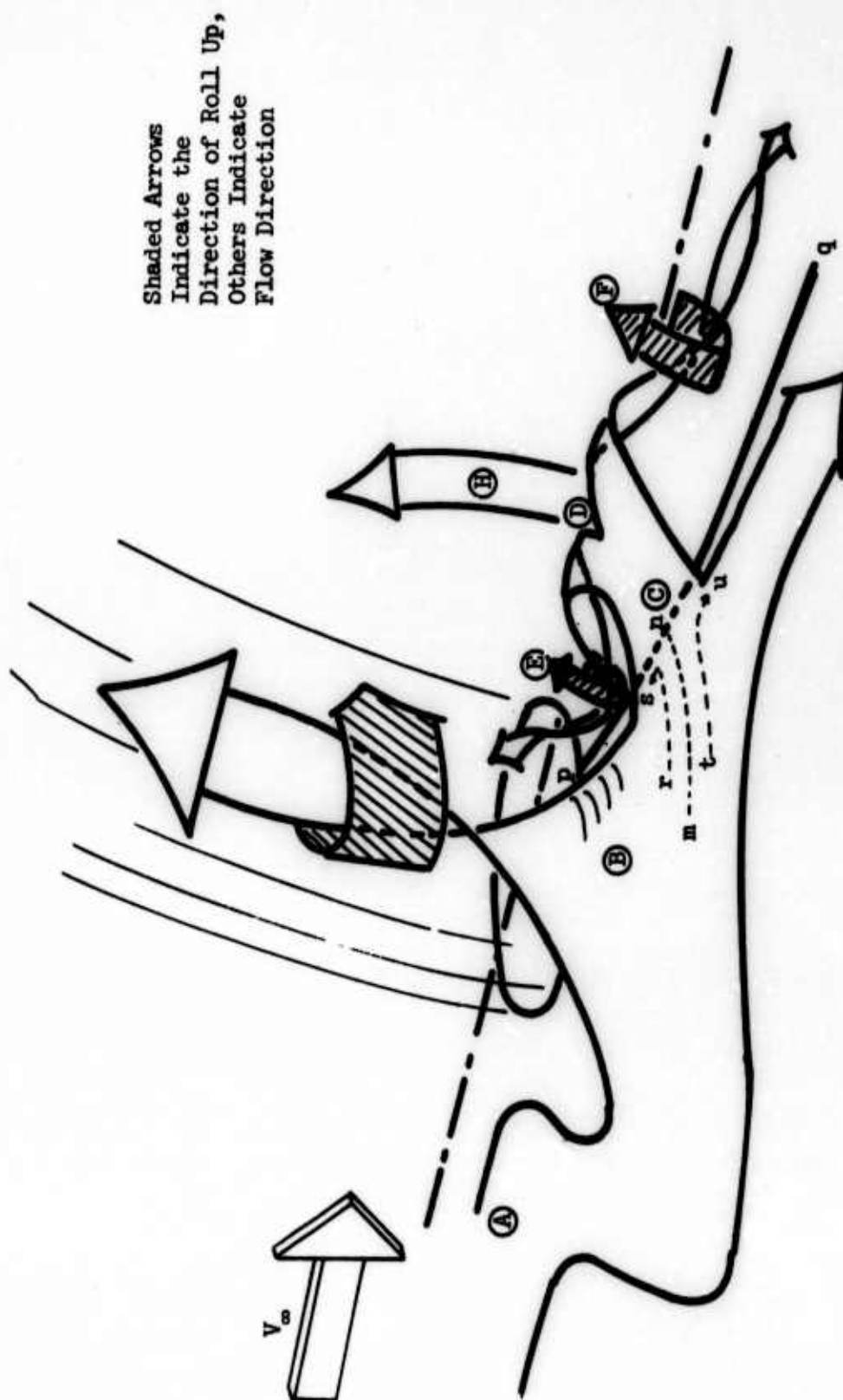
Figure 43. Extract from Extensive Flow Field Survey.



(b)  $y$  and  $z$  Components Only; View in the Plane of  $x/a=10$  Looking Upstream.

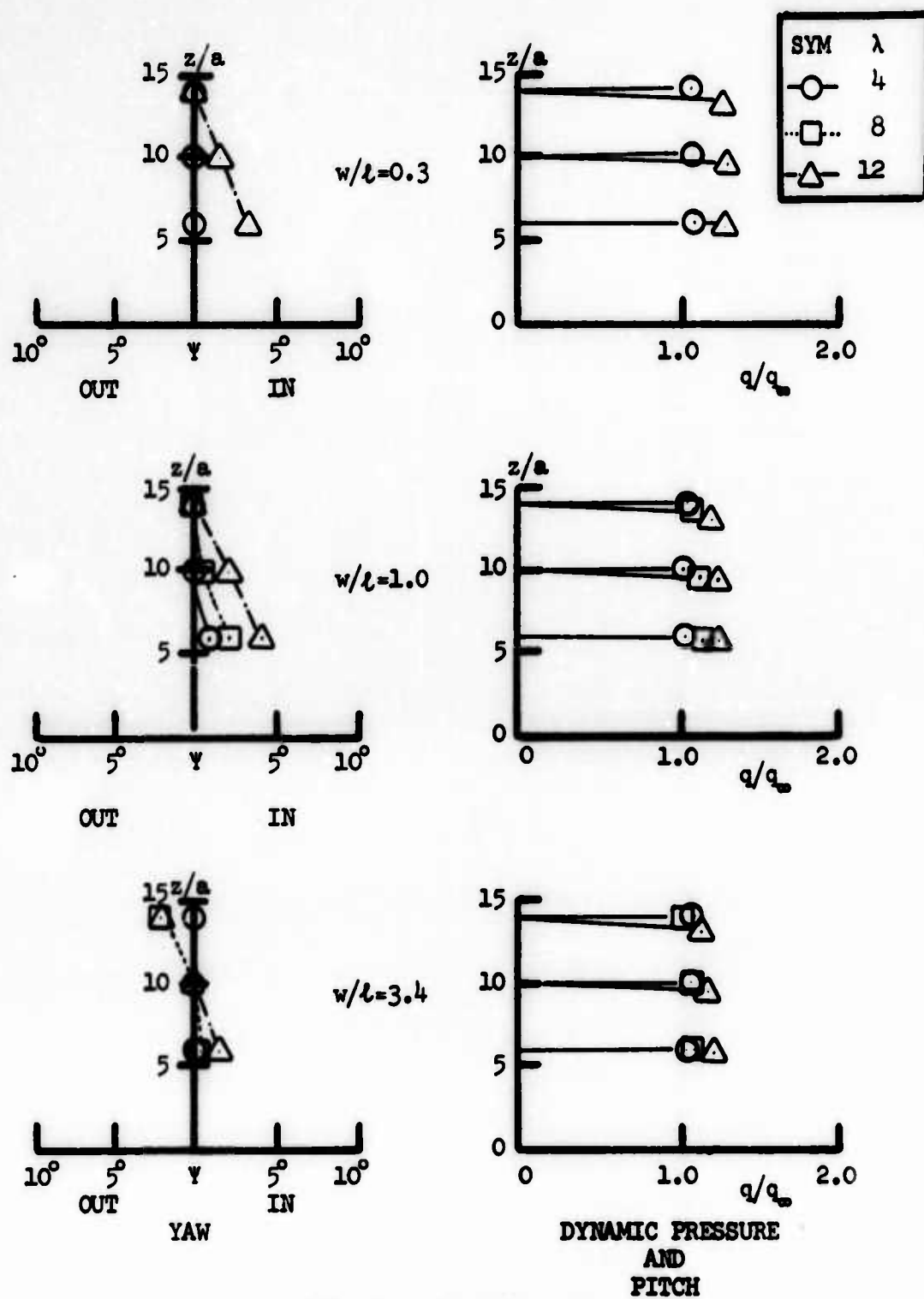
Figure 43. Extract from Extensive Flow Field Survey (Continued).





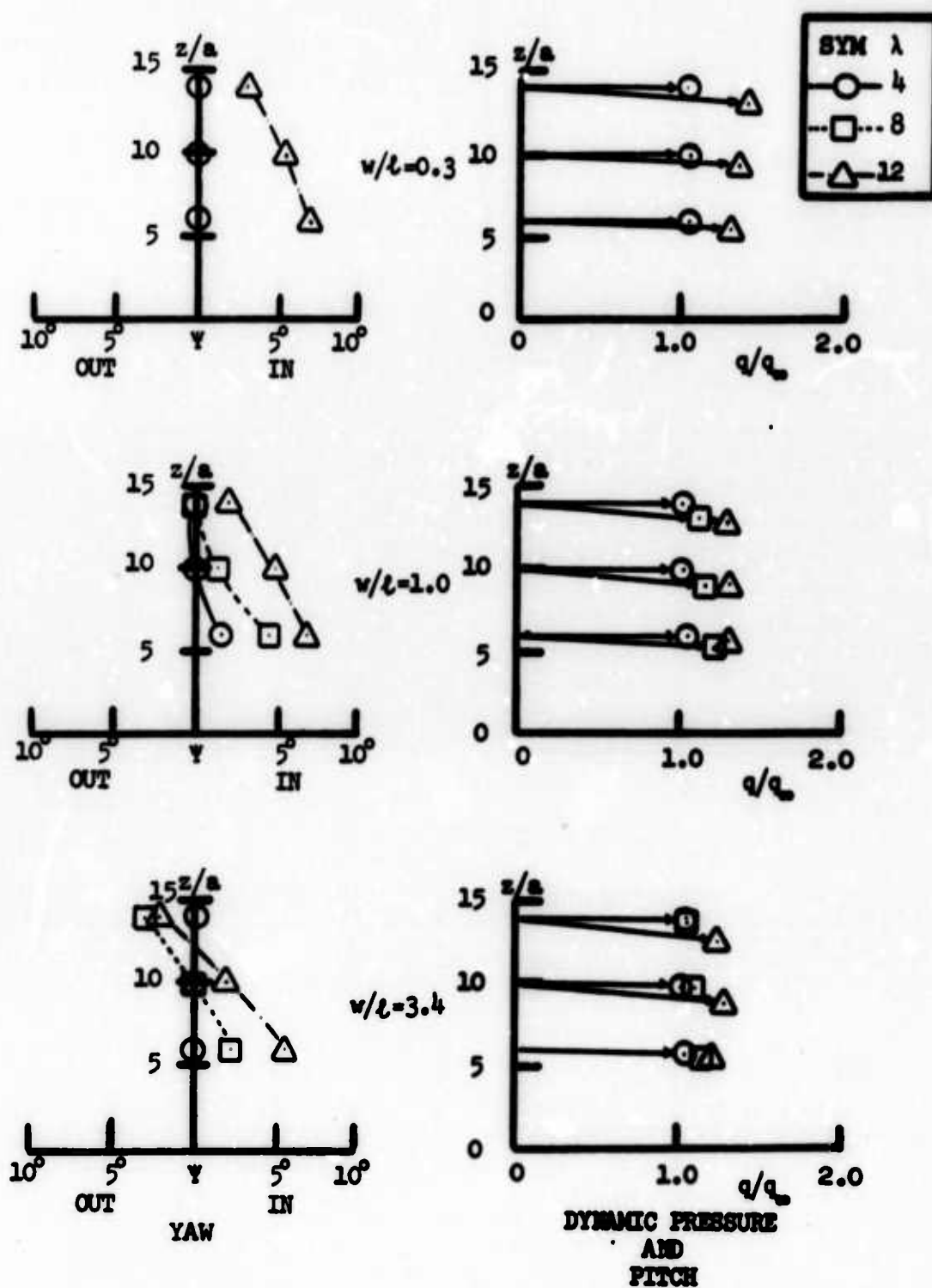
(c) Interpretation.

Figure 43. Extract from Extensive Flow Field Survey (Concluded).



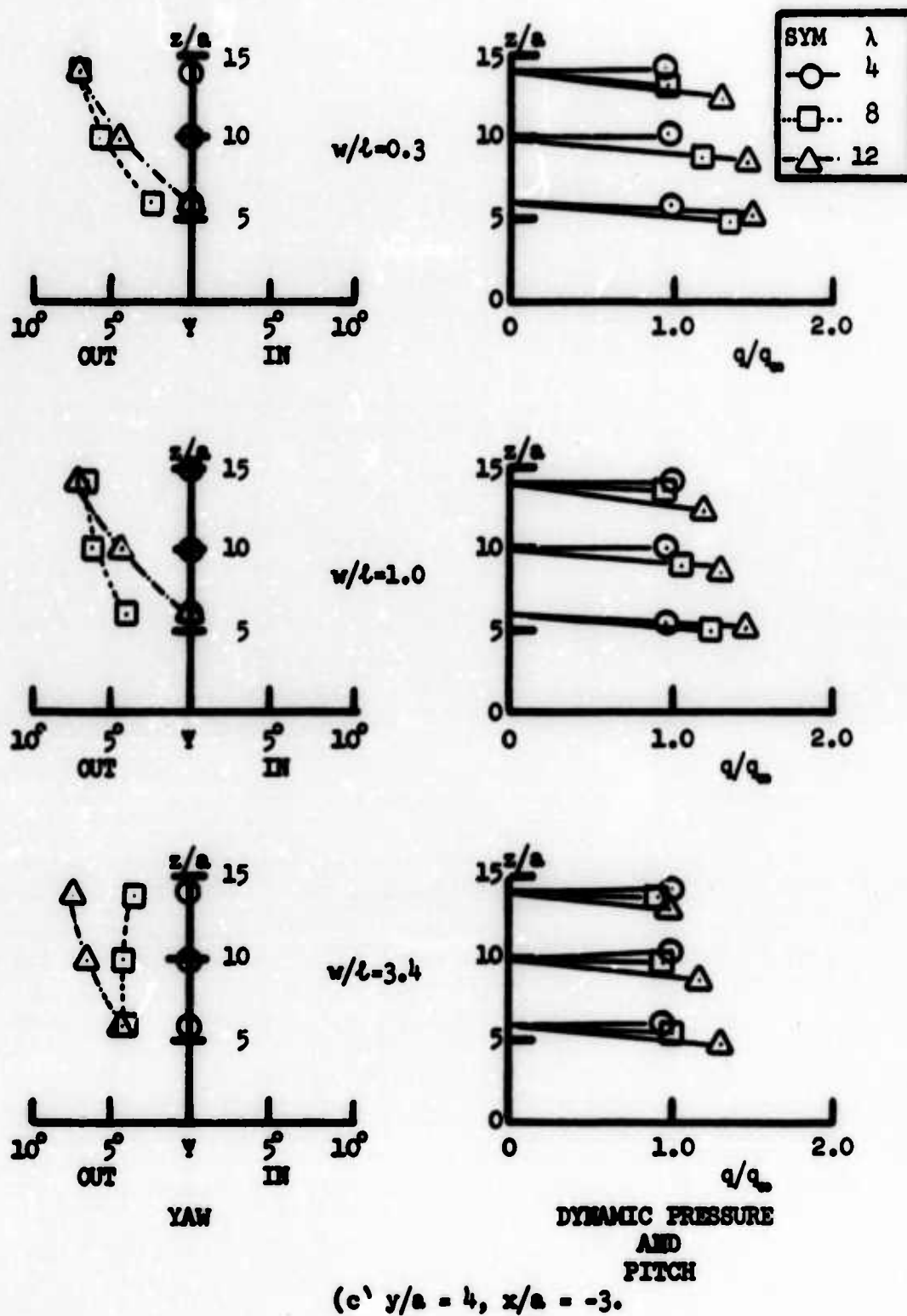
(a)  $z/a = 10$ ,  $x/a = -5$ .

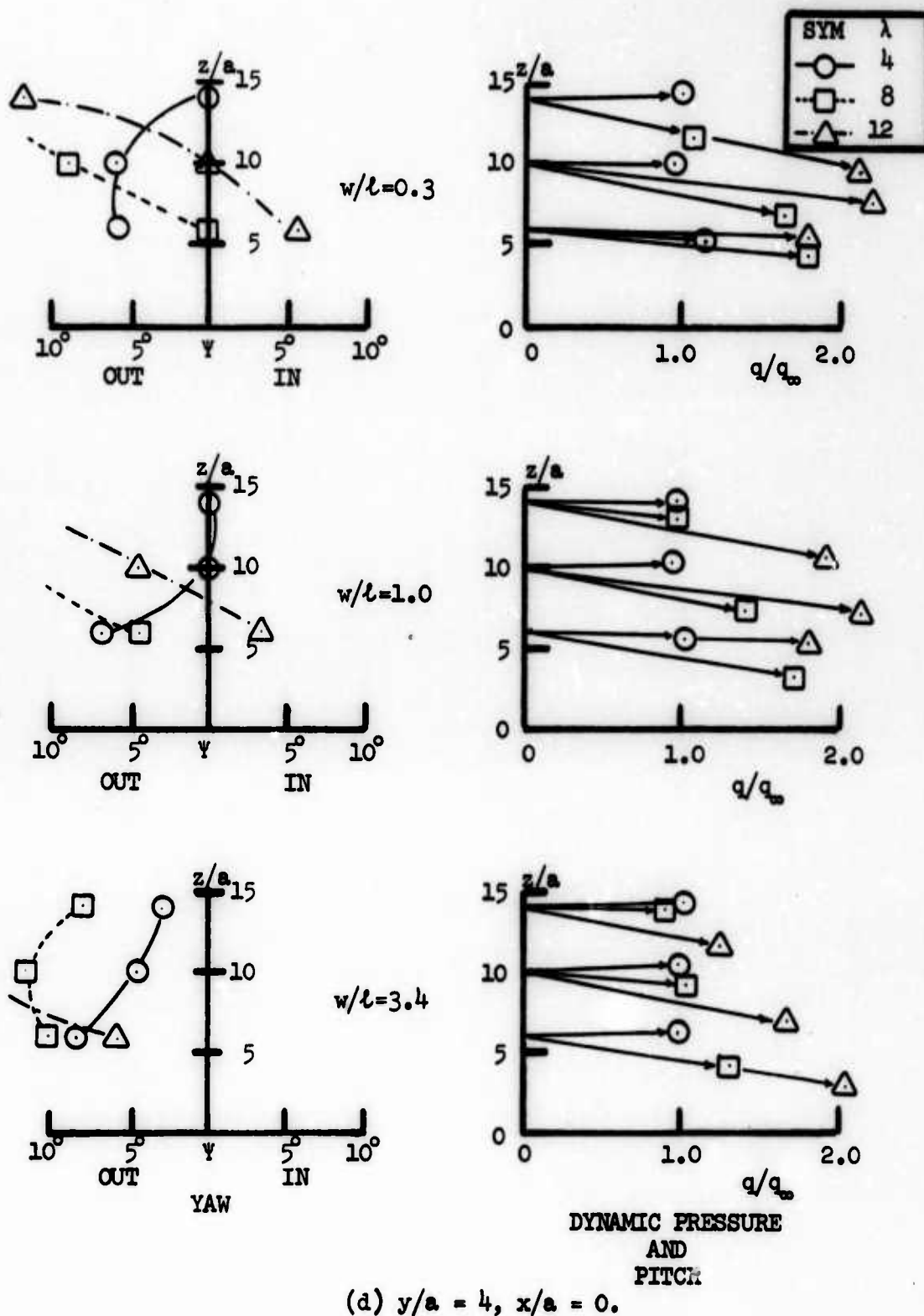
Figure 44. Lateral Flow Field Surveys,  $z/a \geq 6$ .

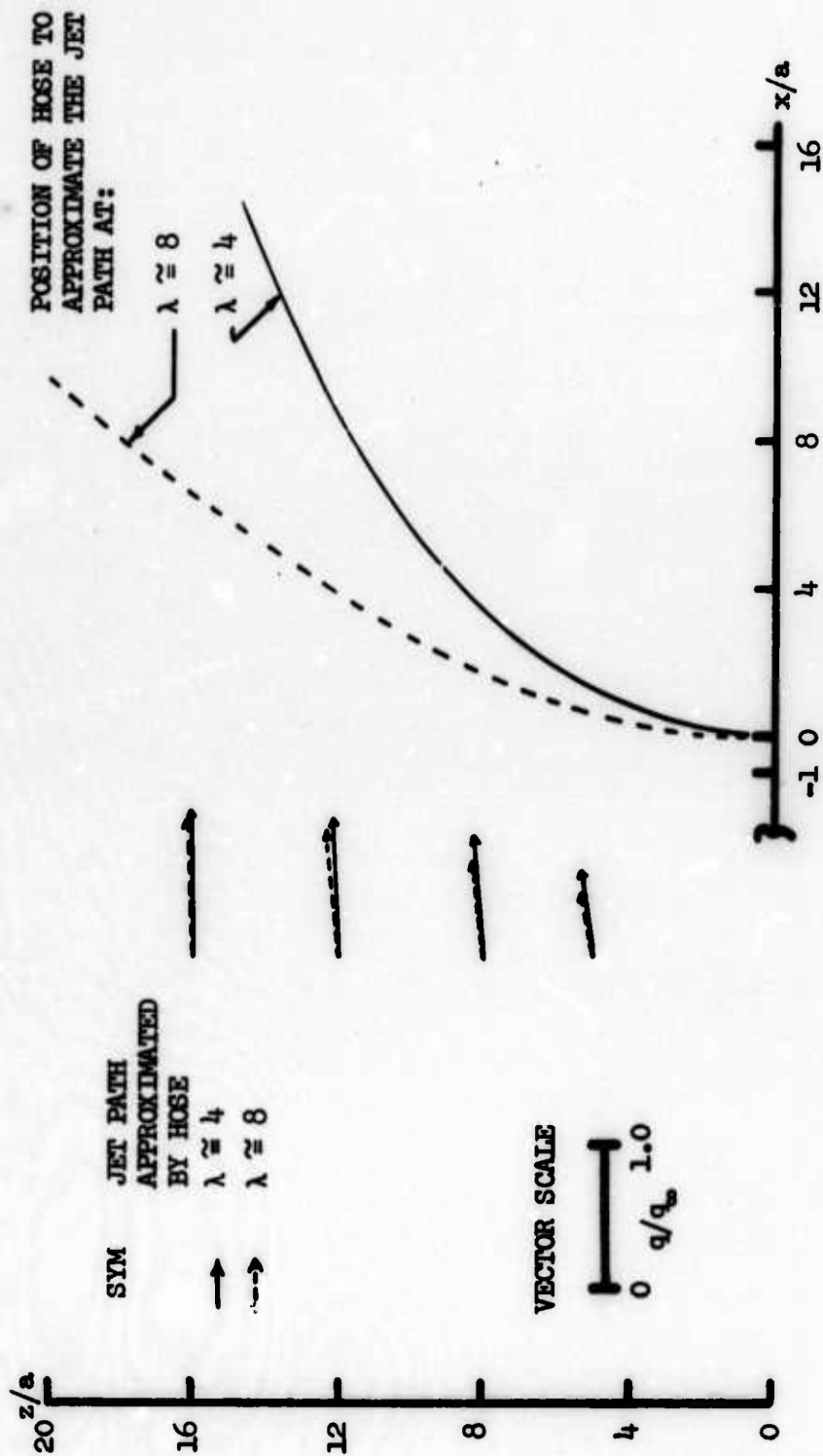


(b)  $y/a = 10, x/a = 0$ .

Figure 44. Lateral Flow Field Surveys,  $z/a \geq 6$  (Continued).

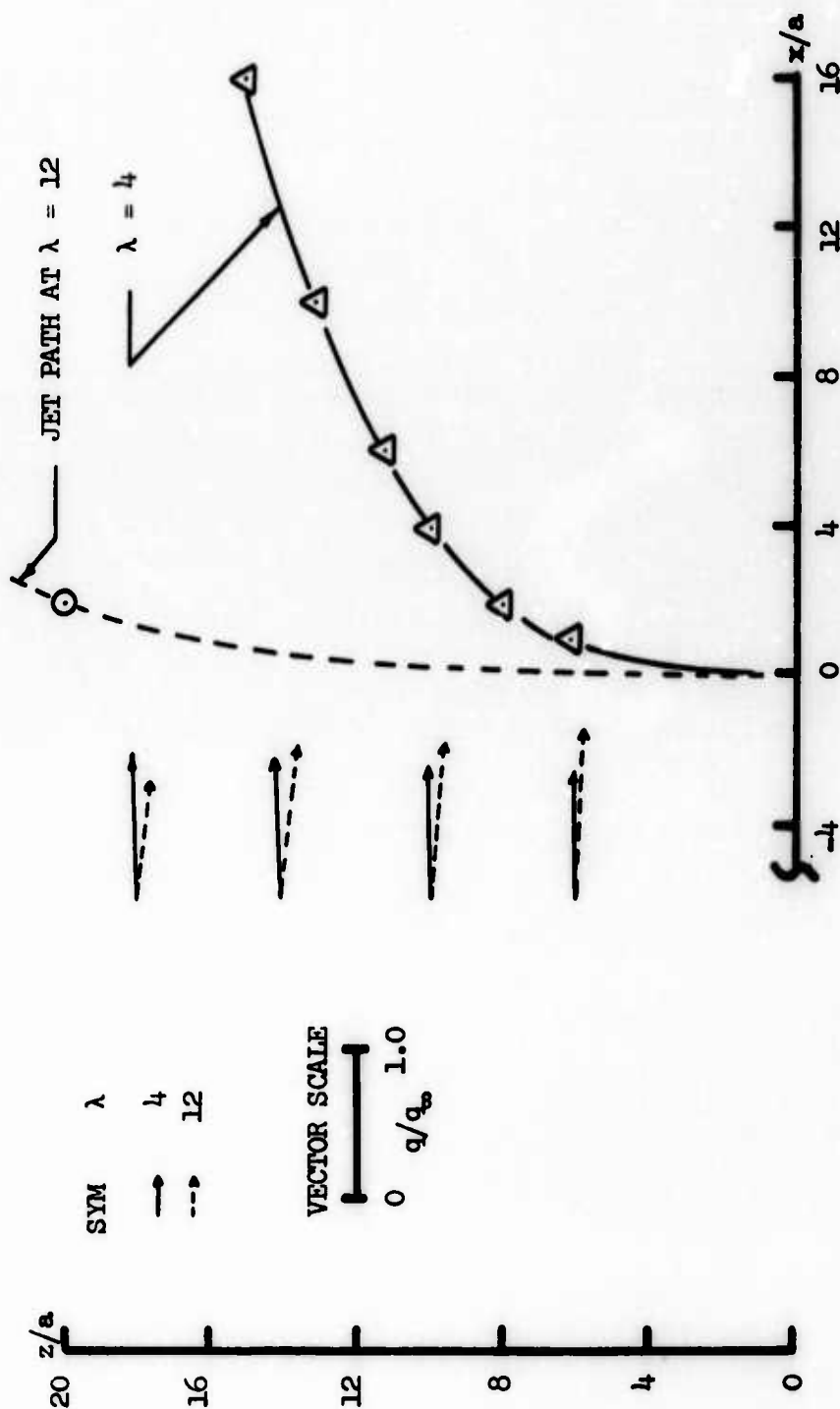
Figure 44. Lateral Flow Field Surveys,  $z/a \geq 6$  (Continued).

Figure 44. Lateral Flow Field Surveys,  $z/a \geq 6$  (Concluded).



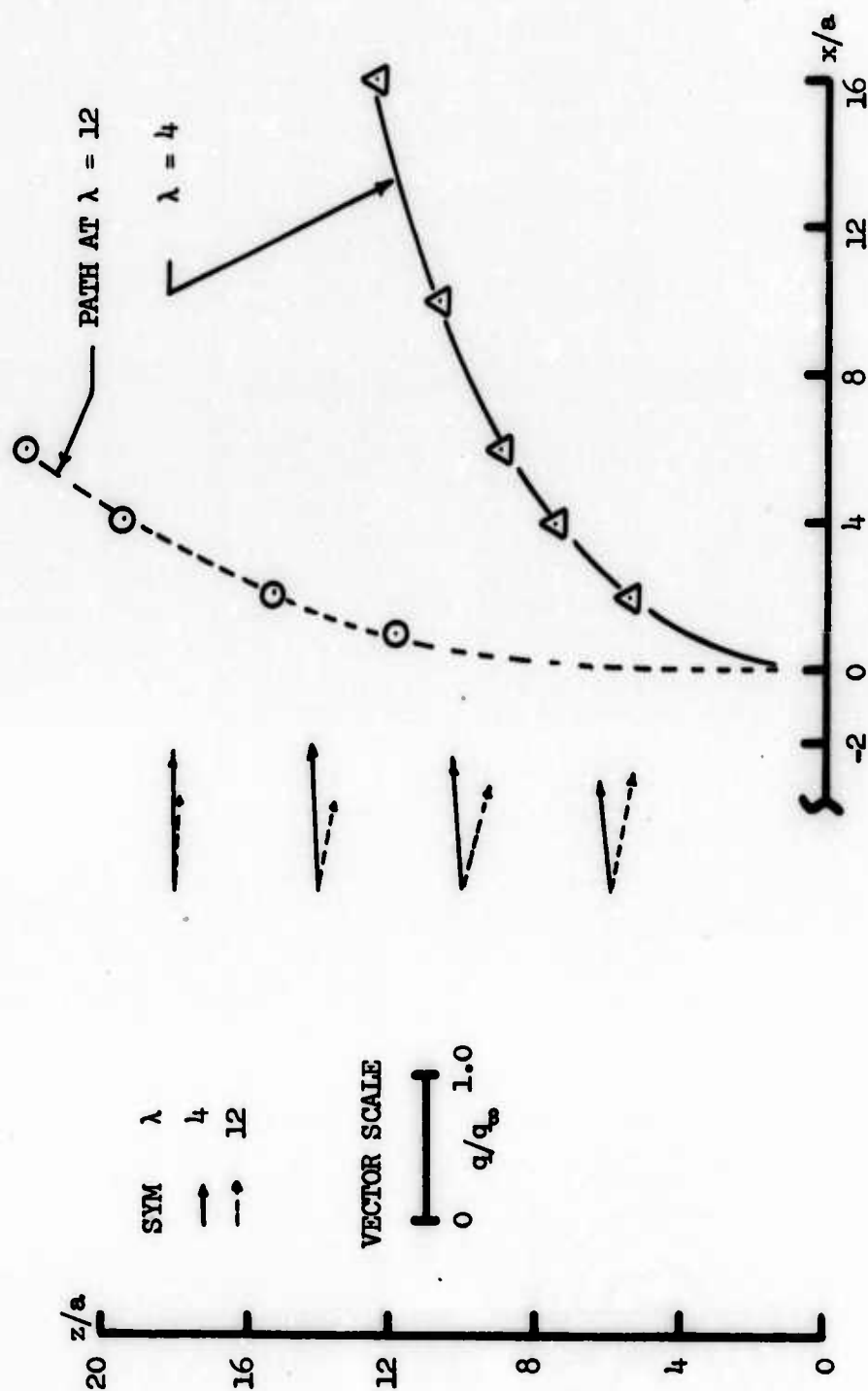
Vertical Traverse at  $x/a = -1$ ,  $y/a = 0$ .

Figure 45. Upstream Flow Field Surveys, Solid Blockage (Rubber Hose).



(a)  $w/l = 0.3$ , Vertical Traverse at  $x/a = -4$ ,  $y/a = 0$ .

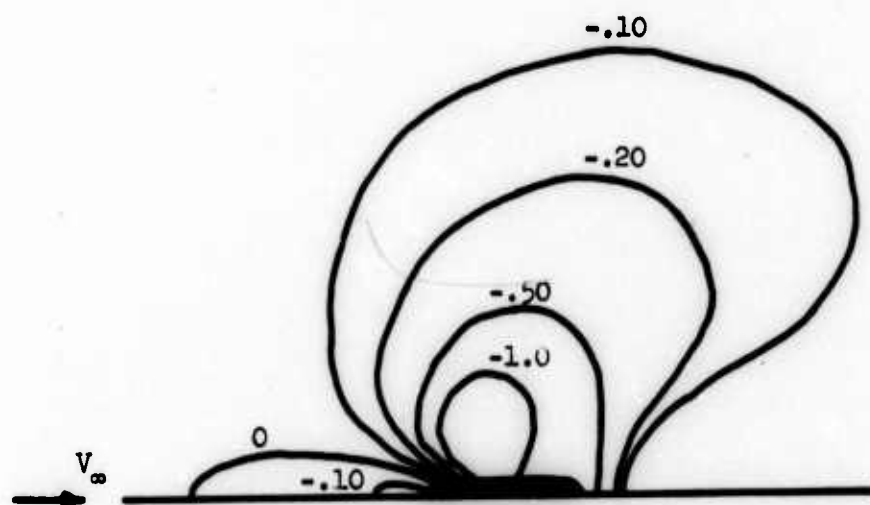
Figure 46. Upstream Flow Field Survey, Jet On.



(b)  $w/l = 3.4$ , Vertical Traverse at  $x/a = -2$ ,  $y/a = 0$ .

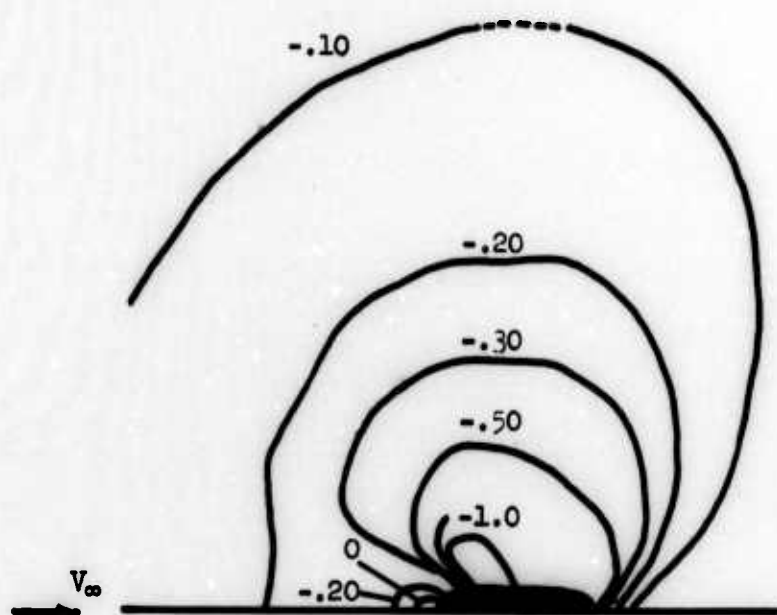
Figure 46. Upstream Flow Field Surveys, Jet On (Concluded).





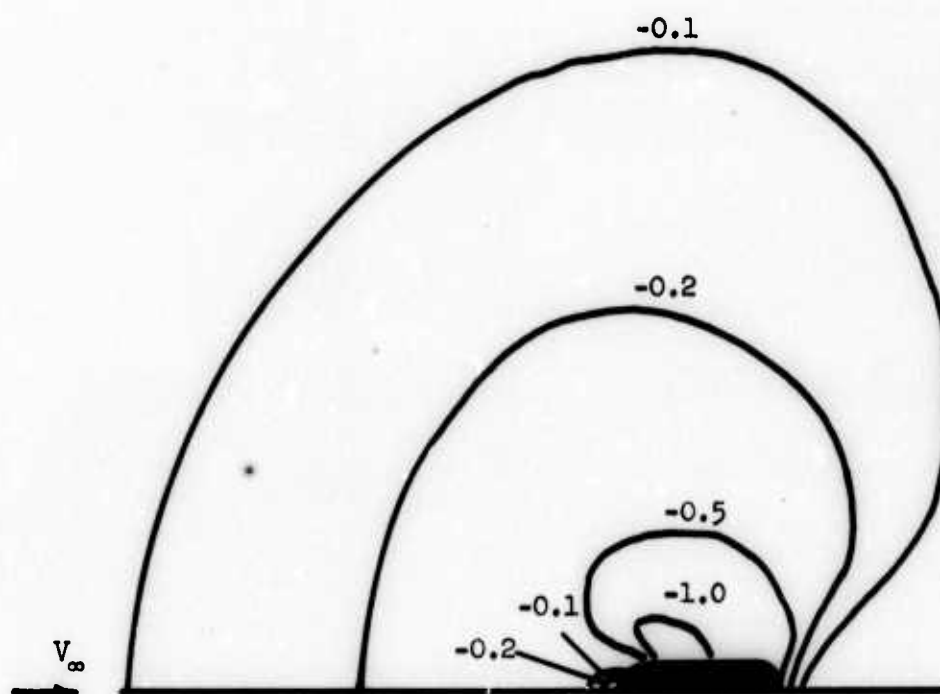
(a)  $w/l = 0.3$ ,  $\lambda = 4$ .

Figure 47. Surface  $C_p$  Contours.



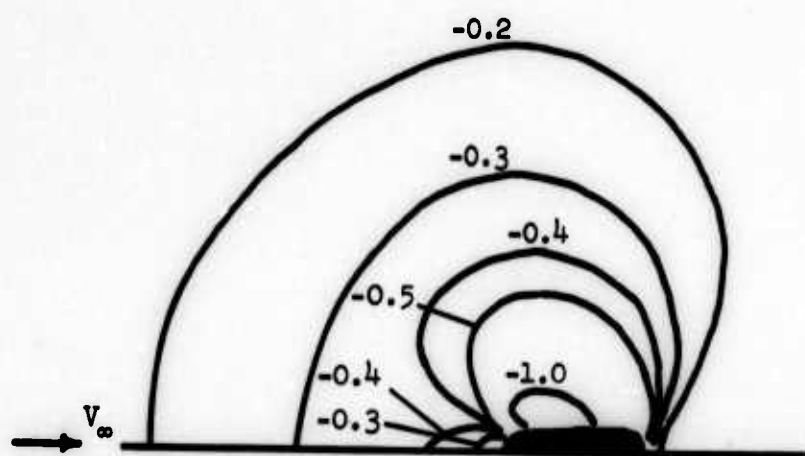
(b)  $w/l = 0.3$ ,  $\lambda = 8$ .

Figure 47. Surface  $C_p$  Contours (Continued).



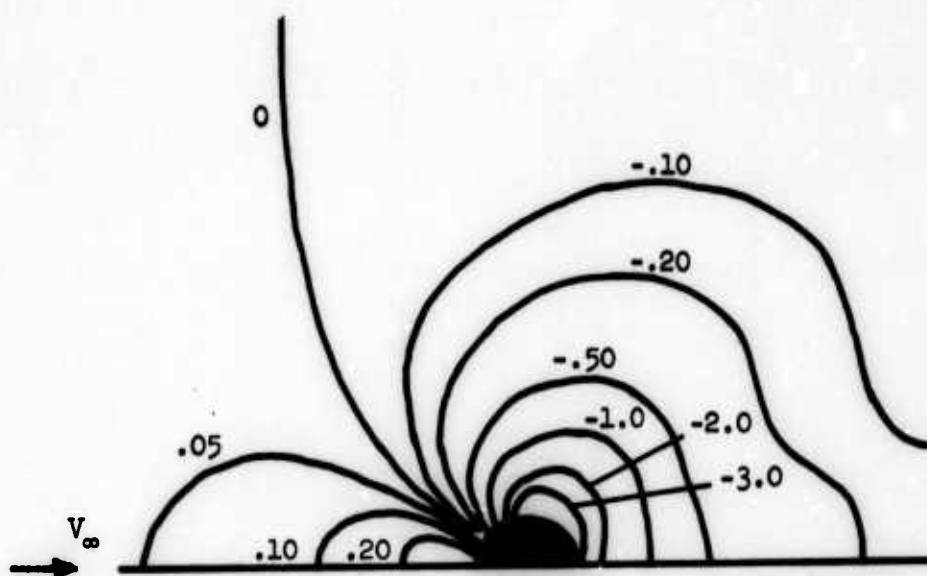
(c)  $w/l = 0.3$ ,  $\lambda = 10$ .

Figure 47. Surface  $C_p$  Contours (Continued).



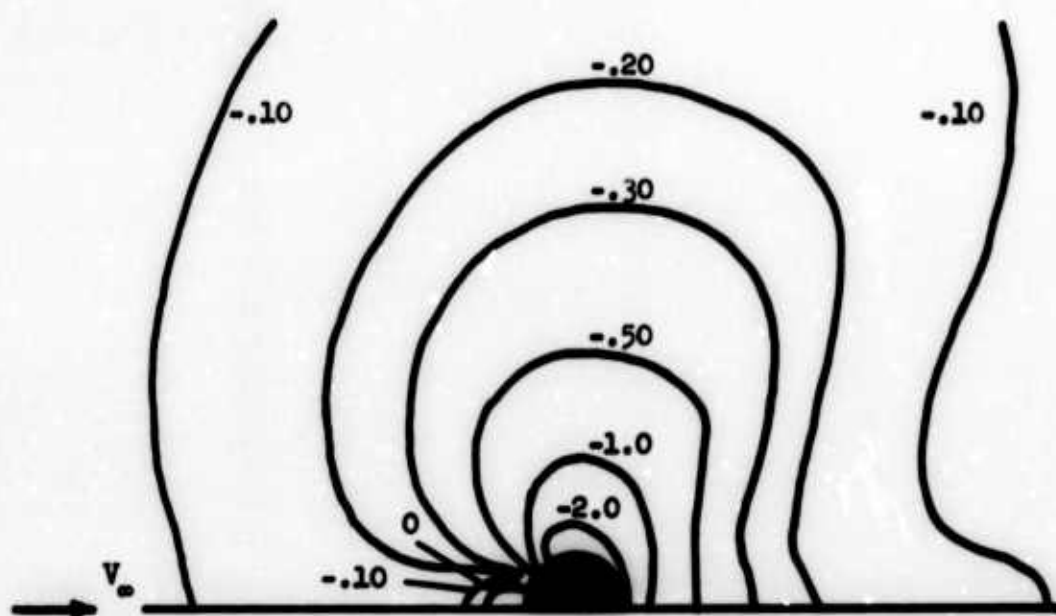
(d)  $w/l = 0.3$ ,  $\lambda = 12$ .

Figure 47. Surface  $C_p$  Contours (Continued).



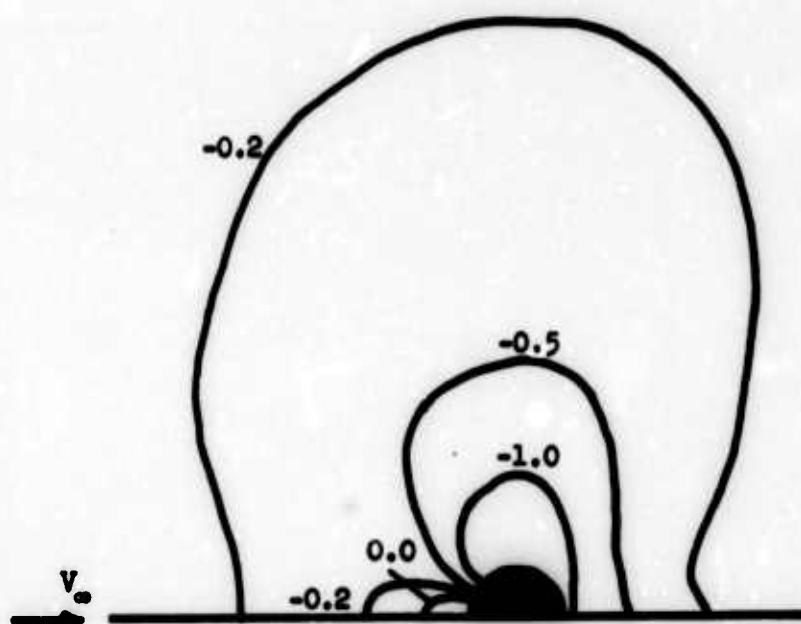
(e)  $w/l = 1.0$ ,  $\lambda = 4$ .

Figure 47. Surface  $C_p$  Contours (Continued).



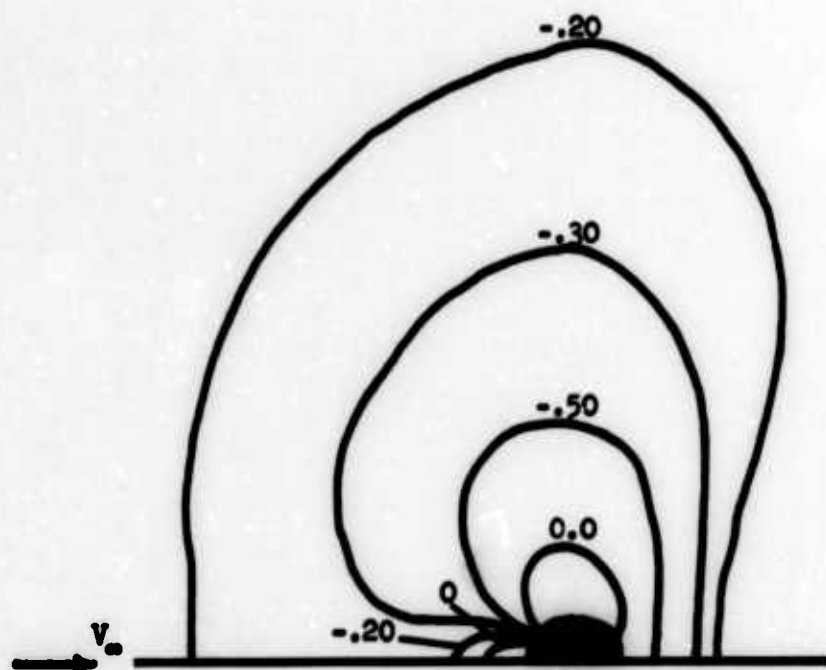
(f)  $w/l = 1.0$ ,  $\lambda = 8$ .

Figure 47. Surface  $C_p$  Contours (Continued).



(g)  $w/l = 1.0$ ,  $\lambda = 10$ .

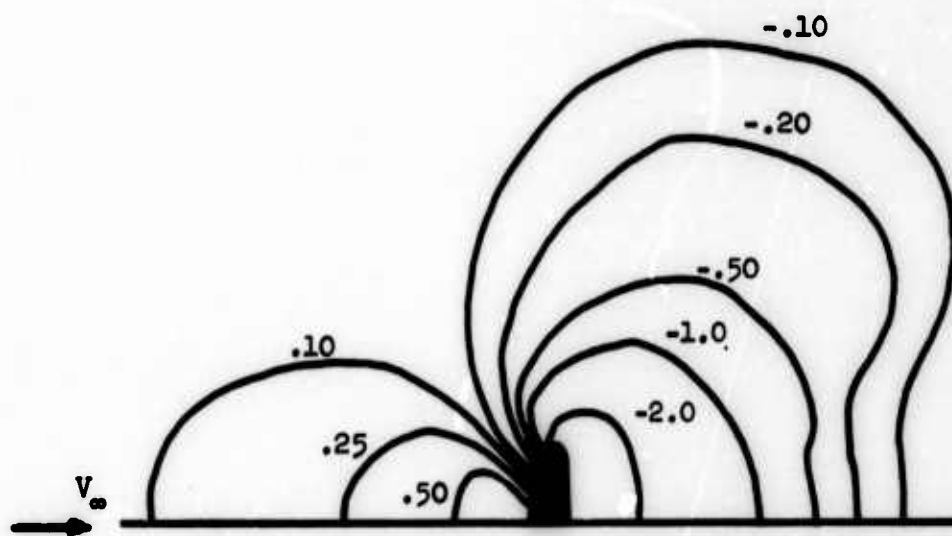
Figure 47. Surface  $C_p$  Contours (Continued).



(h)  $w/l = 1.0$ ,  $\lambda = 12$ .

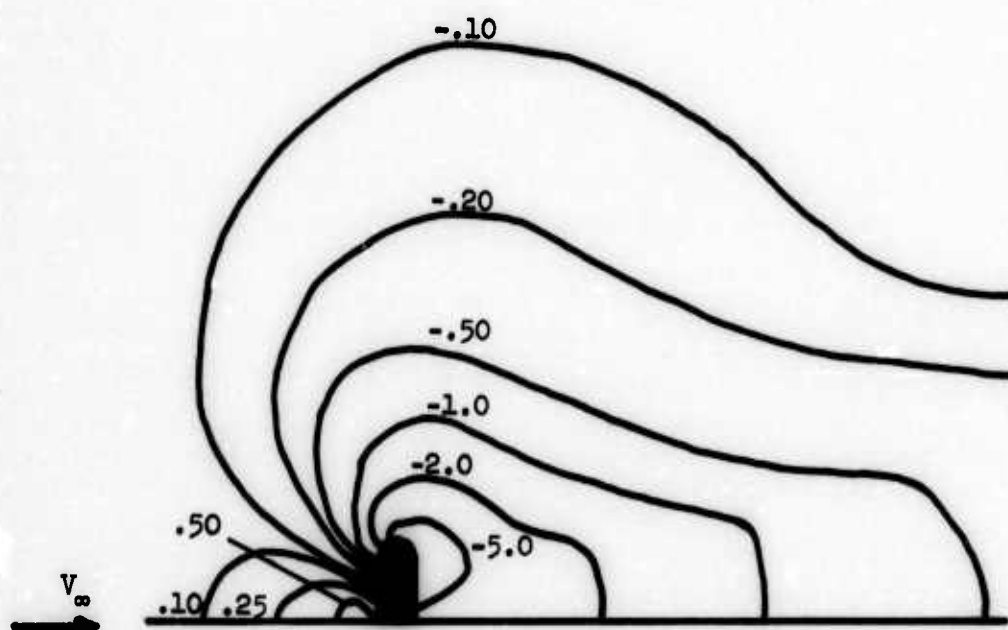
Figure 47. Surface  $C_p$  Contours (Continued).





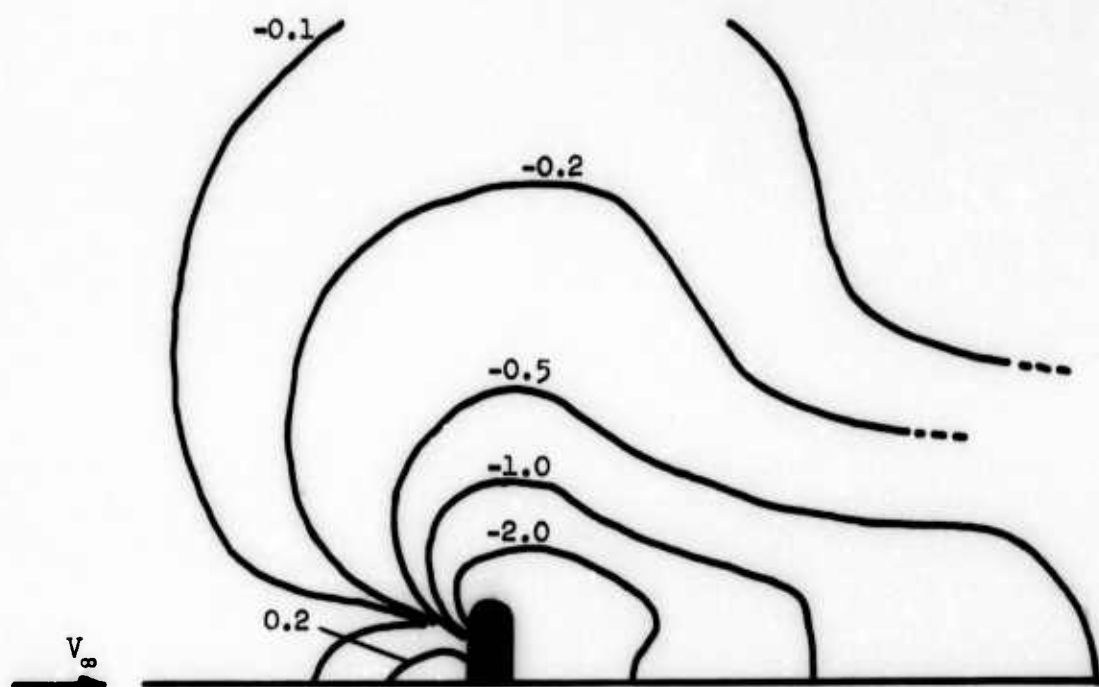
(1)  $w/l = 3.4$ ,  $\lambda = 4$ .

Figure 47. Surface  $C_p$  Contours (Continued).



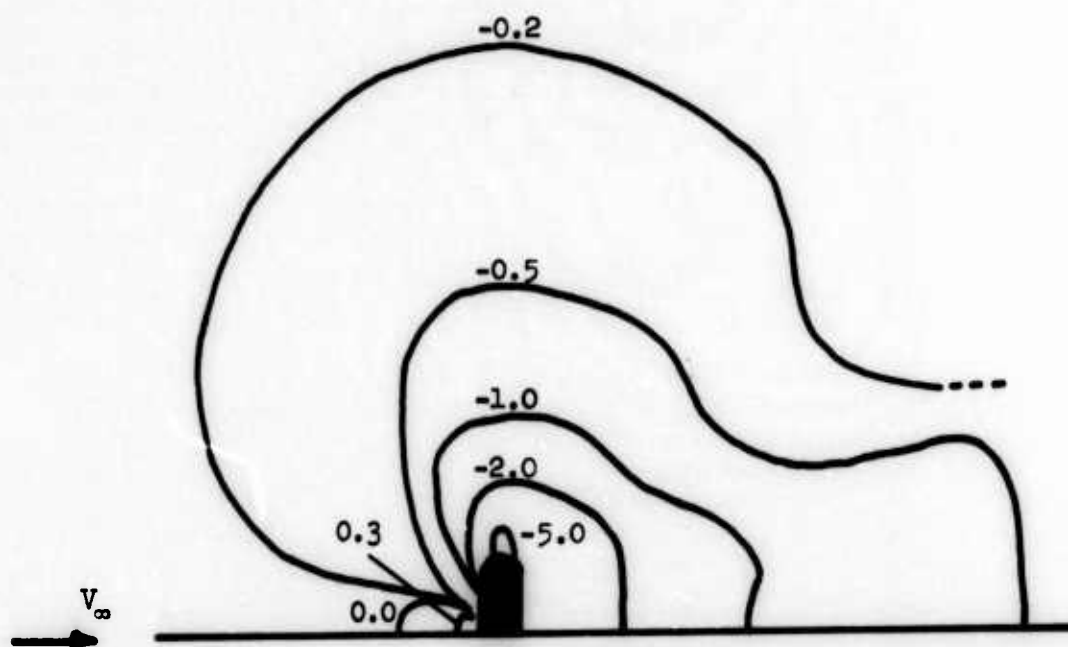
(j)  $w/l = 3.4$ ,  $\lambda = 8$ .

Figure 47. Surface  $C_p$  Contours (Continued).



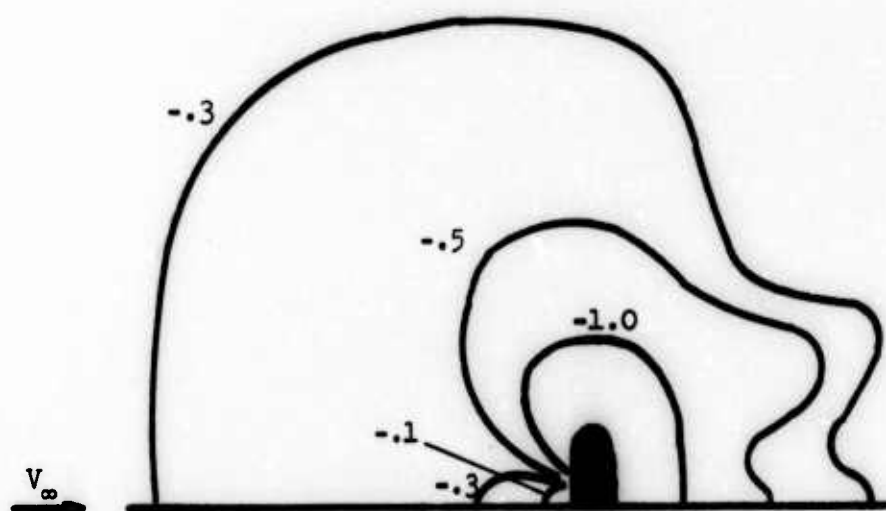
(k)  $w/l = 3.4$ ,  $\lambda = 10$ .

Figure 47. Surface  $C_p$  Contours (Continued).



(*l*)  $w/l = 3.4$ ,  $\lambda = 12$ .

Figure 47. Surface  $C_p$  Contours (Continued).



(m)  $w/l = 3.4$ ,  $\lambda = 20$ .

Figure 47. Surface  $C_p$  Contours (Concluded).

Unclassified

Security Classification

## DOCUMENT CONTROL DATA - R &amp; D

Security classification of title, body of abstract and indexing annotation must be entered when the overall report is classified)

1. ORIGINATING ACTIVITY (Corporate author)		2a. REPORT SECURITY CLASSIFICATION	
GEORGIA INSTITUTE OF TECHNOLOGY		Unclassified	
		2b. GROUP	
		NA	
3. REPORT TITLE			
AN EXPERIMENTAL INVESTIGATION OF A TURBULENT JET IN A CROSS FLOW			
4. DESCRIPTIVE NOTES (Type of report and inclusive dates)			
Technical Report, December 1970			
5. AUTHOR(S) (First name, middle initial, last name)			
DAVID K. MOSHER			
6. REPORT DATE		7a. TOTAL NO. OF PAGES	7b. NO. OF REFS
December 1970		182	47
8a. CONTRACT OR GRANT NO.		9a. ORIGINATOR'S REPORT NUMBER(S)	
DAHCO4 68 C 0004		GITAER 70-7	
b. PROJECT NO.			
c.		9b. OTHER REPORT NO(S) (Any other numbers that may be assigned this report)	
d.			
10. DISTRIBUTION STATEMENT			
This document has been approved for public release and sale; its distribution is unlimited.			
11. SUPPLEMENTARY NOTES		12. SPONSORING MILITARY ACTIVITY	
		U. S. Army Research Office-Durham Box CM, Duke Station Durham, North Carolina 27706	
13. ABSTRACT			
<p>→The interference phenomenon occurring when a subsonic turbulent jet exhausts normally from a large flat plate into a low speed crossflow has been experimentally investigated in the Georgia Tech nine foot wind tunnel. Static pressures have been measured on the surface around the jet. In the region off the surface, including the jet plume, wake and surrounding areas, the average total and static pressures and the average velocity magnitudes and directions have been determined. Three jet exit configurations were studied, one circular and two slot-shaped with width to length ratios of 0.3 and 3.4. All have the same exit area. The effective jet to cross-flow velocity ratio was varied, for each of the exit configurations, over the range <math>4.0 \leq \lambda \leq 12.0</math>. Analysis of the data indicates that the pressure distributions induced on the surface are a combined result of the jet's blocking and entraining effects on the cross flow with entrainment becoming the more dominant of the two as the effective velocity ratio is increased. This relative dominance brings about an attenuation of total interference lift loss (when computed as a fraction of gross thrust, <math>\Delta L/T</math>) primarily by causing a rise in the low pressures in the wake region as <math>\lambda</math> increases. When the effective velocity ratio is held fixed, the total interference lift loss increases with increasing width to length ratio of the jet exit.</p>			
-----			
14. Key Words			
Jet, Crossflow, VTOL, STOL			